

ADA130190

AFWAL TR-82-3103

(2)



ADVANCED FATIGUE DAMAGE DEVELOPMENT IN GRAPHITE EPOXY LAMINATES

RUSSEL D. JAMISON
KENNETH L. REIFSNIDER

Virginia Polytechnic Institute and State University
Blacksburg, VA 24061

December 1982

INTERIM REPORT FOR PERIOD
1 April 1981 to 1 December 1982

DTIC

JUL 7 1983

B

Approved for public release; distribution unlimited.

DTIC FILE COPY

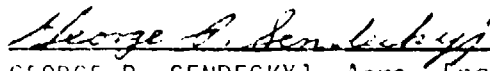
FLIGHT DYNAMICS LABORATORY
AIR FORCE WRIGHT AERONAUTICAL LABORATORIES
AIR FORCE SYSTEMS COMMAND
WRIGHT-PATTERSON AIR FORCE BASE, OHIO 45433

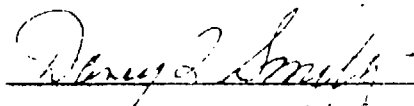
83 07 6 203

NOTICE


When Government drawings, specifications, or other data are used for any purpose other than in connection with a definitely related Government procurement operation, the United States Government thereby incurs no responsibility nor any obligation whatsoever, and the fact that the government may have formulated, furnished, or in any way supplied the said drawings, specifications, or other data, is not to be regarded by implication or otherwise as in any manner licensing the holder or any other person or corporation, or conveying any rights or permission to manufacture, use, or sell any patented invention that may in any way be related thereto.

This technical report has been reviewed and is approved for publication.


GEORGE P. SENDECKYJ, Aero. Engr.
Fatigue, Fracture & Reliability Gp.


DAVEY L. SMITH, Chief
Structural Integrity Branch
Structures & Dynamics Division

FOR THE COMMANDER:


RALPH L. KUSTER, JR., Col, USAF
Chief, Structures & Dynamics Division

"If your address has changed, if you wish to be removed from our mailing list, or if the addressee is no longer employed by your organization please notify AFWAL/FIBE, W-P AFB, OH 45433 to help us maintain a current mailing list".

Copies of this report should not be returned unless return is required by security considerations, contractual obligations, or notice on a specific document.

Unclassified

SECURITY CLASSIFICATION OF THIS PAGE (When Data Entered)

REPORT DOCUMENTATION PAGE		READ INSTRUCTIONS BEFORE COMPLETING FORM															
1. REPORT NUMBER AFWL-TR-82-3103	2. GOVT ACCESSION NO.	3. RECIPIENT'S CATALOG NUMBER															
4. TITLE (and Subtitle) Advanced Fatigue Damage Development in Graphite Epoxy Laminates		5. TYPE OF REPORT & PERIOD COVERED Interim Report April 81 - December 82															
7. AUTHOR(s) Russell D. Jamison Kenneth L. Reifsnider		6. PERFORMING ORG. REPORT NUMBER															
9. PERFORMING ORGANIZATION NAME AND ADDRESS Virginia Polytechnic Institute and State University, Blacksburg, VA 24061		8. CONTRACT OR GRANT NUMBER(s) F33615-81-K-3225															
11. CONTROLLING OFFICE NAME AND ADDRESS Flight Dynamics Laboratory (FIBE) Air Force Wright Aeronautics Laboratories (AFSC) Wright-Patterson AFB, OH 45433		10. PROGRAM ELEMENT, PROJECT, TASK AREA & WORK UNIT NUMBERS PE 61101F PROJECT 2307 WORK UNIT 2307N117															
14. MONITORING AGENCY NAME & ADDRESS (if different from Controlling Office)		12. REPORT DATE December 1982															
		13. NUMBER OF PAGES 234															
		15. SECURITY CLASS. (of this report) Unclassified															
		15a. DECLASSIFICATION/DOWNGRADING SCHEDULE															
16. DISTRIBUTION STATEMENT (of this Report) Approved for public release: distribution unlimited.																	
17. DISTRIBUTION STATEMENT (of the abstract entered in Block 20, if different from Report)																	
18. SUPPLEMENTARY NOTES																	
19. KEY WORDS (Continue on reverse side if necessary and identify by block number) <table border="0"> <tr> <td>Composite Materials</td> <td>Stiffness Changes</td> <td>Nondestructive</td> </tr> <tr> <td>Graphite/Epoxy Laminates</td> <td>Delamination</td> <td>Evaluation (NDE)</td> </tr> <tr> <td>Fatigue Testing</td> <td>Microcracking</td> <td></td> </tr> <tr> <td>Damage Development</td> <td>Matrix Cracks</td> <td></td> </tr> <tr> <td>Damage States</td> <td>Fiber Fracture</td> <td></td> </tr> </table>			Composite Materials	Stiffness Changes	Nondestructive	Graphite/Epoxy Laminates	Delamination	Evaluation (NDE)	Fatigue Testing	Microcracking		Damage Development	Matrix Cracks		Damage States	Fiber Fracture	
Composite Materials	Stiffness Changes	Nondestructive															
Graphite/Epoxy Laminates	Delamination	Evaluation (NDE)															
Fatigue Testing	Microcracking																
Damage Development	Matrix Cracks																
Damage States	Fiber Fracture																
20. ABSTRACT (Continue on reverse side if necessary and identify by block number) <p>Results of an experimental investigation of damage development in T300/5208 graphite epoxy laminates subjected to tension-tension cyclic loading are reported. The concept of laminate stiffness reduction as a damage analogue is shown to be a valuable means of test control and damage interpretation. The relationship between stiffness and number of cycles is shown to be unique for each laminate type studied, each possessing three distinct stages, but markedly different among the laminate types. By using</p>																	

Unclassified

SECURITY CLASSIFICATION OF THIS PAGE (When Data Entered)

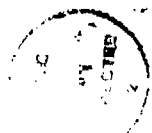
two complementary nondestructive evaluation (NDE) techniques, edge replication and penetrant-enhanced stereo X-ray radiography along with a method for depling fatigue-damaged specimens, the stages of stiffness reduction were found to correspond variously to the predominance of matrix cracking or delamination or interactions of these matrix damage modes. A number of subordinate matrix damage modes including interior delamination, microcracking, and longitudinal splitting are identified with the matrix cracks which produce them.

Results of a parallel study of fatigue-related fiber fracture are also reported. The dominant role of matrix cracks in the fracture of fibers in adjacent plies is established for the first time. Fiber breaks in all plies are shown to be segregated into narrow bands whose location and direction correspond to matrix cracks in adjacent plies. Details regarding discrete modes of individual fiber fracture and through-thickness condition of fibers are included. An analysis of the occurrence of multiple adjacent fiber breaks is presented along with a discussion of the strong dependence of fiber fracture density on the laminate type. The wide variation in fiber fracture density among the laminate types and the near-absence of fiber fractures in certain laminates at the end of fatigue life is explained in terms of a margin of strength concept.

PREFACE

The work reported herein was performed under Contract F33615-81-K-3225, Project 2307, Work Unit 2307N117, sponsored by the Flight Dynamics Laboratory of the Air Force Wright Aeronautical Laboratories, Wright-Patterson Air Force Base, Ohio 45433. Dr. G. P. Sendeckyj, AFWAL/FIBE, was the Air Force Program Monitor.

The authors wish to express their appreciation to G. K. McCauley for his assistance with the photo and art work, and to Mrs. Barbary Wengert for typing the manuscript.



Accepted for 1981	✓
Dis. 1	
A	

TABLE OF CONTENTS

	<u>Page</u>
SECTION	
I. INTRODUCTION.....	1
II. LITERATURE REVIEW.....	6
III. EXPERIMENTAL PROCEDURE.....	22
IV. RESULTS AND DISCUSSION.....	61
V. CONCLUSIONS AND SUMMARY.....	181
REFERENCES.....	192
APPENDIX. MOIRÉ INTERFEROMETRY.....	201

PREVIOUS PAGE
IS BLANK



LIST OF ILLUSTRATIONS

<u>FIGURE</u>	<u>PAGE</u>
1. Interlaminar Shear and Normal Stresses.....	26
2. Specimen Types.....	30
3. Specimen in the Testing Machine with Extensometer Mounted.....	32
4. Initial Static Stiffness Measurement Procedure.....	36
5. Data Acquisition and Control System.....	37
6. Loading Fixture for the Application of X-ray Enhancing Agent.....	45
7. Tilt Method of Stereo X-ray Radiography.....	48
8. Stereo X-ray Radiography Tilting Fixture.....	50
9. Stereoscopic Microscope.....	51
10. Typical Stereo X-ray Image Pair.....	53
11. Optical Micrographs of a Deplied Lamina.....	57
12. Longitudinal Crack Sectioning Schematic.....	60
13. Comparison of Failure Modes in a $[0,90_2]_S$ Laminate.....	62
14. Typical Stiffness Reduction Curve for a $[0,90_2]_S$ Laminate.....	65
15. Edge Replicas from a Progressively Fatigue-Damaged $[0,90_2]_S$ Laminate (Left Side).....	66
16. Edge Replicas from a Progressively Fatigue-Damaged $[0,90_2]_S$ Laminate (Right Side).....	68
17. X-ray Radiographs of a Progressively Fatigue-Damaged $[0,90_2]_S$ Laminate.....	69
18. Edge Replica from a $[0,90_2]_S$ Laminate at Stage I.....	72

19.	Stiffness Reduction and Crack Development for a [0,90 ₂] _s Laminate at Stage I.....	73
20.	Edge Replica from a [0,90 ₂] _s Laminate at Stage II.....	76
21.	X-ray Radiographs of Sections Removed from a [0,90 ₂] _s Laminate.....	78
21.	(cont'd) Sectioning Schematic.....	79
22.	X-ray Radiograph of a [0,90 ₂] _s Laminate at Stage II.....	81
23.	Longitudinal Crack Surface.....	83
24.	Transverse Crack Surface.....	84
25.	Detail of X-ray Radiograph of a [0,90 ₂] _s Laminate at Stage II.....	86
26.	Transverse Section of a Longitudinal Crack (Near Tip)...	87
27.	Transverse Section of a Longitudinal Crack (Away from the Tip).....	89
28.	Crack Tip Stresses.....	90
29.	Zero Degree Stresses in the Neighborhood of a Transverse Crack.....	92
30.	Influence of a Longitudinal Crack on Interior Delamination Formation.....	93
31.	X-ray Radiograph of a [0,90 ₂] _s Laminate at Stage III.....	95
32.	Longitudinal Split Model.....	98
33.	Typical Stiffness Reduction Curve for a [0,±45] _s Laminate.....	101
34.	X-ray Radiographs of a Progressively Fatigue- Damaged [0,±45] _s Laminate.....	102
35.	Edge Replica from a [0,±45] _s Laminate at Stage I.....	105
36.	X-ray Radiograph of a [0,±45] _s Laminate at Stage I.....	107
37.	Edge Replica from a [0,±45] _s Laminate at Stage II.....	108

38.	X-ray Radiograph of a $[0,\pm45]_S$ Laminate at Stage II....	109
39.	Crack Development in the +45 Degree Plies of a $[0,\pm45]_S$ Laminate.....	111
40.	Edge Replica from a $[0,\pm45]_S$ Laminate at Stage III.....	112
41.	X-ray Radiograph of a $[0,\pm45]_S$ Laminate at Stage III.....	113
42.	Model for Microcrack Formation in $[0,\pm45]_S$ Laminates...	115
43.	Typical Stiffness Reduction Curve for a $[0,90,\pm45]_S$ Laminate.....	117
44.	X-ray Radiographs of a Progressively Fatigue-Damaged $[0,90,\pm45]_S$ Laminate.....	118
45.	Edge Replicas from a Progressively Fatigue-Damaged $[0,90,\pm45]_S$ Laminate.....	122
46.	Edge Replicas from a Progressively Fatigue-Damaged $[0,90,\pm45]_S$ Laminate.....	125
47.	X-ray Radiographs of a $[0,90,\pm45]_S$ Laminate at Stage I.....	126
48.	Stiffness Reduction and Crack Development in a $[0,90,\pm45]_S$ Laminate.....	127
49.	Edge Replica from a $[0,90,\pm45]_S$ Laminate at Stage II.....	128
50.	X-ray Radiograph of a $[0,90,\pm45]_S$ Laminate at Stage II.....	130
51.	Sublaminates Resulting from Delamination in a $[0,90,\pm45]_S$ Laminate.....	133
52.	Delamination Boundaries in a $[0,90,\pm45]_S$ Laminate.....	134
53.	Stiffness and Delamination Relationship for $[0,90,\pm45]_S$ Laminates.....	139
54.	Edge Replica from a $[0,90,\pm45]_S$ Laminate at Stage III.....	141
55.	X-ray Radiograph of a $[0,90,\pm45]_S$ Laminate at Stage III.....	142

56.	Detail of Figure 55.....	143
57	Microcracks in $[0,90,\pm45]_S$ Laminates.....	144
58.	Maximum Longitudinal Strain during Cyclic Loading of a $[0,90,\pm45]_S$ Laminate.....	148
59.	Fiber Fractures at the Edge of a $[0,90_2]_S$ Laminate.....	150
60.	Fiber Fractures at an Interior Section of a $[0,90_2]_S$ Laminate.....	152
61.	Deplied Virgin $[0,90_2]_S$ Specimen.....	154
62.	Typical Fiber Break Pattern in 0 Degree Plies.....	155
63.	Segregation of Fiber Breaks in the 0 Degree Ply of a $[0,90_2]_S$ Laminate.....	157
64.	Example of a Gold Chloride Crack Trace.....	158
65.	Total Fiber Breaks in $[0,90_2]_S$ Laminates.....	161
66.	Fan of Influence of Cracks on Fiber Fractures.....	163
67.	Distribution of Multiplets in $[0,90_2]_S$ Laminates.....	165
68.	Mixed Mode of Fiber Fracture in $[0,\pm45]_S$ Laminates.....	169
69.	In-plane Stresses for a $[0,\pm45]_S$ Laminate Loaded to 1000 lbf in Uniaxial Tension.....	171
70.	Model of Fiber Fracture by In-plane Cracks	172
71.	Total Fiber Fractures in $[0,90,\pm45]_S$ Laminates.....	174
72.	Distribution of Multiplets in $[0,90,\pm45]_S$ Laminates....	176
73.	Fiber Fracture Mode in $[0,90,\pm45]_S$ Laminates.....	178
A-1	Example of a Reflectorized Grating on a Graphite/ Epoxy Specimen.....	205
A-2	Moiré Interferometry Optical Arrangement.....	207
A-3	Moiré Interferometry Optical/Loading Machine Arrangement.....	212
A-4	Moiré Fringe Pattern for a $[0_2]_S$ E-Glass/ Epoxy Specimen with a Center Notch.....	214

A-5	Moiré Fringe Pattern for a $[0,90_3]_S$ E-Glass/ Epoxy Specimen.....	215
A-6	Schematic of a Specimen with an Imbedded Flaw.....	217
A-7	Moiré Fringe Pattern for a $[0,90,0]_S$ Graphite/ Epoxy Specimen with an Imbedded Flaw.....	218
A-8	Moiré Fringe Pattern for a $[0,90_2]_S$ Graphite/ Epoxy Specimen after 400,000 Cycles of Fatigue Loading.	220

LIST OF TABLES

<u>TABLE</u>	<u>PAGE</u>
1. Zero Degree Ply Stresses for an Applied Laminate Stress of 10 ksi (69 MPa).....	23
2. Room Temperature Nominal Mechanical Properties of T300/5208 Graphite/Epoxy Laminates.....	25
3. Properties and Cure Data for T300/5208 Graphite/Epoxy Material.....	28
4. Average Measured Laminate Properties.....	33
5. Calculated and Measured Laminate Stiffness Reduction due to Ply Cracking and Delamination.....	137
6. Comparison of Laminate Strength Margins.....	178

I. INTRODUCTION

Understanding how and why structural materials fail is a fundamental requirement for intelligent engineering design. For fiber reinforced composite materials, a class of materials widely recognized to possess unique and extraordinary structural properties, this understanding has not yet developed. This lack of understanding is neither an indictment of the material nor of the many investigators who have addressed the problem. It is, instead, a reflection of the complexity of damage initiation and development mechanisms which characterize failure in composite materials.

While failure in homogeneous materials can frequently be viewed in terms of self-similar crack growth, the failure of composite materials cannot generally be associated with single flaw growth, and the analytical equivalent of linear elastic fracture mechanics (LEFM) is not available to predict static strength or fatigue life of composites. The role of composite material inhomogeneity in influencing damage development is an undeniable reality which must be considered in the development of any analytical scheme to predict failure.

It is necessary, then, to speak of a damage condition in a composite in terms of discrete, identifiable damage in the microstructural constituents: fiber, matrix, and fiber/matrix interface in each lamina and of the interface between laminae. In the case of fatigue damage it has been observed [1] that one needs to think of damage in terms of a collective condition rather than a collection. For given a well-defined collective condition, one can set boundary value problems

correctly and develop comprehensive models of behavior. Given a collection one is left with only emotional alternatives.

Although the issues of damage and failure are fundamental, there exist relatively few areas of general agreement. In considering fatigue damage and failure, it is generally agreed that fatigue damage consists of various combinations of matrix cracking, fiber-matrix debonding, delamination, void growth and local fiber breakage. Further, it is generally recognized that the mechanism, type and distribution of damage depends upon the material system (combination of fiber and matrix material), stacking sequence of plies, fabrication techniques, geometry, stress state, and loading history. Finally, most investigators acknowledge that the mechanisms are sensitive to one or more parameters including type of loading, frequency of cyclic loading, temperature, and moisture [2].

The philosophy is unsettled beyond this point. Two approaches can be identified. The first is deductive, wherein macroscopic measurements or phenomenological observations serve as the basis for the development of models which incorporate the microstructural role heuristically. That is, basic assumptions regarding the nature of the microstructure are made and damage modes are hypothesized. Failure is predicated on the development of one or more of these damage modes into a critical or unstable configuration from which failure somehow follows. Typically such models are evaluated in terms of stiffness reduction, residual strength, fatigue life, and fracture mode. Agreement with one or more sets of data is often taken as validation of the

model regardless of its limitations. Within this category would fall analyses based on the extension of linear elastic fracture mechanics to composite materials [3-16], extension of anisotropic yield criteria [17,18], cumulative damage models [19,20], stochastic fiber models [21-31], physical damage models [32-44], and post-failure analysis [45-57].

The second approach is inductive. Here, the microstructural damage modes are viewed as primitive elements of a framework within which global phenomena can be explained and upon which rational predictions can be assembled for the general case. This approach admits no intuitions regarding damage except those which can be substantiated by observation. Damage models, indispensable in any analytical formulation, are developed from carefully designed leading experiments in which the effect of specific observable damage on macroscopic properties can be assessed and generalized. In this category is work dealing with the role of matrix cracking [58-60], delamination [61,62], fiber fracture [63-65], and edge damage [66-68]. Also included is work dealing with the influence of external variables on the development of damage: cyclic loading frequency [72,73], specimen size [22,27,30], manufacturing defects [75], and environment [76].

The basic attribute of the inductive approach is that the philosophy of composite failure can only be developed from a complete understanding of the damage state which precipitates it. It is to this understanding that the present work makes its major contribution.

An experimental investigation was undertaken to establish the sequence and pattern of damage development in certain laminates of graphite/epoxy material subjected to tension-tension cyclic loading. The laminate types were $[0,90_2]_s$, $[0,\pm 45]_s$, and $[0,90,\pm 45]_s$. They were selected to represent widely different interlaminar constraint situations and (by anticipation) different primary damage modes. The material, T300/5208 graphite/epoxy, was chosen because of its widespread use in aerospace applications. Damage was observed and analyzed using two principal methods--X-ray radiography and light and electron microscopy. A damage analogue in the form of dynamic laminate secant modulus reduction [5,77-80] was used to monitor the state of integrated fatigue damage and to provide a basis for interrupting the fatigue process at desired damage levels prior to failure.

The present study concentrated on the advanced damage regime associated with long life-engineering stress level situations, i.e., damage states that develop subsequent to development of the characteristic damage state for matrix cracking [58-60]. The advanced damage state of each laminate type was characterized and the damage mechanisms were evaluated in terms of the associated local or global stress fields. An item of particular interest was the influence of matrix cracking in off-axis plies on fiber fracture in adjacent plies.

Results of this study include documentation and analysis of the stages of fatigue damage development in terms of laminate stiffness reduction; identification of several unique damage types heretofore not identified in the literature; and an examination of edge-related

fiber damage; a demonstration of the influence of ply cracking on the location of adjacent ply fiber fracture and of the influence of the lamina stress state upon the mode of fiber fracture, and the establishment of the density and statistical distribution of single and multiple fiber fractures in these laminates.

Chapter II provides a survey of literature dealing with damage development in composites and with the broader issue of composite failure. Chapter III describes the philosophy and methods of the experimental work. Chapter IV describes and discusses the results for each laminate type. The conclusions and summary of the work are contained in Chapter V. An appendix describes the application of moiré interferometry as a nondestructive interrogative tool for the observation of damage development in situ and in real time. Some preliminary results with notched and unnotched E-glass/epoxy laminates and some of the laminates used in the fatigue damage study are reported there also.

II. LITERATURE REVIEW

Perhaps no single area of recent research in composite materials has attracted the attention of more workers in the field than failure analysis. Because of the complexity of the problem, of predicting failure based on the damage condition which precedes it, a consensus philosophy and methodology to be applied to achieve a solution has not yet been established. As a result, the literature in this area is extensive and diverse. It shall be the purpose of this chapter to review the work in this area which is pertinent to the present report, dealing not only with fatigue damage mechanisms but also the broader issue of composite material failure, viewed both analytically and experimentally.

There exists in the literature a number of excellent overview articles dealing with fatigue of composite materials. Reifsnider [1] examined the fatigue behavior of composite materials in terms of their anisotropic, inhomogeneous character and pointed out the futility of attempting to extend concepts derived from fatigue of isotropic, homogeneous materials to this class of materials. He also considered the means by which the complex nature of fatigue damage in composite materials can be ordered, not as a collection of disconnected entities but rather as elements of a collective condition. It is the latter viewpoint, he suggests, that provides a rational framework for properly setting mechanics boundary value problems and for ultimately developing a comprehensive model of fatigue behavior. Stinchcomb and Reifsnider [2] provided a comprehensive survey of activity dedicated

to developing and understanding basic fatigue mechanisms in both notched and unnotched composite laminates, and observed that this represents a rather small part of the overall fatigue literature. Their review included primarily experimental work dealing with the characterization of fatigue-induced damage at the microstructural level and the effects of external variables such as moisture, temperature, frequency of cycling, and modes of loading on this damage.

Owen [81] examined fatigue in composite materials using simple fiber-matrix models to determine the relative merits of combinations of fiber and matrix properties. In approaching the problem as one of design for damage tolerance rather than damage avoidance, he identified a number of intuitive concepts regarding matrix ductility on interfacial strength which do not hold up to even elementary micro-mechanics analysis. Hahn and Kim [82] provided a thorough treatment of the fatigue behavior of a $[0, \pm 45, 90]_s$ glass/epoxy laminate. Among other things, they investigated static properties, S-N relationship, thickness variation, damage initiation and growth, temperature increase, and secant modulus change. One of their conclusions was that the primary process responsible for fatigue failure of laminates having lifetimes on the order of 10^6 cycles was that of matrix "wear-out" followed by chance failure of the fibers.

Reifsnider [58] examined the mechanics of damage development and failure for notched and unnotched materials beginning with lamina behavior and proceeding to laminate behavior. He introduced the

concept of a characteristic damage state as a prefracture condition from which fracture models might be developed, and drew an analogy with the familiar single crack condition in homogeneous materials. Hahn [83] reviewed the effects of constant amplitude cyclic loading on uniaxial and multiaxial laminates. He provided an excellent analytical treatment of longitudinal cracking in 0 degree plies for both cases as well as other subcritical damage, and attempted to relate these to changes in strength and stiffness.

Harris [84] reviewed the state of knowledge of composite fatigue and suggested that matrix and interface damage represent the weak link as far as fatigue resistance is concerned inasmuch as local matrix fatigue failures are, in his opinion, the predominant contributor to composite fatigue failure.

There have been a number of contributions to the recent literature involving the observation and experimental characterization of fatigue damage in composite materials. In this area there has been in the author's opinion, some unevenness. In some cases there appears to be a tendency to simply report observations of damage for specified conditions with little or no analysis of the cause of the damage in terms of the loading, geometry, laminate stacking sequence, et cetera, or its effect upon fatigue behavior. Such ad hoc observation and conjectural analysis is not likely to lead to a fundamental understanding of the effect of such damage upon composite strength, stiffness, and life.

Several investigators have studied specific aspects of the broader problem of damage development and have produced thorough and critical treatments. Awerbach and Hahn [85] examined the role of matrix and interface damage on failure of unidirectional, off-axis graphite/epoxy specimens under combined-stress fatigue loading in order to understand ply failure in more complicated laminates. By the use of stereoptical techniques they concluded that several interdependent failure modes (fracture of individual fibers, matrix separation or shear failure in the matrix, matrix cleavage, and matrix/interface cracking parallel to fibers) act to produce overall failure of these specimens. Similar work and results were reported by Sinclair and Chamis [47-49].

Reifsnider, et al. [59], Masters [60], and Bader, et al. [86] have examined the formation of cracks in the off-axis plies. Reifsnider identified the existence of a "characteristic damage state," a condition in which a saturation of cracking is ultimately achieved in both static and cyclic loading and for which a characteristic spacing of cracks is observed and can be predicted from a simple one-dimensional shear-lag analysis. This characteristic damage state is independent of load history, including thermal and hygroscopic effects and depends only upon the material, geometry, and stacking sequence. Bader subsequently reported similar results.

Stinchcomb, et al. [72] have examined the effect of cyclic frequency on the fatigue damage modes in boron/epoxy material. They identified a marked frequency dependence of mechanical response which

they attributed to a time-at-load influence on the development of damage in the matrix material. Stinchcomb, et al. [74] have also studied the effects of ply constraint on fatigue damage development in composite materials. They concluded that constraint situations which produce the greatest static strength do not minimize the extent of damage that develops during cyclic loading; and, likewise, constraints which lead to minimum damage situations do not conform to maximum strength cases. They also observed that the out-of-plane stresses produced by constraints are influential on the growth of damage along ply interfaces, especially during cyclic loading. Finally, they determined that through-the-thickness constraint controls the pattern and spacing of cracks in the characteristic damage state which in turn determines the state of stress in the damaged laminate.

O'Brien [62] has quantitatively described the onset and growth of delaminations in certain stacking sequences of graphite/epoxy laminates. He determined that the laminate stiffness decreased linearly with increasing delamination size. By computing the strain energy release rate, G , he was able to calculate a critical value, G_c , for delamination onset. He proposed a power law correlation between G and the delamination growth rate in fatigue.

Except for the classical work of Rosen [21] in which he proposed the ineffective length model to predict lamina fracture and the early work by Herring, et al. [65] with crack growth in a unidirectional boron/aluminum composite which yielded some quite remarkable radiographs, most fiber fracture investigations have been of the

post-failure fractographic nature. An exception is work reported by Reifsnider, et al. [63] in which scanning electron micrographs of edge replicas were analyzed to determine patterns of fiber breaks at the edge of fatigue-damaged graphite/epoxy specimens. Freeman [87] has also observed damage including broken fibers around holes in fatigue loaded graphite/epoxy specimens using a light microscope to observe individual laminae which had been "deplied" from the laminate. This deply process was accomplished by heating the laminate to a temperature sufficient to pyrolyze the resin matrix and thereby eliminate the interlaminar bond. Recently, Jamison [64] has observed fiber fracture in similarly deplyed laminae from unnotched laminates by scanning electron microscopy (SEM).

Analytical treatments of fiber fracture are typically statistical in nature. The groundwork for predicting tensile failure of a composite lamina in terms of the strength of the constituent fibers was provided by Rosen [21], who proposed the chain of bundles model and introduced the fiber ineffective length concept. In a subsequent related paper, Zweben [22] extended the model to account for multiple contiguous fiber breaks using the stress transfer scheme of Hedgepeth [29]. Zweben also suggested that two general modes of composite failure exist--a cumulative mode in which damage including fiber breaks develops globally prior to failure, and a non-cumulative mode in which little fiber fracture occurs prior to fracture. These modes were later observed experimentally by Herring [65]. Zweben and Rosen [23] discussed crack growth in unidirectional composites taking into

account stress concentrations in nearest fibers and expressed the expected number of multiple breaks of various orders as functions of stress.

Harlow and Phoenix [24,25] extended the chain-of-bundles model to produce an essentially exact solution and concluded that the Weibull shape and scale parameters for the composite strength are different from those of the fibers which make up the composite. Tamuzs [31] treated the accumulation of contiguous fiber breaks in a unidirectional composite as the growth of a penny-shaped crack. In his analysis, failure occurred when the fracture of one additional fiber in a multiplet of breaks occurred to produce an unstable arrangement. Batdorf [26] abandoned the chain-of-bundles model in favor of a Griffith-type instability treatment of a "crack" representing multiple adjacent fiber breaks. His treatment is conceptually and analytically simpler than the treatment of Phoenix and Harlow yet yields similar predictions. Additionally it can be extended to the three-dimensional case.

Tamuzs [30,31] has analyzed the time-dependent fracture of composites at constant load by introducing the concept of time-dependent fiber strength and has proposed a kinetic model of cumulative defects. He has also reported a size effect in cumulative damage development in which final failure in large specimens occurs at lower densities of accumulated damage than in smaller specimens. This phenomenon was also predicted by Zweben [22] and Batdorf [27].

Within the literature which can be broadly classified as post-fracture analysis, some type of "fractographic" technique is often

employed. Purslow [54] provided an excellent treatment of the fundamental aspects of composite fracture surface analysis. He conducted a fractographic characterization of carbon fiber reinforced plastic laminates and by interpretation of fracture surface features he contended that the fracture modes, failure sequence and the initiation site for failure could be identified. Morris [55] applied SEM fractography to graphite/epoxy specimens having known failure directions and, by observing features (which he termed "hackles") in the epoxy fracture surface, he found that the direction of overlap or tilt of these hackles indicated the initiation site and direction of failure.

Williams and Reifsnider [56] used SEM fractography to assess the role of matrix damage in fatigue failure of two boron fiber composites. They reported distinct differences between static and fatigue damage and between high and low cyclic frequencies, both in the type of damage and in the order of occurrence and modes of propagation. Kline and Chang [57] used both light and electron microscopy and X-ray radiography to study tension-tension fatigue failure of notched graphite/epoxy laminates. Their observations of hackle structures were similar to those of Morris. They observed cleavage-like branched structures in between fibers and suggested that they resulted from fiber-matrix interfacial stress due to differences in elastic properties. They also observed that these cracks appeared to be the inverse image of hackles, suggesting a source for the latter structure.

Sinclair and Chamis [47-49] examined fracture surfaces of off-axis specimens of graphite/epoxy material and classified them according to stress state: fiber tensile fracture for fiber orientations between 0 and 5 degrees; interlaminar shear stress fracture for fiber orientations between 5 and 15 degrees; transverse tensile stress fracture for fiber orientations between 45 and 90 degrees; and mixed mode fracture, a combination of intralaminar shear and transverse tensile stress which can occur for angles between 15 and 45 degrees.

Rotem and Hashin [46] have studied the failure of balanced angle ply laminates of E-glass/epoxy material. By using transmitted light to observe cracks and delaminations, they identified three distinct modes of failure. For ply angles between 0 and 40 degrees, failure was due to delamination; for angles between 40 and 50 degrees, failure was by ply cracking; and for angles greater than 50 degrees, by a single crack parallel to the fibers, a more local phenomenon.

Bailey and Parvizi [45] studied the role of fiber debonding in the failure of cross-ply glass fiber composites. Using a strain stage in an SEM they directly observed fiber-matrix debonding in transverse plies. They reported that in $[0,90,0]$ laminates fiber-matrix debonding preceded transverse cracking in 90° plies and occurred at strains as low as 0.1 percent. They noted that visible whitening of the matrix and a small modulus change appeared to be associated with debonding in glass fiber epoxy systems. They concluded that

transverse cracks in this material developed by formation and coalescence of fiber-matrix debonds.

Damage which develops at free edges of composites has been examined both experimentally and analytically by a number of investigators. The study of the role of interlaminar stresses in edge delamination which accounts for much of this literature was begun by Pagano and Pipes [69-71]. They identified the role of laminate stacking sequence in producing states of interlaminar shear and normal stress which either encouraged or resisted the initiation and growth of edge delaminations. Herakovich [67] has further analyzed the stacking sequence effect in terms of the elastic properties of the material and has established a rank ordering of the stacking sequence combinations for a quasi-isotropic graphite/epoxy laminate based on the magnitudes of elastic property differences at adjacent plies. Crossman [68] used a finite element analysis to compute interlaminar stresses at the free edge of graphite/epoxy laminates under tensile loads and correctly predicted the interlaminar location of the first delaminations, but did not predict subsequent delaminations which occurred at other interfaces.

Edge studies have been undertaken not only to investigate edge delamination but also other damage modes as well. Stalnaker and Stinchcomb [66] followed the progression of fatigue damage in two different quasi-isotropic stacking sequences of graphite/epoxy material as a function of load history using a surface replication technique. They observed that the formation of cracks in off-axis plies and

delaminations between plies were dependent upon the stacking sequence. They also observed that a stable crack density was eventually reached in each lamina and that the measure of this characteristic spacing in each ply was dependent upon the stacking sequence but not upon the cyclic stress level.

Wang and Wang [32] used a full-width surface notch in laminates of E-glass/epoxy material to study delamination growth during tension-tension cyclic loading. They observed that delamination was a matrix-dominated process in which the interlaminar crack traveled within the resin-rich zone. They noted a strong correlation between delamination growth rate and the range of cyclic stress intensity factors and proposed a power law for delamination growth rate.

There are numerous analytical treatments of composite damage accumulation and failure, apart from those dealing with the statistics of fiber fracture. Those which are discussed in the following paragraphs do not, by any measure, represent the complete set but are, in the author's opinion, representative of general categories of these analyses. Some analysis efforts deal with modeling specific damage mechanisms. Wang, et al. [37] used the concept of strain energy release rate and a finite element analysis to model the development of multiple transverse cracks in graphite/epoxy laminates. Their analysis predicted both the critical applied stress for first cracking and the existence of a saturation spacing of transverse cracks. Reifsnider [88] had previously predicted this spacing using a simpler one-dimensional shear-lag analysis. Kelly [36] examined the same

phenomenon in cross-ply laminates and included the effects of curing stresses. He hypothesized the existence of longitudinal cracking from consideration of Poisson mismatch between plies and suggested that such splitting should be complete when the saturation condition in the transverse plies is achieved. Korczynskyj and Morley [34] approached the same problem with similar results by modeling the strain field about a crack of arbitrary length in a transverse ply.

Another type of analytical treatment is that which uses microstructural damage models as a basis for predicting macroscopic failure conditions. Hashin [38] took this approach to developing fatigue failure criteria for unidirectional fiber composites. He identified and separately modeled two distinct failure modes: a fiber mode and a matrix mode, the active mode being determined by the fiber angle of the laminate. The failure criteria took a tensor polynomial form in which strengths are functions of the fatigue-stress ratio and fatigue life. Nuismer [42] also modeled damage as being of two types occurring in repeating patterns: normal damage consisting of fiber breaks and matrix cracks normal to the fiber direction; and parallel damage consisting of longitudinal splitting and fiber-matrix debonding. He thereby introduced damage state variables into the ply constitutive relations which were then used in a laminated plate theory along with an unspecified failure criterion to predict laminate failure. He reported general agreement with a set of experimental data.

Tsai and Hahn [18] and Wu [17] have provided tutorial treatments of macroscopic failure predictions dealing generally with tensor polynomial formulations of failure criteria. Wu also provided an excellent treatment of fracture mechanics concepts applied first to anisotropic, and then to inhomogeneous materials.

A number of analytical treatments of the role of stress redistribution due to damage development have been reported. Kochetkov and Maksimov [33] have provided an analysis of stress redistribution in a unidirectional hybrid composite using a composite cylinders model to assess the changes in elastic modulus due to failure of fibers. Reifsnider and Talug [89] analyzed the stress fields in laminates in the presence of cracks using a quasi-three-dimensional finite difference scheme to solve a displacement-formulated classical elasticity problem. This analysis substantiated the characteristic damage state prediction of saturation crack spacing and provided a basis for the role of the altered stress state about these cracks on subsequent damage development.

Two analytical treatments of fatigue life have been reported. Chou and Croman [35] studied two models for residual strength--(i) a degradation model in which strength decreases with each cycle as a result of damage; and (ii) a sudden death model in which strength decrease occurs only in the last cycle and fatigue failure is governed by some mechanism other than residual strength. They found that the degradation model was a better predictor of residual strength for multi-directional laminates but that the sudden death model better

described unidirectional behavior. Chou [19] proposed a phenomenological cumulative damage rule for fatigue life using a percent failure of specimens basis rather than Miner's Rule. In this model, which was shown to agree reasonably well with a small set of experimental data, damage development is assumed to be independent of the sequence of cyclic loading.

Applications of linear elastic fracture mechanics to composite materials also make up a sizable part of the analytical treatments of composite failure. This work falls generally into two categories--(i) that which seeks to approach the question of fracture toughness of a composite in terms of the crack tip-microstructure interaction, viz Beaumont and Tetelman [3], Kreider and Dardi [4], Averbach and Hahn [5], and Poe [6]; (ii) those which apply LEFM concepts to the composite modeled as an anisotropic medium in which the material heterogeneity is either ignored or accommodated in "equivalent homogeneous" models. Some examples of this second category are those by Cook and Rau [7], Cruse and Konish [8], Maron and Johnson [9], Erdogan [10], Tsai and Hahn [11], Morris and Hahn [12], and Sih [13]. Several workers have provided overview treatments of the possible applications and limitations of LEFM in the study of composite fracture. Among the best of these, in the author's opinion, are those by Kanninen, et al. [14], Smith [15], and Zweben [16].

The relationship between reduction of stiffness and development of damage during fatigue of composites had been observed and studied by several investigators. O'Brien [90] and O'Brien and

Reifsnider [78] have described the stiffness reductions in boron/epoxy laminates in terms of reductions of the in-plane stiffness properties, E_{xx} , E_{yy} , and G_{xy} . They observed that damage modes differed distinctively according to lay-up and that the anisotropy of fatigue damage development among laminates having different stacking sequences was reflected in differing percentage changes in these stiffness properties. They also examined [77] the correlation between matrix damage and fiber fracture in boron/epoxy laminates with stiffness and strength reductions. In this study, the number of fractures due to cyclic loading was determined after acid-leaching of the epoxy resin matrix. They concluded that there was a strong correlation between static stiffness changes and matrix damage and that a weaker correlation existed between the reduction in strength and the number of fibers broken during fatigue prior to final fracture.

Hahn and Kim [82] proposed a secant modulus criterion for fatigue failure of composite laminates. The criterion, simply stated, was that fatigue failure would occur when the static stiffness measured during fatigue was degraded to the value of the secant modulus measured by a quasi-static ultimate strength test, regardless of the load history. The later work of O'Brien and Reifsnider [78], however, demonstrated that damage accumulation for a particular laminate during fatigue and static loading was different, i.e., load history could not be ignored and the secant modulus criterion was not generally applicable.

Highsmith and Reifsnider [79] have extended the work of O'Brien and Reifsnider, previously cited, in determining stiffness changes due to matrix cracks alone. They proposed a model for treating the problem analytically wherein elements of the lamina stiffness tensor are systematically reduced in relation to crack density and the laminate stiffness is then determined from a laminated plate theory. They reported good correlation with experimental results from both static and fatigue tests.

III. EXPERIMENTAL PROCEDURE

In order to study generic fatigue damage development in composite materials experimentally, two general conditions must be met. First, the choice of laminate stacking sequences used must span the range of interlaminar constraint conditions in order that observations and conclusions drawn from them can be generalized to the multilayered composite laminates used in practical structures. Second, some provision must be made for assessing damage development in a particular specimen during the course of cyclic loading using nondestructive methods so that the testing programs can be accomplished efficiently and economically. Without such a damage analogue to serve as a sentinel for control, the number of tests required to provide a sufficiently representative range of damage conditions using only S-N data could be prohibitive.

To satisfy the first of these conditions, three laminate stacking sequences were selected: $[0,90_2]_S$, $[0,\pm45]_S$, and $[0,90,\pm45]_S$. Each of these stacking sequences appear as repeating sublaminates in thicker structural laminates. Moreover, the in-plane stress state of the $[0,90_2]_S$ laminate subjected to uniaxial tensile loading in the 0 degree direction differs markedly from that of the $[0,\pm45]_S$ laminate, as do the laminate elastic properties. Table I shows the in-plane stresses in the 0 degree plies calculated from laminated plate theory for an applied laminate stress of 10 ksi (69 MPa). Residual thermal stresses corresponding to a cure temperature of 275°F (133°C) and operating temperature of 75°F (24°C) are included.

Table 1. Zero Degree Ply Stresses for an Applied Laminate Stress of 10 ksi (69 MPa).

Laminate Type	σ_1 (ksi) (MPa)	σ_2 (ksi) (MPa)	τ_{12} (ksi) (MPa)
$[0,90_2]_s$	19.4 (134)	4.2 (29)	0
$[0,\pm45]_s$	23.7 (163)	2.5 (17)	0
$[0,90,\pm45]_s$	22.5 (155)	3.6 (25)	0

Table II shows the initial elastic constants for each laminate. All values are calculated from a laminated plate theory using nominal lamina properties of T300/5208 graphite/epoxy material. Differences in the initial stress state and elastic properties would be expected to cause differences in damage development.

The role of interlaminar normal and shear stresses in the development and growth of delaminations has been recognized for some time [69-71]. Figure 1 shows the through-thickness variation of these stresses near the edge of each of the laminate types for an applied uniaxial tensile load, $N_x = 1000$ lbf. (4.45 kN). A finite element analysis was used to determine the values shown. Such information is useful in assessing the tendency of a particular stacking sequence to delaminate and in predicting the interface(s) at which such delaminations would most likely occur. A large tensile σ_z value or large value of τ_{zx} or τ_{zy} (of either sign), or a combination of moderate values of several of these stresses at one or more interfaces would suggest a tendency for delamination to occur. Inspection of Fig. 1 suggests a relatively higher probability of delamination for the $[0,90,\pm45]_s$ laminate because of high interlaminar shear stress than for the other laminate types despite the existence of a compressive interlaminar normal stress. The $[0,\pm45]_s$ laminate would appear to have the lowest tendency for delamination as a result of low interlaminar shear and normal stresses. On this basis, the selected laminate types represented a desirable range of delamination expectations.

Table 2. Room Temperature Nominal Mechanical Properties of
T300/5208 Graphite/Epoxy Laminates.

Laminate Type	Initial Elastic Properties			
	E_x (MSI) (GPa)	E_y (MSI) (GPa)	G_{xy} (MSI) (GPa)	ν_{xy}
$[0,90_2]_s$	7.9 (54)	14.3 (98.6)	0.9 (6)	0.03
$[0,\pm45]_s$	9.0 (62)	3.9 (27)	3.8 (26)	0.69
$[0,90,\pm45]_s$	8.1 (56)	8.1 (56)	3.1 (21)	0.30

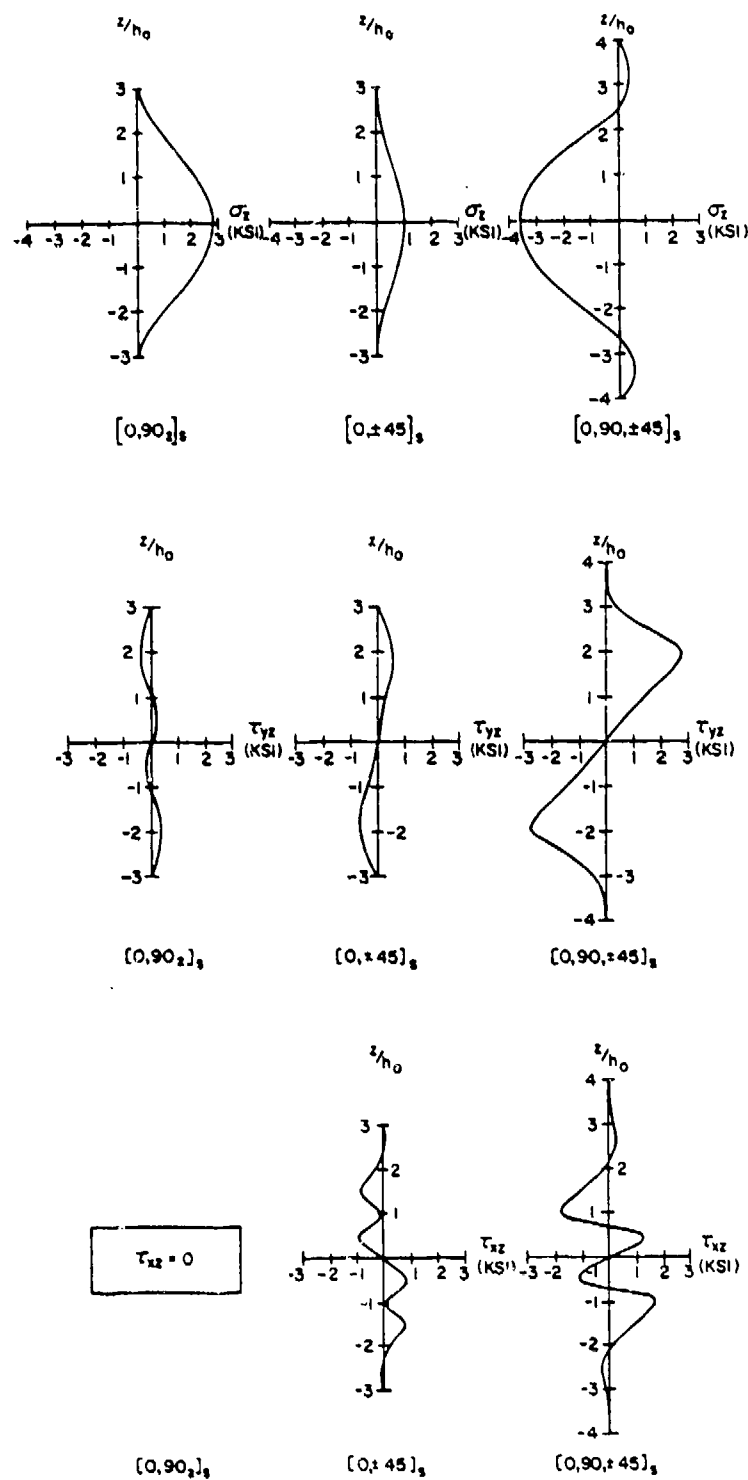


Figure 1. Interlaminar Shear and Normal Stresses.

The material used was T300/5208 graphite/epoxy manufactured by NARMCO Materials, Inc. and supplied in a prepreg form as 6 inch (152 mm) wide rolls. Table III lists nominal properties of the material along with cure cycle data. Laminated plates of this material were fabricated locally using a flat face press and the cure cycle described in Table III. Each plate was examined visually and by ultrasonic C-scan to assess its overall quality and to exclude regions of high porosity in cutting specimens from it. Specimens were cut from the plate using a circular saw with a diamond wheel. Specimen dimensions were 8 in. (203 mm) long and 1 in. (25.4 mm) wide. Thickness for the 6-ply laminates ($[0,90_2]_s$ and $[0,\pm45]_s$) was approximately 0.034 in. (0.86 mm); for the 8-ply laminate ($[0,90,\pm45]_s$), the thickness was 0.045 in. (1.1 mm). Width and thickness measurements were made with dial calipers for each specimen individually.

Some specimens to be examined by moiré interferometry (see Appendix) were 9 in. (229 mm) long and were provided with 1 3/4 in. (44.5 mm) end tabs to conform to a special specimen gripping arrangement for that purpose. The tabs were of the same material and stacking sequence as the specimen to which they were attached and were bonded with EPON 828/PACM 20 epoxy manufactured by Shell Chemical Company. All other specimens did not have end tabs. However the ends of the specimens (approximately 1 1/2 in. (38 mm)) were coated with a thin layer of MS 907 epoxy manufactured by Miller-Stephenson Chemical Company. This coating served to consolidate the surface fibers in the

Table 3. Properties and Cure Data¹ for T300/5208
Graphite/Epoxy Material

Ply Thickness before Fabrication (in.) (mm) ²	0.0075 (0.19)
Ply Thickness after Fabrication (in.) (mm) ²	0.0055 (0.14)
Fiber Volume Fraction (%) ²	66
Cure Temperature (°F) (°C)	275 (135)
Cure Pressure (psi) (MPa)	70 (0.5)
Cure Time (min.)	105
Post-cure Temperature (°F) (°C)	325 (163)
Post-cure Pressure (psi) (MPa)	70 (0.5)
Post-cure Time (min.)	120
Lamina Elastic Properties ³	
Longitudinal Modulus, E_1 (ksi)(GPa)	20.6 (142)
Transverse Modulus, E_2 (ksi)(GPa)	1.5 (10)
Shear Modulus, G_{12} (ksi)(GPa)	0.87 (6)
Poisson Ratio, ν_{12}	0.035

1. Supplied by manufacturer
2. Measured
3. Nominal values for T300/5208

0 degree plies and provide a more uniform gripping surface. Two thicknesses of 320 grit emery cloth were interposed between the machine grips and the specimens during fatigue loading to improve the gripping efficiency. The epoxy layer served to insulate the specimen from wear induced by this arrangement. The two specimen types are shown schematically in Fig. 2. Specimens were stored in a desicator cabinet between the time of fabrication and the time of use.

All static and cyclic tests were conducted on an MTS servo-controlled, closed loop testing machine operating in the load-controlled mode. Two types of grips were used. Initially, the fatigue testing of the $[0,90,\pm45]_S$ specimens was conducted using MTS hydraulic wedge-type grips having a 1 1/2 in. (38.1 mm) width capacity. Lateral alignment for 1 in. (25.4 mm) wide specimens was accomplished by using locally fabricated thin brass guides having outside dimensions of 1 1/2 in. and inside dimensions of 1 in. Although this arrangement was satisfactory for the $[0,90,\pm45]_S$ laminates, it proved to be unsatisfactory for the other laminate types. The combination of a slight, uncorrectable misalignment in one of the hydraulic grips and the reduced thickness and increased anisotropy of the $[0,90_2]_S$ and $[0,\pm45]_S$ laminates, produced unacceptable scatter in their observed fatigue behavior. Consequently, most of the cyclic testing of these laminate types was conducted on another MTS machine equipped with mechanical Instron grips having 1 in. wide wedges. Although difficulties associated with uniaxial loading of these thin

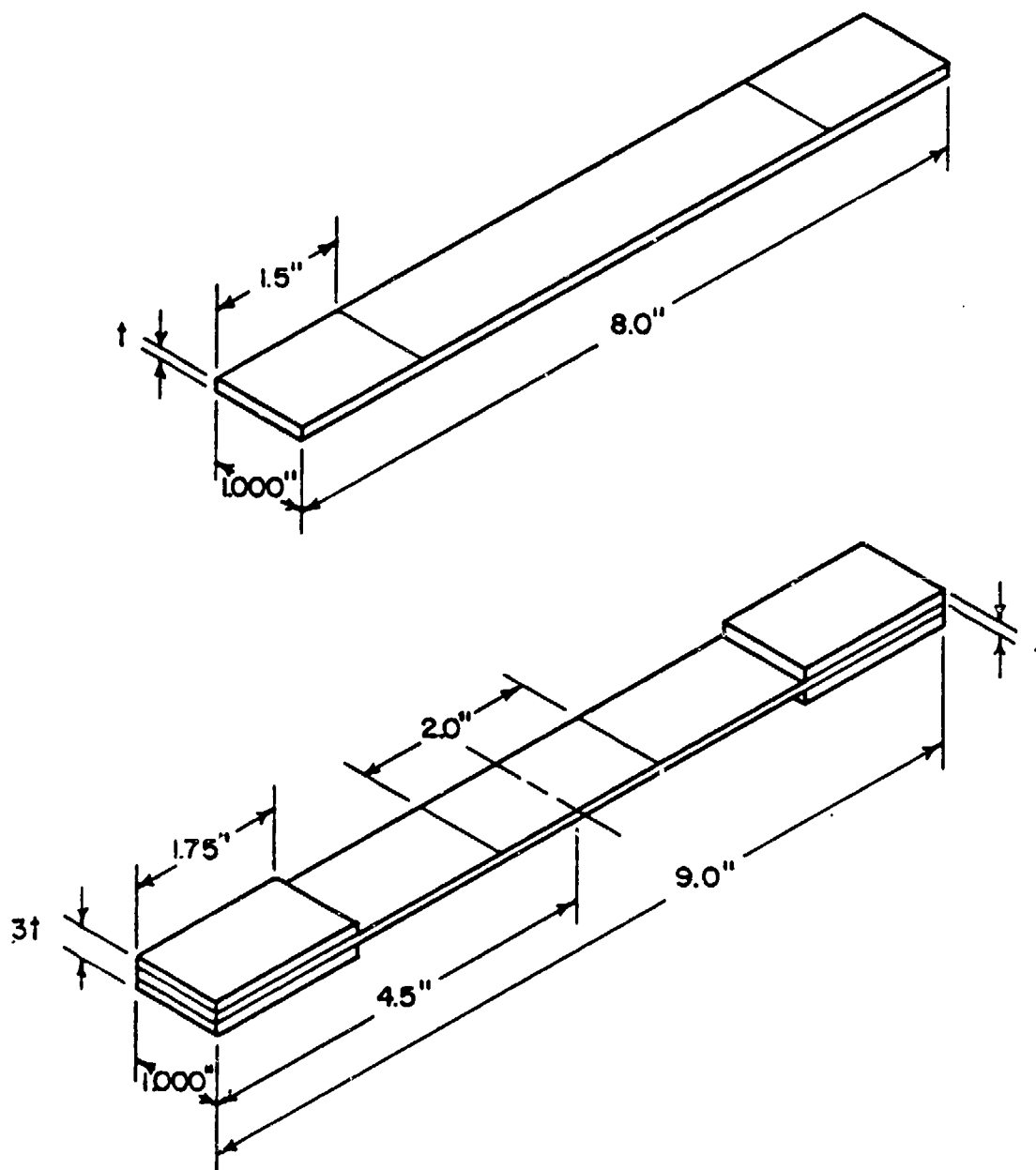


Figure 2. Specimen Types.

specimens was not entirely eliminated, a major difficulty was thereby avoided.

Continuous stiffness monitoring was an integral part of the damage development investigation. Stiffness was measured by means of an extensometer attached to one surface of the specimen. The extensometer gage length was nominally 2 in. (51 mm) and attachment was made to the center portion of the specimen. The extensometer knife edges sat in narrow, V-shaped channels machined into aluminum tabs. These tabs, measuring nominally 1/2 in. (13 mm) by 1/4 in. (6 mm) by 1/32 in. (0.8 mm), were in turn bonded to the specimen surface using RTV silicone rubber cement manufactured by 3-M Company. The arrangement is shown in Fig. 3.

The testing program for each of the three laminate types was the same and consisted of several phases. The first was the determination of the ultimate tensile strength, S_{ult} . These tests were conducted using the Instron mechanical wedge-type grips with the MTS machine in load-controlled mode at a loading rate of 20 lbf (0.09 N) per second. Strain was measured by two-element strain gages bonded to the center of the specimen using AE-1015 epoxy adhesive manufactured by Micro-Measurements Company. Load and longitudinal and transverse strains were recorded on a three channel plotter. Three tests for each laminate type were conducted. Average values of the results are shown in Table IV.

Using these measured ultimate tensile strength values, a series of preliminary fatigue tests was conducted to establish proper stress

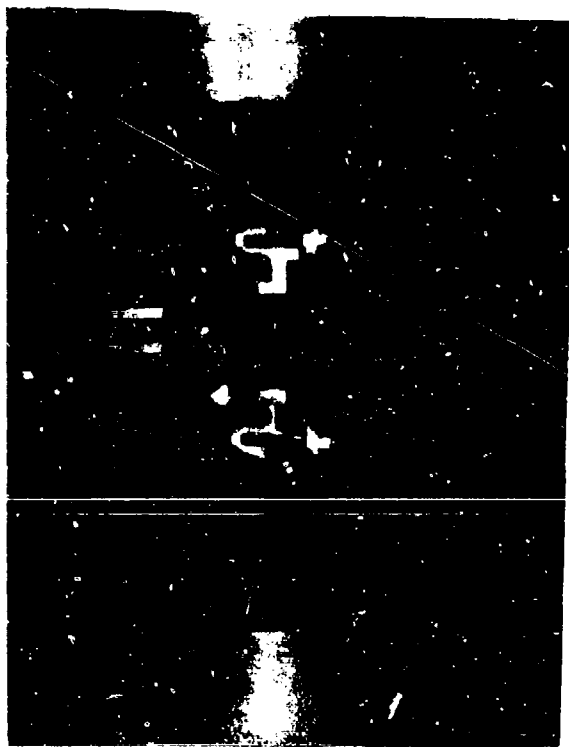


Figure 3. Specimen in the Testing Machine with Extensometer Mounted.

Table 4. Average Measured Laminate Properties.

Laminate Type	E_x (Avg) Msi (GPa)	ν_{xy} (Avg)	S_{ult} (Avg) Ksi (MPa)
$[0,90_2]_s$	$7.43(51.2) \pm 0.27(1.9)$	0.04	$81.2(560) \pm 5.3(37)$
$[0,\pm 45]_s$	$8.34(57.5) \pm 0.29(2.0)$	0.71 ± 0.01	$96.2(663) \pm 5.0(34)$
$[0,90,\pm 45]_s$	$7.67(52.9) \pm 0.22(1.5)$	---	$74.1(511) \pm 0.1(1)$

levels for subsequent tests. The aim was to determine the maximum cyclic stress level which would produce fatigue lifetimes on the order of 10^5 cycles and produce approximately the same maximum stresses in the 0 degree plies for each of the laminate types. The preliminary tests were conducted at a constant stress ratio, $R=0.1$, in a sinusoidal form at a cyclic frequency of 10 Hz in a tension-tension mode. The results of these tests provided the following working stresses, σ_{\max} , for each laminate type:

$$\begin{array}{ll} [0,90_2]_s, & \sigma_{\max} = 0.70 S_{ult} \\ [0,\pm 45]_s, & \sigma_{\max} = 0.72 S_{ult} \\ [0,90,\pm 45]_s, & \sigma_{\max} = 0.62 S_{ult} \end{array}$$

These maximum stress amplitudes were used in all subsequent tests.

Two series of fatigue tests were conducted for each laminate type. The first was designed to study the sequence of damage development in a single specimen by nondestructively evaluating its condition at intervals during its fatigue lifetime. For purposes of discussion, this type of test will be referred to hereafter as a "stop and go" test. The second series of tests was aimed at producing various levels of expected damage in a number of different specimens, each specimen characterizing a stage of stiffness reduction and associated damage. These specimens were both nondestructively and destructively examined by methods to be described.

The stop and go tests for each laminate type were conducted first. The procedure followed in both series was in fact identical in

the beginning steps. The specimen with extensometer tabs attached was aligned in the testing machine and the extensometer was attached using four small rubber bands looped around the specimen as fasteners. The extensometer output was set to zero and the specimen was slowly loaded under manual control to a tensile load of 1000 lbf (4.45kN). Load and strain were recorded by a two channel plotter so that an initial static elastic modulus could be calculated. The specimen was then slowly unloaded to zero load and reloaded manually to the load corresponding to the maximum fatigue stress amplitude to be used. Finally, the specimen was unloaded and the static elastic modulus following this fatigue half-cycle was measured as initially. The procedure is shown schematically in Fig. 4.

These modulus measurements provided a means by which initial and, for some laminate types, substantial stiffness reductions could be measured independently of the dynamic modulus measurement technique used during the fatigue test.

At this point the data acquisition system was initialized with specimen dimensions, calibration factors and other information required for control of calculation and output. The data acquisition system is shown schematically in Fig. 5. It consisted of a Z-80 microprocessor-based micro-computer with a CRT input/output device and line printer. It acquired data at a rate of 333 samples per second and provided output data every 12 seconds.

The specimen was slowly loaded to the mean cyclic stress and cyclic loading was begun at $R \approx 1.0$, i.e. a small variation in amplitude

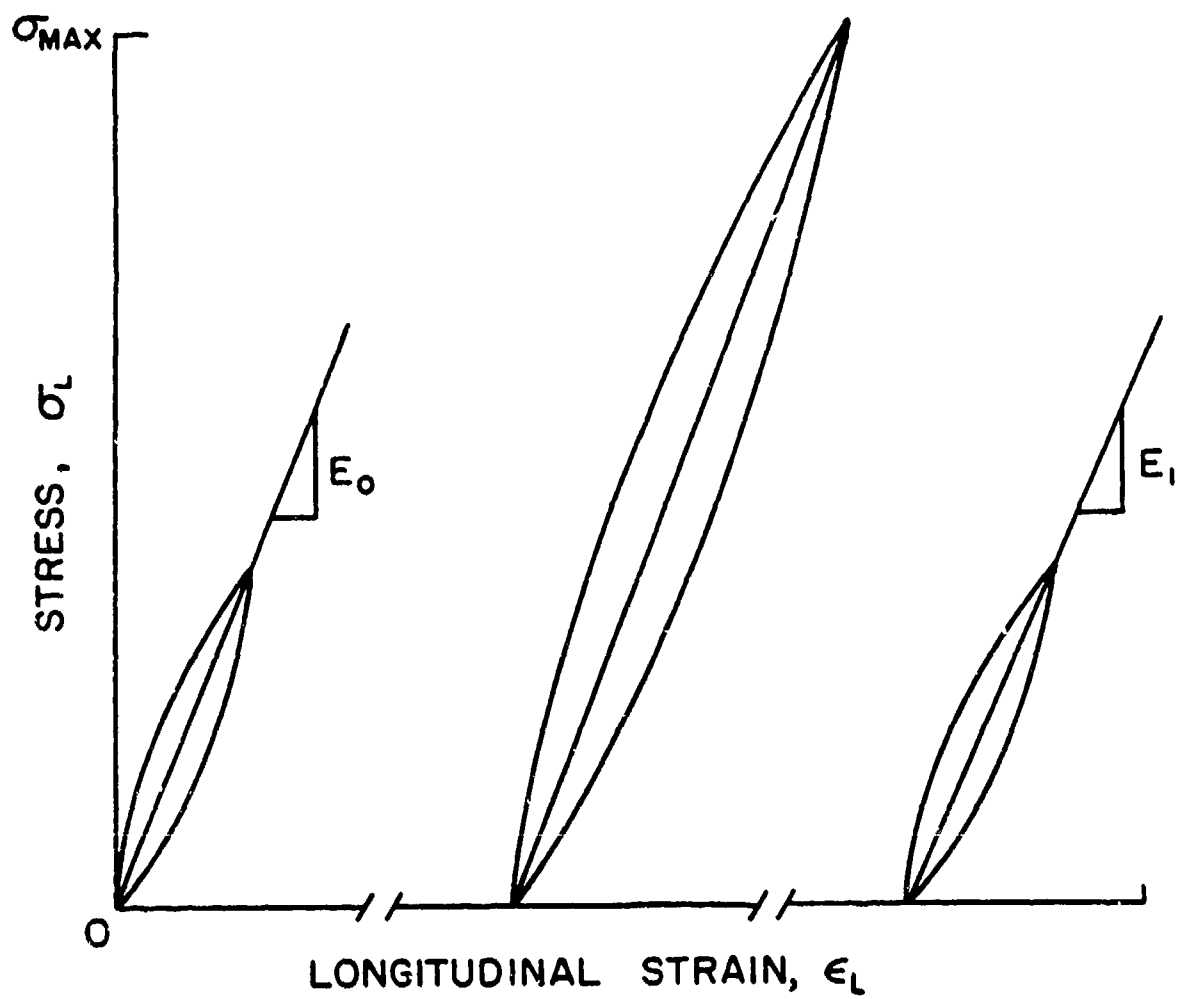


Figure 4. Initial Static Stiffness Measurement Procedure.

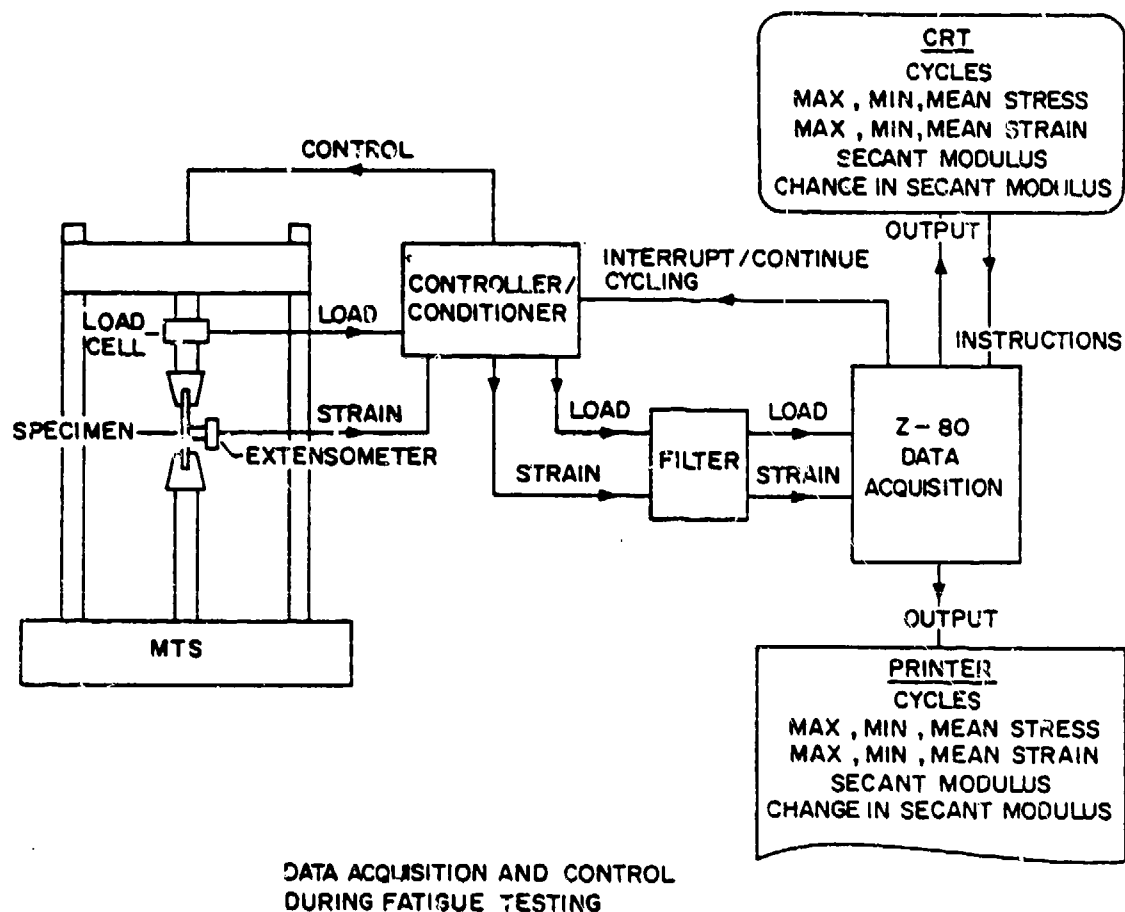


Figure 5. Data Acquisition and Control System.

of load. The span ($\sigma_{\max} - \sigma_{\min}$) was slowly adjusted until the desired σ_{\max} and $R=0.1$ were achieved. At this point the data acquisition system was instructed to begin acquiring data. This gradual fatigue initiation procedure was employed to avoid the possibility of initial specimen overload due to the difficulty of precisely matching preset static load limits to the dynamic levels required. The procedure required approximately 30 seconds or 300 cycles to complete, during which time stiffness data were not collected. Examination of initial rates of stiffness reduction for each laminate type indicated that this interval after the first cycle was not a significant contributor to overall measurement error.

Secant modulus reduction (the damage analogue) was monitored continuously during the tests and was plotted manually. Initial fatigue life tests had indicated that for each laminate type the shape of the dynamic secant modulus versus cycles curve was characteristic and generally displayed three distinct regions. A full discussion of the implications of these regions is central to the interpretation of damage development and necessarily will be deferred to a subsequent section. However, inasmuch as the procedures followed in both series of fatigue tests were based on this behavior, it is worthwhile at this point to define those regions. Region I is a region of rapid initial stiffness reduction; Region II is an intermediate region wherein the stiffness reduction occurs linearly with increasing cycles; and Region III is a region of final rapid stiffness reduction ending in specimen fracture.

It should be noted here that stiffness, which is a material property, and the dynamic secant modulus, which is a property determined by the dynamic stress-strain curve are not one and the same. Stiffness reduction is the more rational damage analogue; secant modulus change is simply a convenient, measurable related quantity. When static stiffness and dynamic secant modulus values were measured at the same point in a specimen's fatigue life, the dynamic secant modulus was typically higher by 2.5 to 4.9 percent, depending upon the laminate type. The two quantities were approximately equal for $[0,90_2]_s$ laminates. However, differences between secant modulus values at two points during a fatigue test did not differ significantly from quasi-static stiffness variations measured between the same two points. Consequently, when difference measurements are described and discussed, secant modulus changes will be taken to represent stiffness changes unless a special distinction must be made.

For the stop and go series of tests, the specimen was cyclically loaded until the stiffness versus cycles curve reached the apparent end of Region I. The specimen was then unloaded, reloaded to 1000 lbf (4.45 kN) and unloaded again so that a static stiffness measurement could be taken for comparison with the dynamic stiffness data. While at the load of 1000 lbf, a replica was made of each edge over a length of 1 in. (25 mm) near the specimen center. (The replication technique as well as other damage evaluation methods discussed will be described in detail in a subsequent section of this chapter.) Following replication, the specimen was removed from the testing machine and prepared

for X-ray radiography by the introduction of an X-ray opaque enhancing agent along the edges. Following X-ray radiography and a low-temperature heating cycle to drive off the enhancing agent liquid carrier, the specimen was returned to the testing machine and the fatigue loading procedure was repeated. During the examination phase, the extensometer mounting tabs were not removed. Data acquisition and stiffness monitoring proceeded until the next selected stiffness reduction level was reached. The examination procedure was then repeated. This stop and go process typically continued until the specimen failed in fatigue and stopping points were chosen frequently enough that each region of damage was included.

The stop and go series of tests had the advantage that it provided clear evidence of damage progression in a given specimen. This information was particularly useful in following the development of certain types of damage such as longitudinal splitting and delamination. The method had the disadvantage that there were largely uncontrollable extraneous factors involved such as specimen realignment, extensometer calibration and realignment, cyclic load reinitiation, introduction of a foreign substance (acetone for replication and an enhancing agent for radiography) which made quantitative interpretation of the total stiffness reduction and damage development difficult.

For this reason a complementary series of tests was conducted for each laminate type in which the specimen was cyclically loaded until a desired level of stiffness reduction (and by implication, damage

development) had occurred. At that point the specimen was subjected to first nondestructive and then microscopic analysis but was not subjected to additional fatigue cycles thereafter. This method required that a fairly large number of tests be conducted for each laminate type to provide a collection of damaged specimens which, taken together, were representative of the full range of damage development. Examination and analysis of damage conditions produced by each of these two test series form the basis of this investigation. In the following sections, details of the techniques employed in these tests are described.

Edge Replication

Replication is a technique by which surface topography is duplicated and made permanent in another medium. It has been used for a number of years to prepare thick specimens for transmission electron microscopy. Edge replication of composite specimens has been employed with considerable success in the study of ply cracking, delamination, and 0 degree fiber fracture [60,63,66]. In order to use the technique effectively for composite materials, the specimen edges must be polished. The polishing procedure followed is similar to that used in metallography. Successively finer grades of abrasives are used to produce a desirable level of surface smoothness. For this study, the abrasives were wetted 600 grit silicon carbide paper, followed by 5.0 μm alumina powder on a wetted felt cloth followed by 3.0 μm alumina powder on a wetted felt cloth. Each specimen edge was polished approximately 120 strokes at each polishing stage,

reversing the polishing direction every 30 strokes. The specimen was rinsed thoroughly between stages and, because the specimens were thin, was clamped between stiffener plates during polishing.

To produce a replica of a polished edge, a piece of cellulose acetate tape, 10 mils in thickness, is affixed to the specimen edge with adhesive tape. A small amount of acetone is injected between the tape and specimen and the tape is pressed quickly and lightly against the specimen edge. The acetate tape is allowed to harden for approximately one minute, and upon removal retains a permanent, high fidelity replica of the edge topography. The replica is then mounted and labelled on a glass plate for storage. Examination of the replica can be accomplished in several ways. One means is by use of a microfiche reader. When the glass plate containing the replica is inserted into the reader, magnifications on the order of 23X and 46X are provided. These are more than sufficient to distinguish the details of ply cracking and delamination which occur at the edge. In addition, replicas which have been coated with a thin conductive film of gold palladium can be observed at higher magnification and greater depth of field in a scanning electron microscope. This method provided a very useful means to study the development of fiber fractures at the edge in several laminates.

X-ray Radiography

X-ray radiography is perhaps the most widely used nondestructive evaluation technique aside from visual inspection for material characterization. In principle it provides images of material internal

structure by the selective absorption and transmission of X-ray radiation. Variations in X-ray absorption in a composite material can result from the presence of voids, cracks, delaminations, inclusions, or manufacturing flaws. For the study of damage development, then, it is a potentially valuable interrogative tool. However, variations in X-ray radiation absorptivity among the classes of damage and defects mentioned are often slight and difficult to resolve in the X-ray image. As a result, it has become common practice in the radiography of composite materials to apply an enhancing agent along the specimen edges. There are a number of these agents in use both in research and commercially--tetrabromoethane, diiodobutane, diiodomethane, and zinc iodide are some examples. All are both diffusive and opaque to X-rays and consequently appear distinctly in X-ray images. However, many of these agents, including the first three listed above, are derivatives of halogenated organic compounds and are quite toxic. Zinc iodide, however, is not toxic to humans and has been shown to compare favorably with other enhancing agents in both penetration and opacity [91]. The influence of zinc iodide on the mechanical response of graphite/epoxy has also been investigated [91]. No influence was observed. The present investigator has compared the effectiveness of tetrabromoethane and zinc iodide and found no observable difference for the applications required in this study. Consequently, zinc iodide was chosen as the enhancing agent for all radiography.

The zinc iodide solution consisted of 60 g of zinc iodide, 10 ml of water, 10 ml of isopropyl alcohol and 10 ml of Kodak

"Photo-Flo 600" as a wetting agent. Although this solution is quite diffusive into the damage regions of graphite/epoxy material, it was found that infiltration into these regions could be measurably improved by applying the zinc iodide while the specimen was under a tensile load. The loading served to reopen off-axis cracks and provided a broader channel for the ingress of the agent. It was also found that penetration was improved when the zinc iodide was applied along the specimen edge with the specimen in a horizontal position. Both were accomplished by using the arrangement shown in Fig. 6. The specimen was clamped in the loading fixture as shown with one specimen edge uppermost. The specimen was then loaded to approximately 300 lbf (1.3 kN). Two strips of adhesive tape extending approximately 1/4 in. (6 mm) above the edge were fastened to the specimen surfaces. Plates were clamped over the tape flush with the edge to ensure a seal with the surface, and the ends of the tape were crimped shut. A small amount of stopcock grease was injected at each end to provide a viscous plug. The channel thus formed was filled with zinc iodide which was allowed to remain at least 30 minutes. The residue was then removed and the surface and edges were cleaned with acetone to remove all superficial zinc iodide from the specimen.

Radiographs of the specimens were made immediately after zinc iodide treatment using a Hewlett-Packard Model 43805N Faxitron Series X-ray unit. The nominal film-to-source distance was 18 in. (460 mm). By a series of preliminary trials, the optimum operating voltage for the laminates used was found to be 25kV. The source

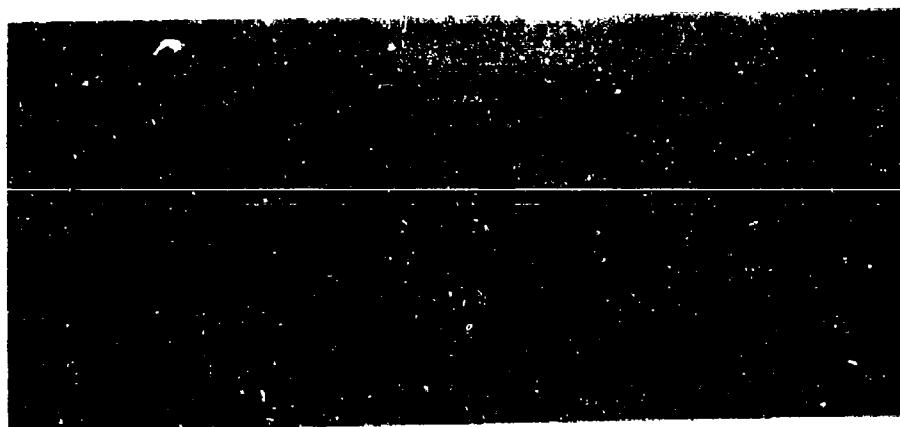


Figure 6. Loading Fixture for the Application of X-ray Enhancing Agent.

current was approximately 2.5 ma. The film used was Kodak Industrex R-type, single emulsion and high resolution. For those operating conditions, exposure times were 0.45 minutes for the 6-ply laminates, and 0.60 minutes for the 8-ply laminates. X-ray negatives were normally used for analysis. A light table and a 5X magnifying lens were sufficient for preliminary examination.

Radiography by its nature produces images which integrate information along the dimension of the specimen parallel to the X-ray beam. Hence, interpretation of damage existing at different levels and which overlap in the X-ray image is difficult. Moreover, it is not normally possible to associate a given damage condition with the ply in which it is located. This deficiency is particularly severe in the study of delamination growth, in which interface location is of primary interest.

However, the method of stereo X-ray radiography can be used to effectively resolve radiographic detail through the specimen thickness. The principle involved follows directly from the optical analogue. Because of the unique benefits derived from its three-dimensional image, the stereoptical method was applied to nearly all of the radiographs made during this investigation. The principle and its application are described in the following section.

Stereo X-ray Radiography

A number of techniques can be used to accomplish the three-dimensional stereoscopic effect [92]. In each, two images of the specimen are made, one differing slightly in orientation from the other. When

the two images are observed independently, one image to each eye, the viewer perceives the misorientation as an indication of depth and can distinguish "near" from "far" detail. The principle applies whether the images are photographic or radiographic.

The technique chosen for this work to provide the required orientation differences was that of specimen tilt, shown schematically in Fig. 7. The first radiographic image is made with the specimen surface normal parallel to the X-ray beam. The specimen rests directly on the X-ray film and the image is true size. For the second image, the exposed film is exchanged for an unexposed sheet and the platform is tilted so that the specimen film normal is rotated through a small angle, ϕ , relative to the X-ray beam axis. The second exposure is made in this rotated orientation.

The angle, ϕ , is related to the angle formed by the left and right eye when the observer is viewing an object at a fixed distance--the smaller the angle, the greater the perceived distance. For light stereoscopy a typical choice is 6 to 8 degrees. For radiographic stereoscopy of thin specimens, an angle of approximately 15 degrees was found to be optimum. The value itself does not appear to be critical although significantly larger or smaller angles can produce image distortion or result in eyestrain in viewing.

For the purposes of this work, it was found that it was desirable to incline the specimen approximately 6 degrees so that transverse cracks which otherwise would appear as edges in both images would have a small aspect. Details of these cracks in the radiographs were

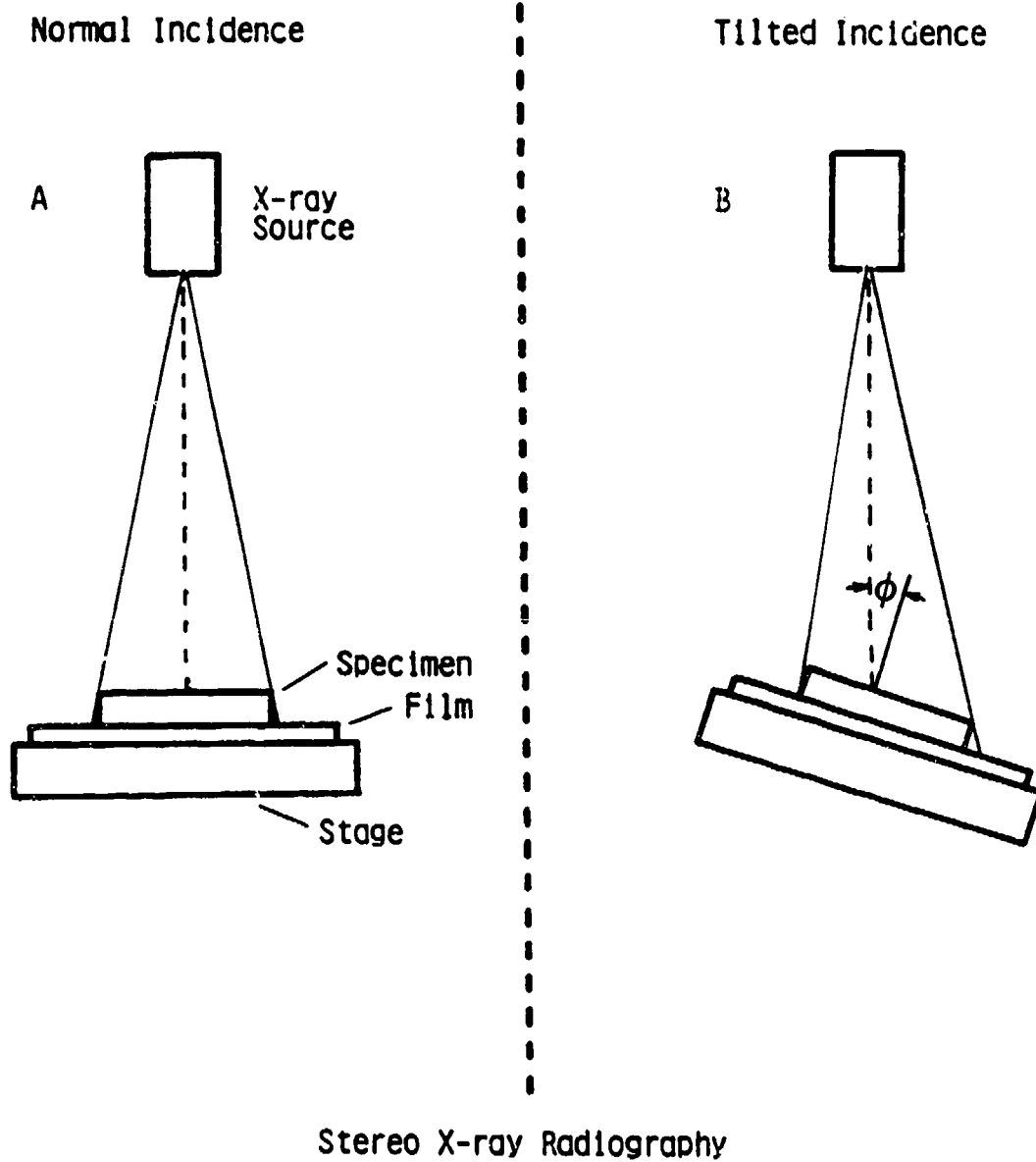


Figure 7. Tilt Method of Stereo X-Ray Radiography.

thereby enhanced. The fixture used to accomplish specimen tilt and rotation was locally constructed and is shown in Fig. 8. Viewing of the stereoptical pair of images generally requires the use of a device which confines the view of each eye to one image. Some of the devices are quite simple and provide magnification between 2X and 4X. Others are more complex and more versatile. For viewing stereoscopic radiographs used in this investigation, a Bausch and Lomb Versatile Stereoscope Model 5399-8712 was acquired. This instrument, which is normally used in aerial photogrammetry, provides microscopic stereoscopy. It was attached to a Richards Model GFL 940-MC light table equipped with rails which provided for two directions of translation of the instrument. The arrangement is shown in Fig. 9. The true size radiographic negatives were placed on the light table, one aligned with each of the instrument prism areas. The images were viewed through binocular eyepieces and aligned. (A small silver paint dot was placed on the specimen surface prior to radiography to serve as an alignment fiducial.) When alignment was achieved, the viewer was provided with a remarkable perception of depth in which the relative position of dominant features in the image could be resolved without difficulty. With experience, even subtle detail could be resolved in three dimensions.

With alignment achieved, the magnification could be changed and the instrument could be translated to different regions of the image, both without loss of the three-dimensional perception. The total

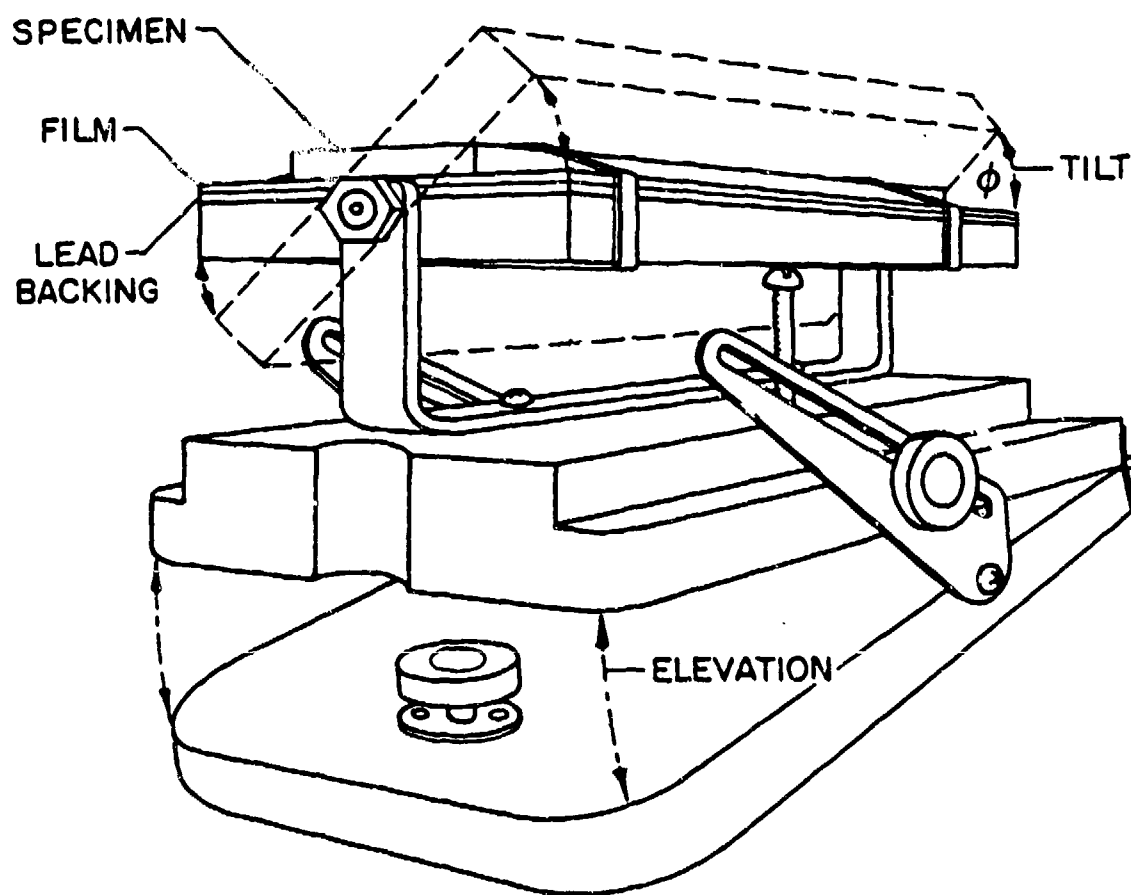


Figure 8. Stereo X-ray Radiography Tilting Fixture.

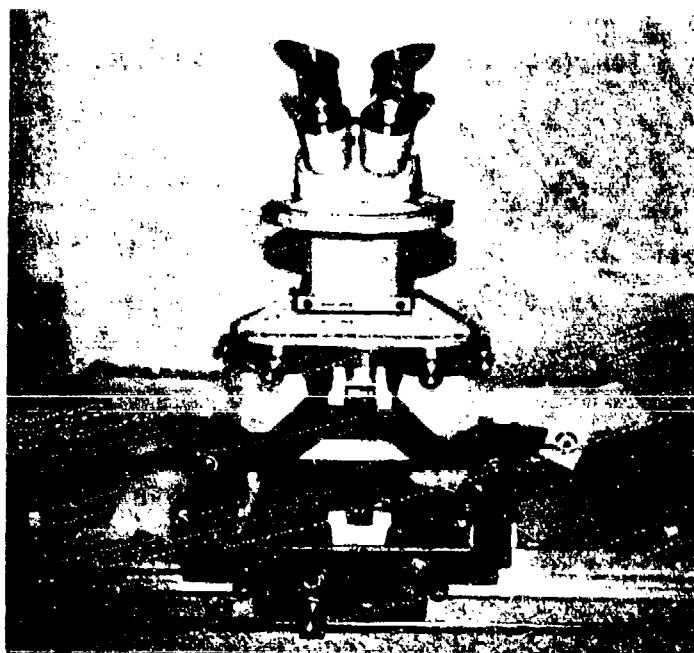


Figure 9. Stereoscopic Microscope.

range of magnification was 7X to 120X. 7X-10X was found to be the optimum magnification range for thin graphite/epoxy specimens.

Analysis based on stereoscopic observations done in this way has one disadvantage--the stereoptical images cannot be simply displayed. One means is to present positive images, properly aligned for the average viewer's interpupillary distance and presume that the viewer has access to a viewing instrument. It has been the author's observation that very few readers satisfy both requirements. Therefore the discussion of results which are provided in the following chapter and which are based on stereoscopic observation will rely on narrative or schematic drawings. However, a typical stereo radiographic image pair is presented as Fig. 10 to illustrate the usefulness of the technique. The lefthand image was made at a specimen elevation of 6 degrees from horizontal and 0 degree tilt angle. The right image was made also at 6 degrees elevation but 15 degrees tilt. The interpupillary distance is fixed at $2 \frac{9}{16}$ in. (65.1 mm), an average value. Viewing can be accomplished by an Abrams folding stereoscope or similar device or by placing a piece of cardboard vertically between the images and viewing at a distance of 8 to 10 in. (203 to 254 mm) so that the cardboard prevents each eye from seeing more than one image. In this example of a damaged $[0,90_2]_s$ graphite/epoxy specimen the dark, horizontal lines are transverse cracks in the 90 degree plies and the vertical lines are longitudinal cracks in the 0 degree plies. The reader should be able to assign

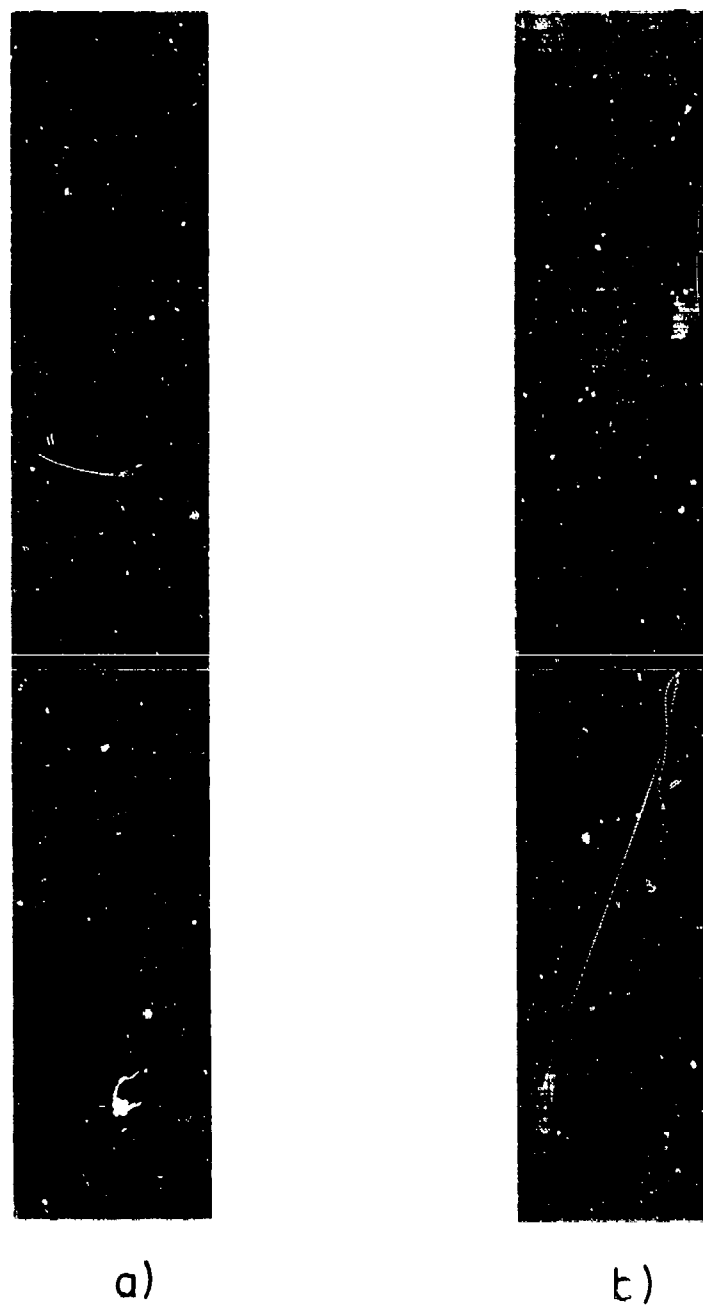


Figure 10. Typical Stereo X-ray Image Pair.

each of the longitudinal cracks to the "near" ply or the "far" ply once stereoptical registration is achieved.

It is commonly assumed that penetration of X-ray enhancing agent into interior damage requires the existence of a continuous path having connectivity with the edge along which the agent is applied. These paths typically involve the off-axis ply cracks. However, it is conceivable that some interior damage might lack the required edge connectivity and hence would be concealed even in enhanced radiographs if this model is correct.

The ability to observe, for the first time, enhanced radiographs both microscopically and stereoptically provided some insight into this question. Although most of the enhanced detail could in fact be associated with a path to the edge, there existed some details, both flaw and damage, which appeared even at high magnification to be completely isolated. These structures were typically small but were nonetheless well-enhanced and easily resolved. Isolated cracks as small as 0.004 in. (0.1 mm) were identifiable.

It does not appear then that edge connectivity is a necessary condition for damage detection. It is likely that at least for T300/5208 graphite/epoxy laminates, zinc iodide can reach interior damage by diffusion through the resin material. Such a phenomenon greatly extends the confidence with which enhanced radiography can be applied to damage detection and characterization.

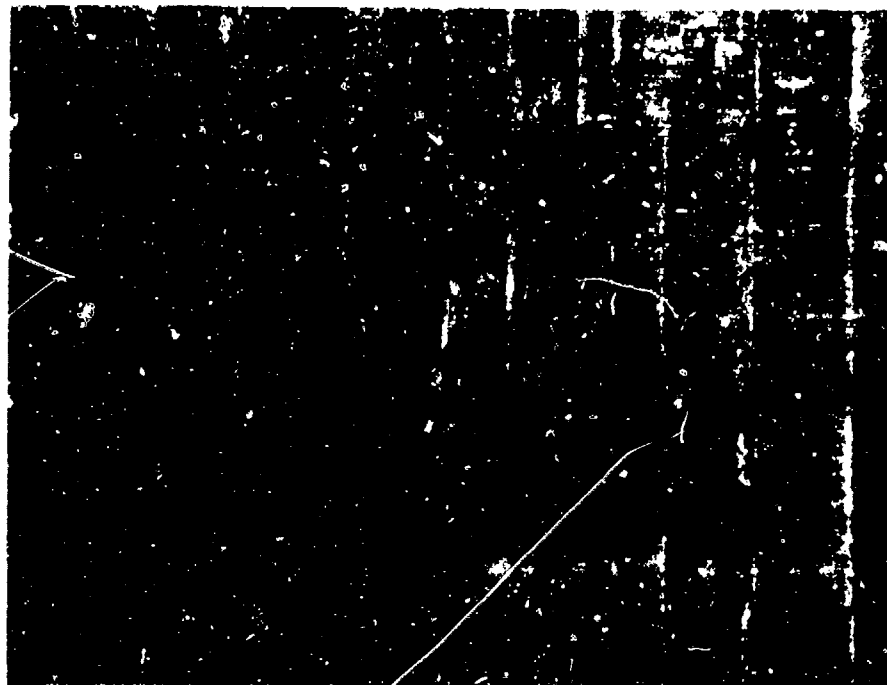
Specimen Deply

None of the available NDE methods provided information about discrete fiber fracture in the interior of graphite/epoxy specimens. Since this information is essential for the complete characterization of damage, a destructive, microscopic technique developed by Freeman [87] was employed. In this technique, the specimen is heated to a temperature sufficient to partially pyrolyze the resin matrix. The interlaminar bond strength is thereby diminished to the extent that the individual plies of the laminate can be separated. For T300/5208 graphite/epoxy material, the required temperature is 785°F (418°C). The time required depends upon the laminate thickness: for 6-ply laminates, 23 minutes was used; for 8-ply laminates, 30 minutes. The heating was accomplished in an electric tube oven in an argon gas environment. The process evolved noxious fumes in quantity which were evacuated from the oven and vented outside. The specimen was removed from the oven after the required time and allowed to cool in air. Using a small knife edge and probe, the individual plies could then be separated. Sufficient resin material remains after pyrolysis to hold the plies together if they are handled carefully. As a precaution, a narrow strip of adhesive tape was applied along an edge of each angle ply to provide reinforcement.

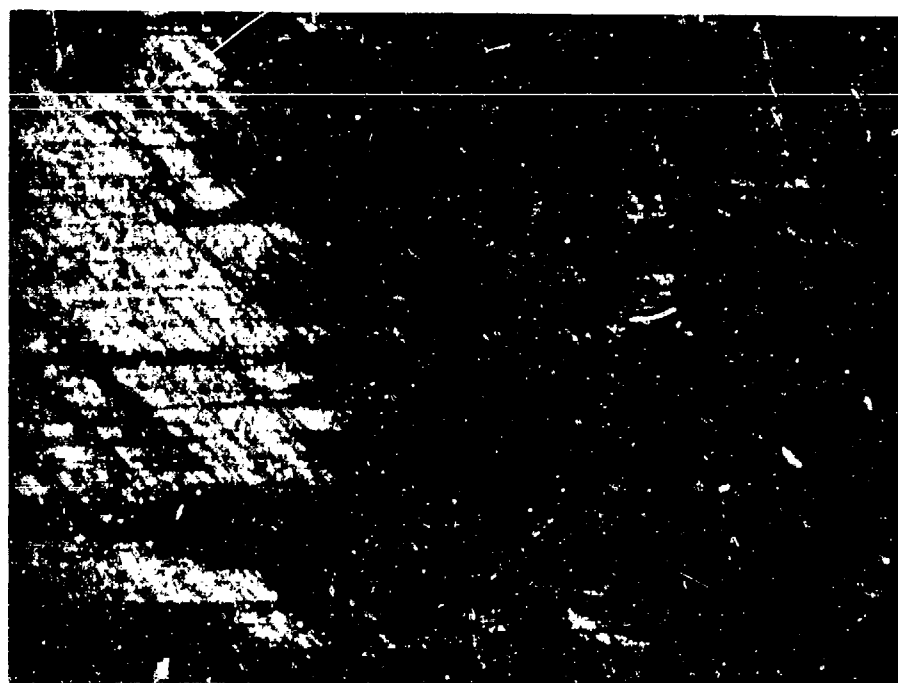
Freeman observed that the introduction of an enhancing agent along the edges of a specimen prior to the deply procedure served to mark regions of damage for visual inspection, much in the manner of X-ray enhancement. The agent which he used and which was also used in

this investigation was gold chloride in a carrier of diethyl ether. A 9.2 weight-percent solution was made and applied to the specimen using the same load fixture and technique described previously for X-ray enhancement. The solution was allowed to remain on each edge for at least 30 minutes. Prior to pyrolysis the specimen was heated to 140°F (60°C) for one hour to drive off the carrier residue and prevent gas bubble formation during the higher temperature process.

The separated plies were examined by two means: light and electron microscopy. For light microscopy, a Bausch and Lomb 3X-30X zoom microscope was used. To derive the maximum benefit from the presence of the enhancing agent, proper illumination was critical. Two types of illumination were required: a fluorescent source directed normal to the fiber direction and an incandescent source approximately parallel to the fiber direction, both angled obliquely to the specimen surface. When the proper combination of illumination is achieved, the gold chloride shines brightly. The effect is particularly pronounced for cracks and delaminations. Figure 11 shows two examples. Figure 11a shows the gold chloride traces on the 0 degree ply of a fatigue damaged $[0,90_2]_S$ laminate. The traces correspond to the locations of transverse cracks in the adjacent plies. Figure 11b is the boundary of a delamination developed in a $[0,90,\pm 45]_S$ laminate during cyclic loading. These boundaries were used to measure the delaminated area of each ply as part of an analysis described in Chapter 4.



a)



b)

Figure 11. Optical Micrographs of a Deplied Lamina Showing
(a) Gold Chloride Traces of Transverse Cracks and
(b) Delamination Boundary.

The second method of observation was by scanning electron microscopy (SEM) which was used principally to study the details of fiber fracture. Coupons measuring approximately 1/4 in. (6 mm) square were cut from various areas of the deplied laminae and mounted with double-sided tape on 1/4 in. diameter specimen stubs. A thin ribbon of silver paint was applied at the perimeter of the coupon to provide an electrical path to the instrument ground in order to minimize electron charging. Operating at 15kV accelerating voltage, it was found that the carbon fibers were sufficiently conductive at magnifications up to 10,000X that it was not necessary to coat the specimens with a layer of gold palladium. Working magnifications to study patterns of fiber breaks was 200-40GX; to study the details of a single fiber fracture, 1000-2000X was required. At 200X magnification, the gold chloride trace was not as evident as it was in the light microscope inasmuch as the apparent interparticle spacing was much larger. However, once the particles had been identified as gold chloride by an energy dispersive X-ray analysis, the trace of these particles could be identified readily at the lower working magnifications.

Sectioning Studies

As part of the examination of particular damage conditions, several sectioning studies were undertaken. The principal sectioning work was associated with the investigation of the nucleation and growth of longitudinal cracking. Two types of sections were used:

one parallel to the longitudinal crack and one normal to the crack. For the normal sections, the cutting and polishing procedures were identical to that used for specimens cut from plates. Observation was by binocular microscope, metallograph, and scanning electron microscope. For the parallel sections, coarse polishing with wetted 400 grit silicon carbide abrasive paper was used to remove material to within 1/8 in. (3 mm) of the longitudinal crack. Polishing was continued with 600 grit abrasive paper until the delamination associated with longitudinal cracks intersected the section surface. This stage is shown schematically in Fig. 12. At that point a splinter of material containing one surface of the longitudinal crack could be removed. The surface was then sputter-coated with gold palladium for SEM examination.

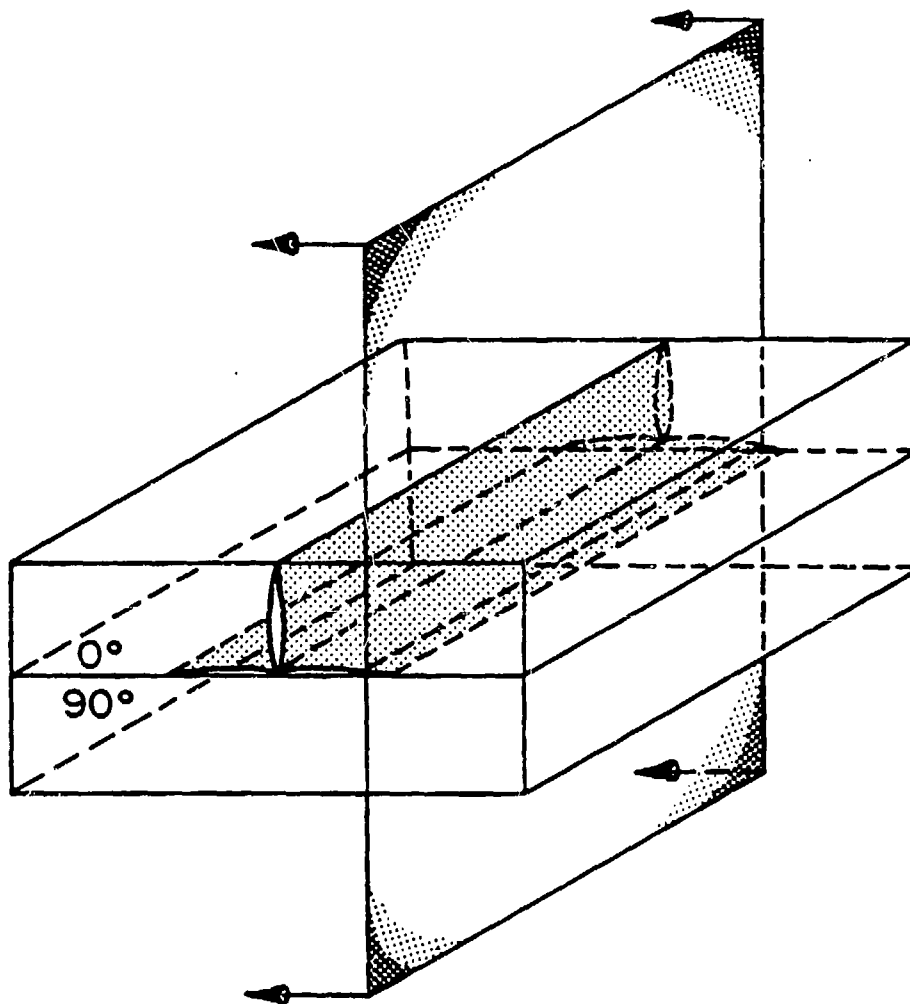


Figure 12. Longitudinal Crack Sectioning Schematic.

IV. RESULTS AND DISCUSSION

One of the challenges of reporting experimental observations of fatigue damage is to provide a rational structure within which the discrete modes can be set and by which a philosophy of fatigue failure can be articulated. It is the purpose of this chapter, and of this investigation, to attempt to accomplish the former and in doing so to assist the latter.

It is first necessary to define what shall be considered fatigue damage. For the purposes of the analysis to be presented here, fatigue damage is that damage which develops progressively as a result of cyclic loading. The damage modes involved are not necessarily unique to cyclic loading, for matrix cracking, delamination, fiber fracture, and other modes of damage also occur in quasi-static loading. What distinguishes the two is the way in which this damage is integrated into a state unique and characteristic of fatigue. For those who would suggest that the damage events are the same from incipency to failure and that fatigue failure is simply static failure delayed, Figure 13 is offered into evidence. The three photographs represent three specimens of graphite/epoxy $[0,90_2]_s$ laminates which failed: a) in quasi-static tension; b) after 2,500 cycles of tension-tension cyclic loading; and c) after 70,000 cycles of tension-tension cyclic loading at the same amplitude. Clearly something is happening to the material to progressively degrade its integrity over an increasingly large region. It is this damage development which shall be of interest here.

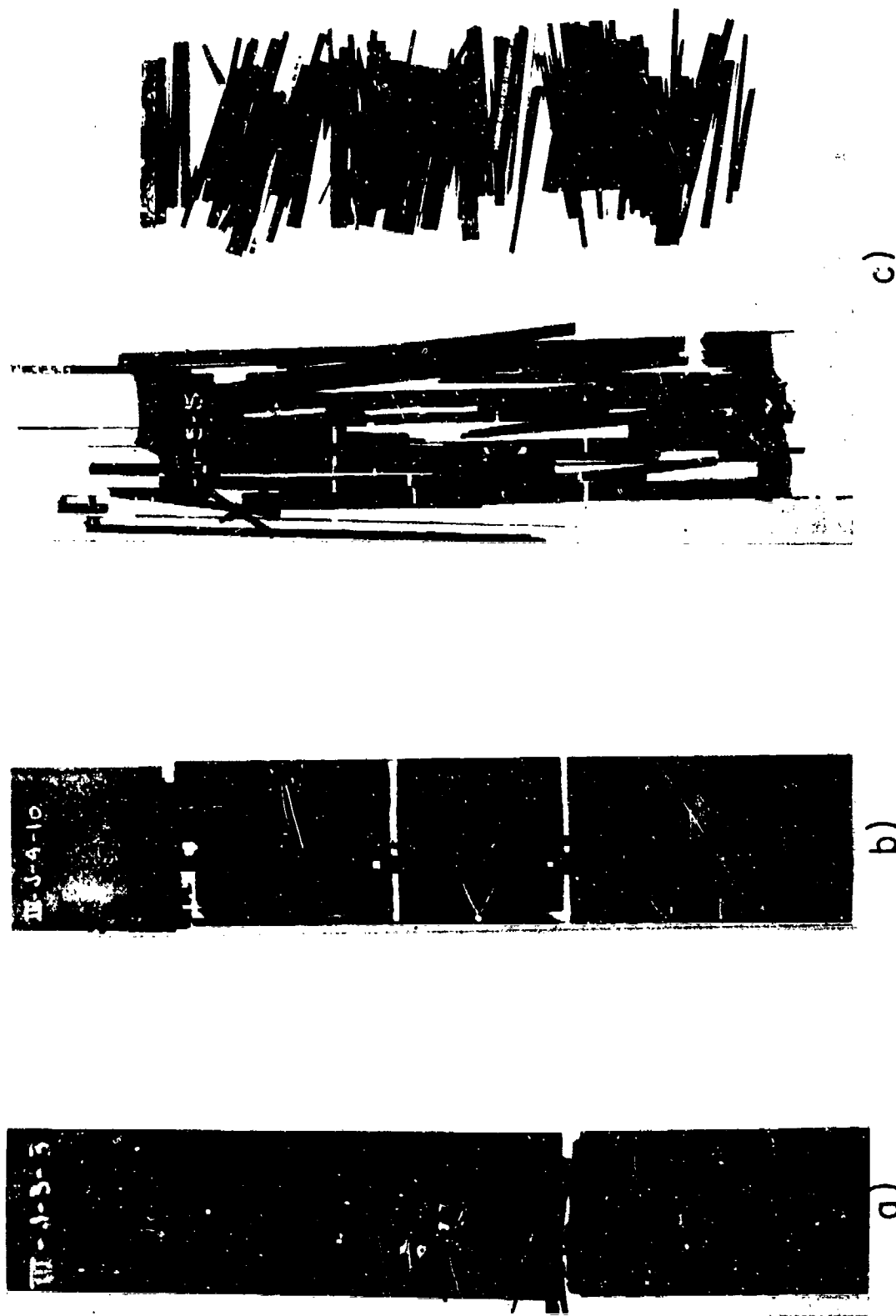


Figure 13. Comparison of Failure Modes in a $[0,90_2]_s$ Laminate.

Extensive experimental and analytical treatments of the characteristic damage state which develops in composite materials have established that it develops independently of load history [59,60]. This shall be taken as the context for defining advanced damage development-damage which develops in cyclic loading subsequent to the development of the characteristic damage state.

The approach to the discussion of results in this chapter will, therefore, be the following: (i) to establish for each laminate type the characteristic damage state to serve as a reference in describing advanced damage; (ii) to identify and define advanced damage in each laminate type; (iii) to establish the damage mode, size and location in terms of the local or global stress state. The framework for the discussion of damage in each laminate type will be its stiffness reduction behavior in fatigue. An early observation was that with each laminate type there was associated a stiffness-versus-cycles relationship which was repeatable and characteristic of the laminate type and that although the relations differed markedly among the laminate types, each was distinguished by three stages: Stage I, a rapid, initial decrease in stiffness; Stage II, a larger, intermediate period of approximately linear stiffness reduction; and Stage III, a final rapid stiffness decrease ending in fracture.

[0,90₂]_s Laminate Type

Overview

The maximum cyclic stress amplitude for all tests was 0.70 S_{ult} . Figure 14 shows the stiffness reduction curve for a typical [0,90₂]_s specimen. The shape of the curve for short life and long life tests are similar and varies little in form from specimen to specimen. Stages I, II, and III are marked on the figure. The association of primary and secondary damage modes can perhaps best begin with the results of a stop and go test. Figure 15 shows a series of edge replicas taken at various points during the fatigue life of one specimen. Figure 15(a) shows the edge condition at the end of one cycle. Thin horizontal lines extending across the width are transverse cracks in the 90 degree plies. Figure 15(b) was made at the end of 1400 cycles and a 1 percent stiffness reduction. The beginnings of several delaminations in the 0/90 degree interfaces at several of the transverse crack tips can be seen. Figure 15(c) was made at the end of 22,000 cycles with a 3 percent stiffness reduction. The delamination at the right surface of the specimen has become complete and has caused separation. The width dimension of this delamination is quite small (less than the specimen thickness). The tensile interlaminar normal stress, σ_z , at the edge, and a tensile stress, σ_y , in the 0 degree plies which promotes longitudinal crack growth in those plies frequently combine to produce edge delaminations in the [0,90₂]_s laminate type.

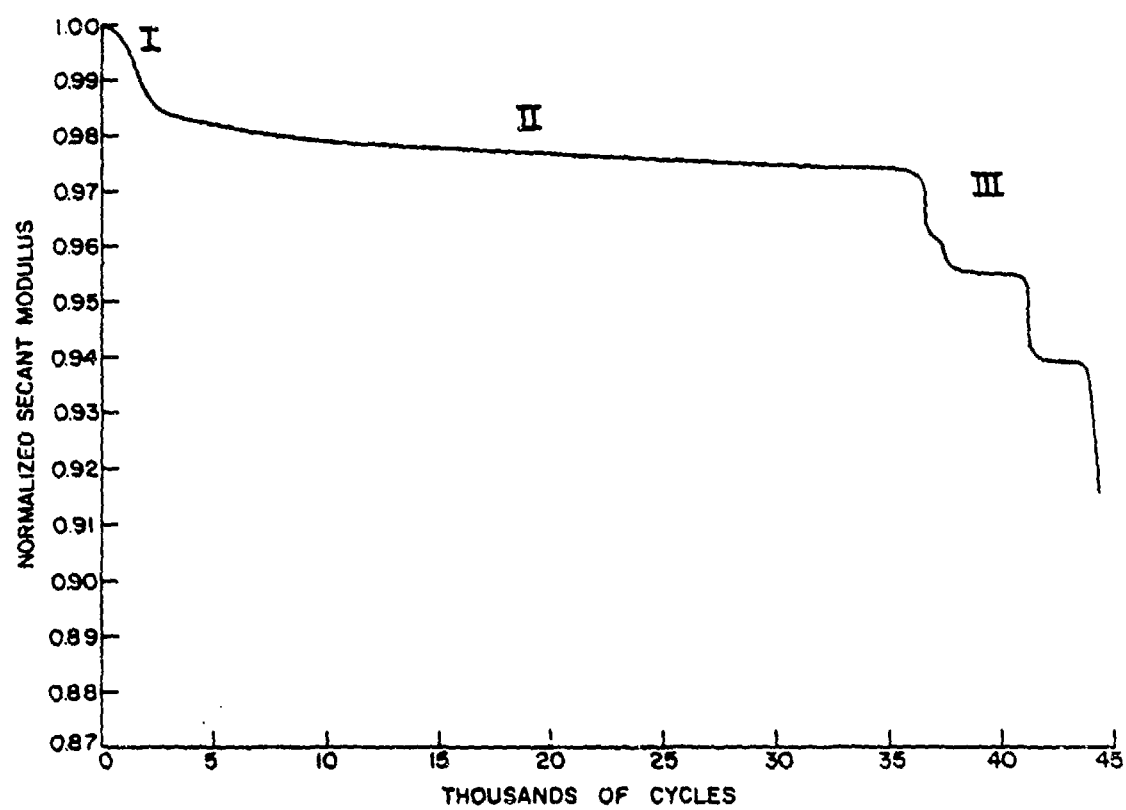


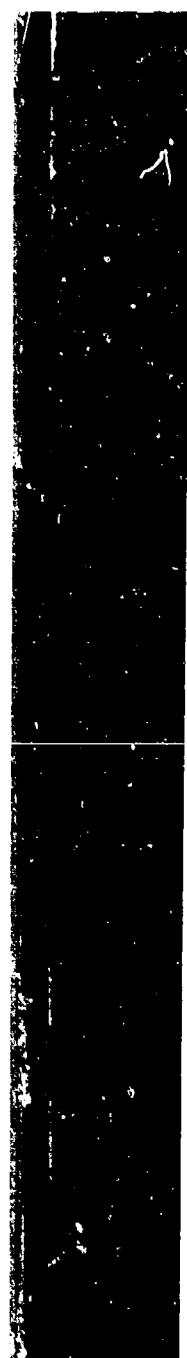
Figure 14. Typical Stiffness Reduction Curve for a [0,90₂]₅ Laminate.



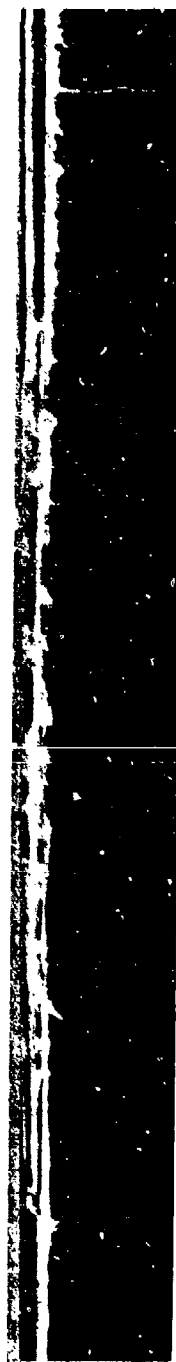
Figure 15. Edge Replicas from a Progressively Fatigue-Damaged $[0,90_2]_s$ Laminate (Left Side).

Comparing this figure to Figure 15(b), it is notable that the number of cracks has not increased. In fact, at this point the specimen has achieved the characteristic damage state crack spacing of 0.026 in. (0.67 mm) predicted by the one-dimensional shear lag analysis of Reifsnider [88], and no additional cracks would be expected to form. Figure 16 shows the opposite edge of the same specimen at higher cycles. Figure 16(a) corresponds to 181,000 cycles, 5.3 percent stiffness reduction. Delaminations are seen to extend from most transverse crack tips and on the left-hand side are seen to have joined together. At 258,000 cycles, 7.7 percent stiffness reduction (Fig. 16(b)), damage is severe but appears to have achieved a saturation condition along the edge. The specimen failed at 287,000 cycles, with a 10.4 percent stiffness reduction.

Figure 17 shows a stop and go series of X-ray radiographs for another $[0,90_2]_S$ specimen. X-rays were penetrant-enhanced as described in Chapter III. Figure 17(a) shows the virgin specimen as fabricated. Some porosity is visible at the specimen edges. The dark dot at the center of one edge is a silver paint fiducial mark used for stereoptical alignment. Figure 17(b) is the same specimen after 26,000 cycles, 3 percent stiffness reduction. The dark, horizontal lines reaching from edge to edge are transverse cracks in the 90 degree plies. Their edge-to-edge continuity is evidence that crack development observed at the edge is also representative of the interior condition. Measurement of crack spacing in the radiograph confirms the CDS prediction.



a)



b)

Figure 16. Edge Replicas from a Progressively Fatigue-Damaged $[0,90_2]_S$ Laminate (Right Side).

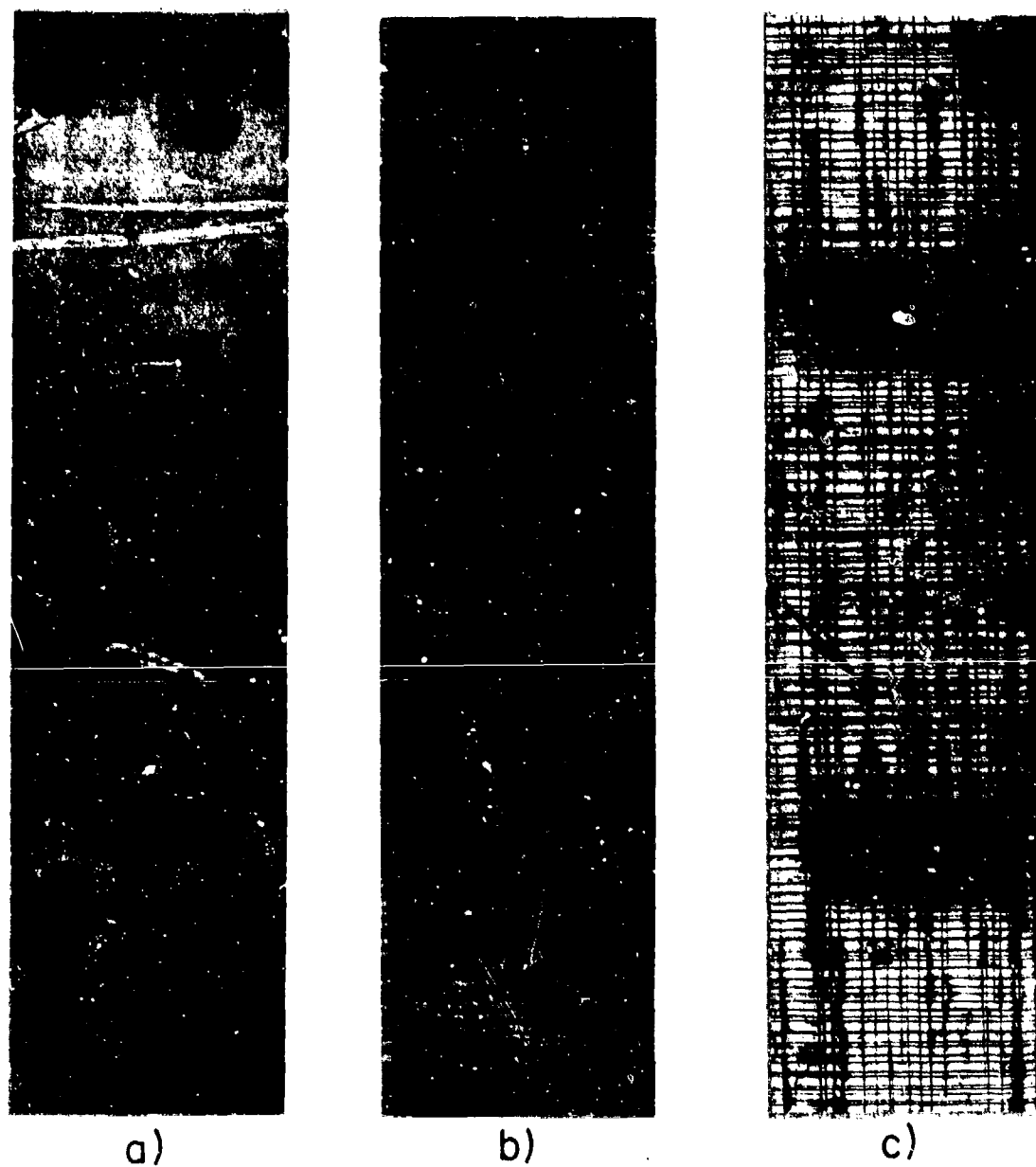


Figure 17. X-ray Radiographs of a Progressively Fatigue-Damaged $[0,90_2]_s$ Laminate.

The long, vertical lines are longitudinal cracks in one or the other of the 0 degree plies. These cracks are not of equal length, some being considerably larger than others. The stereoptical technique makes assignment of these cracks to the plies in which they lie a simple matter. The two dark, rectangular shapes in this radiograph and the one adjacent to it are images of the extensometer mounting tabs. Figure 17(c) shows the specimen at 71,000 cycles with a 7 percent stiffness reduction. The average spacing between adjacent cracks has not changed from the previous radiograph; both, in fact, correspond to the predicted CDS spacing. A notable feature of the third radiograph is the increased density and length of the longitudinal cracks. Some extend nearly the full length of the specimen and growth of individual cracks can be clearly seen by comparison with the previous radiograph. When the radiographs are viewed stereoptically, the number of longitudinal cracks is seen to be approximately evenly divided between the 0 degree plies.

Less obvious detail also appears in Figure 17(c). Associated with many of the longitudinal cracks are small, halo-like structures. An arrow points to one in the radiograph. Each of these structures appears to be bisected by the longitudinal crack and upon stereoptical examination, each is seen to reside at a 0/90 degree interface. By comparing these details with enhanced radiographs of specimens containing edge delaminations, it was determined that these structures are interior delaminations.

Also of interest in Figure 17(c) are the delaminations at each edge. They are also observed in edge replicas. However, they are confined in the $[0,90_2]_3$ laminates to a boundary layer along the edge having a width approximately equal to the laminate thickness.

The specimen for which this series of radiographs was made failed at 75,000 cycles with no additional stiffness reduction. With this initial characterization to provide an overview of damage development in the $[0,90_2]_3$ laminate type, the details of the damage and an association of the damage with the regions of stiffness reduction in which the damage modes are predominant will be considered next.

Stage I

Figure 18 shows an edge replica of a $[0,90_2]_3$ specimen at the end of 50,000 cycles with a measured stiffness reduction of 2.4 percent corresponding to approximately the end of Stage I in the characteristic curve. The transverse crack spacing corresponds to the characteristic damage state. Some incipient delamination growth is observed. Figure 19 is the Stage I portion of the stiffness reduction curve for the same specimen. Also included is a plot of crack density taken from replicas made at intermediate stages. Approximately one-half of the transverse cracks which ultimately form in these laminates do so in the first cycle for the load levels used. As noted in Chapter 3, the procedure used for starting each fatigue test inevitably resulted in the loss of initial stiffness reduction information. By measuring static stiffness changes at the beginning of a number of tests, it was found that the average stiffness deficit

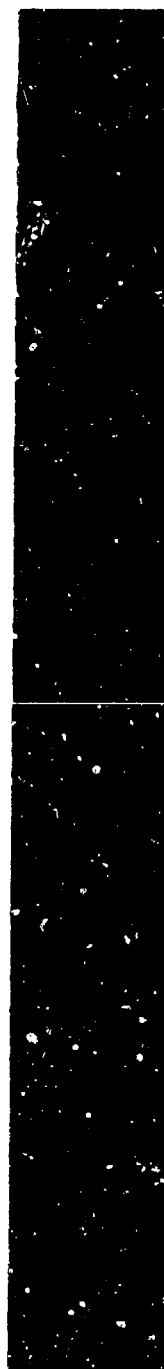


Figure 18. Edge Replica from a $[0,90_2]_s$ Laminate at Stage I.

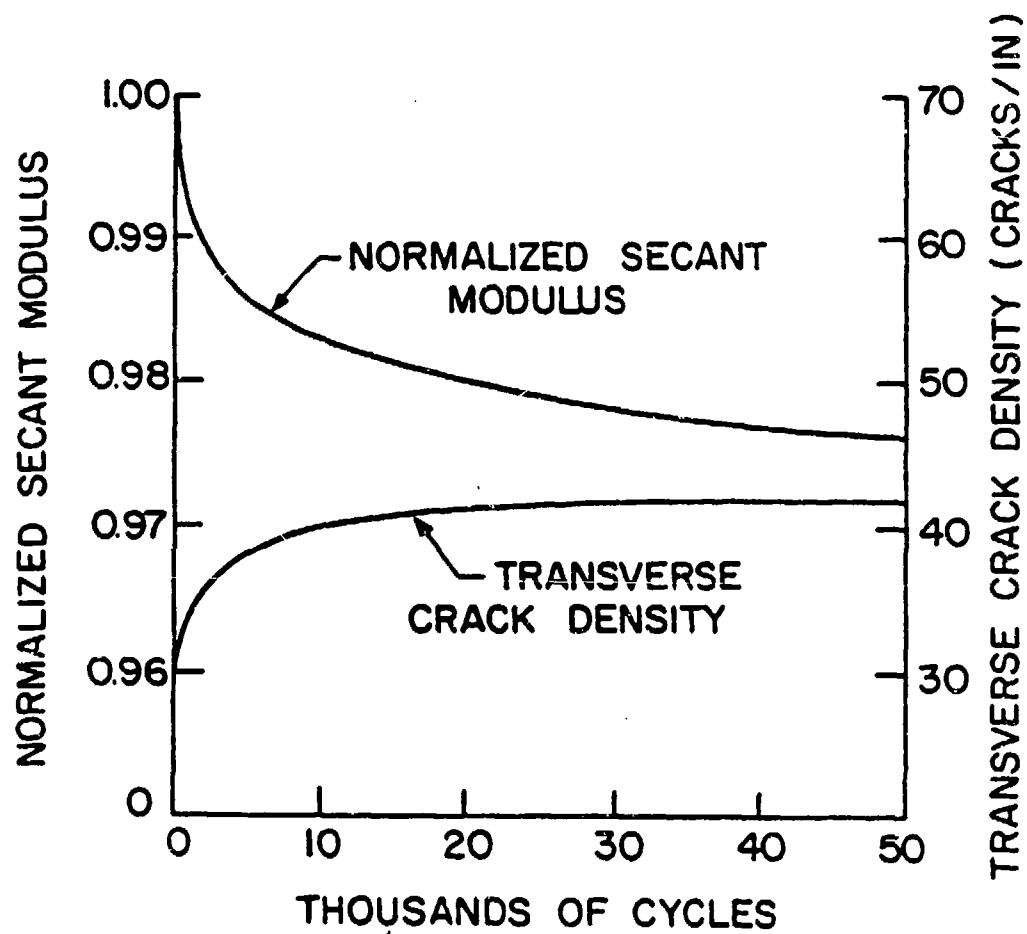


Figure 19. Stiffness Reduction and Crack Development for a $[0,90]_s$ Laminate at Stage I.

was 4.5 percent. Thus the total stiffness reduction in this specimen was approximately 6.9 percent.

Can this stiffness reduction be explained in terms of the formation of transverse cracks alone? The answer is provided by the classical laminated plate theory. The longitudinal stiffness of an undamaged $[0,90_2]_s$ laminate is calculated to be 7.88×10^3 ksi (5.43×10^4 MPa) based on the following nominal lamina properties of T300/5208 graphite/epoxy material:

$$E_1 = 2.055 \times 10^4 \text{ ksi } (14.2 \times 10^4 \text{ MPa})$$

$$E_2 = 1.48 \times 10^3 \text{ ksi } (10.2 \times 10^3 \text{ MPa})$$

$$\nu_{12} = 0.305$$

$$G_{12} = 8.71 \times 10^2 \text{ ksi } (6.0 \times 10^3 \text{ MPa})$$

If, for saturation cracking, it is assumed that the longitudinal stiffness, E_2 , and the shear modulus G_{12} are reduced to zero and if these discounted properties are used in the laminated plate theory, then the predicted laminate stiffness becomes 6.89×10^3 ksi (4.75×10^4 MPa). The laminate stiffness reduction due only to saturation cracking of the 90 degree plies is thus 12.6 percent. This is more than sufficient to account for the measured stiffness reduction of 6.9 percent. The fact that it is substantially more can be attributed to the fact that transverse cracking reduces the load-carrying capacity of those plies only in a local region adjacent to the cracks. The material between adjacent cracks outside of these relaxed zones is capable of carrying some load and hence contributing to the

laminate stiffness. For example, if saturation cracking is assumed to reduce the longitudinal stiffness of the 90 degree plies to one-half of the undegraded value, then the laminate stiffness becomes 7.38×10^3 ksi (5.09×10^4 MPa) and the calculated stiffness reduction is 6.3 percent. Inasmuch as the measured stiffness reduction is acquired over a two inch gage length and is certainly "global" when compared to the spacing of the approximately 80 cracks which are included therein, the total discount scheme can be expected to provide an upper bound on the actual stiffness reduction.

Other damage at this stage is relatively minor. Some small delaminations confined to a boundary layer along the edge are observed. These delaminations actually appear to mark the beginning of Stage II damage.

Stage II

Figure 20 is an edge replica made of another specimen at the end of 73,000 cycles with a 4 percent stiffness reduction, corresponding to approximately the end of Stage II in the characteristic curve. A delamination running the full length of one of the 0/90 degree interfaces is observed as well as an incipient delamination at the other interface. Such delaminations are frequently observed to be connected to transverse cracks. Upon close inspection, it appears that the transverse cracks make a 90 degree "turn" at the interface. Such a phenomenon is not unexpected for a crack confronted by the very steep gradient of stiffness and strength presented by the fibers of the 0 degree plies. Although analysis of the complex stress state about the

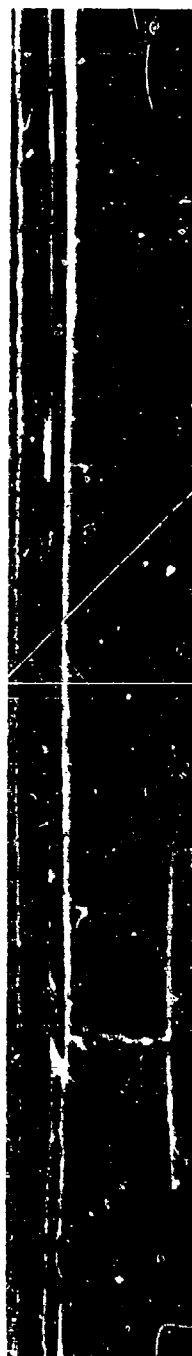


Figure 20. Edge Replica from a $[0,90_2]_s$ Laminate at Stage II.

crack tip in a nonuniform medium is outside the scope of this work, it has been shown [93] that a crack growing into a positive strength gradient will divert laterally. In a $[0,90_2]_s$ laminate, this diverted path takes the crack through a resin-rich zone at the 0/90 degree interface, a region notably low in strength. The growth of the delamination along the edge is aided by a tensile interlaminar normal stress, σ_z (see Fig. 1). However, sectioning studies show that the growth of these delaminations across the width is limited to a distance approximately equal to the laminate thickness. Figure 21 shows radiographs of sections cut from the edges of a $[0,90_2]_s$ laminate after 400,000 cycles. The orientation is the same as that used for replicas, with horizontal, dark lines being transverse cracks and vertical lines being delaminations in the 0/90 degree interfaces. Figure 21(a) shows a thin section taken from the edge of the specimen and having a depth dimension (normal to the photograph) equal to the laminate thickness, approximately 0.034 in. (0.86 mm). Figure 21(b) is a section of the same dimension removed from the same side of the specimen. Together they show successive views of first the original and then an exposed edge. The sectioning arrangement is shown schematically in Fig. 21(c).

Examination of the sections shows that the delaminations are clearly associated with cracks and are often single-branched. Comparison between Figs. 21(a) and 21(b) shows that although some evidence of delamination exists at the specimen interior, the extent is diminished markedly over a quite small distance.

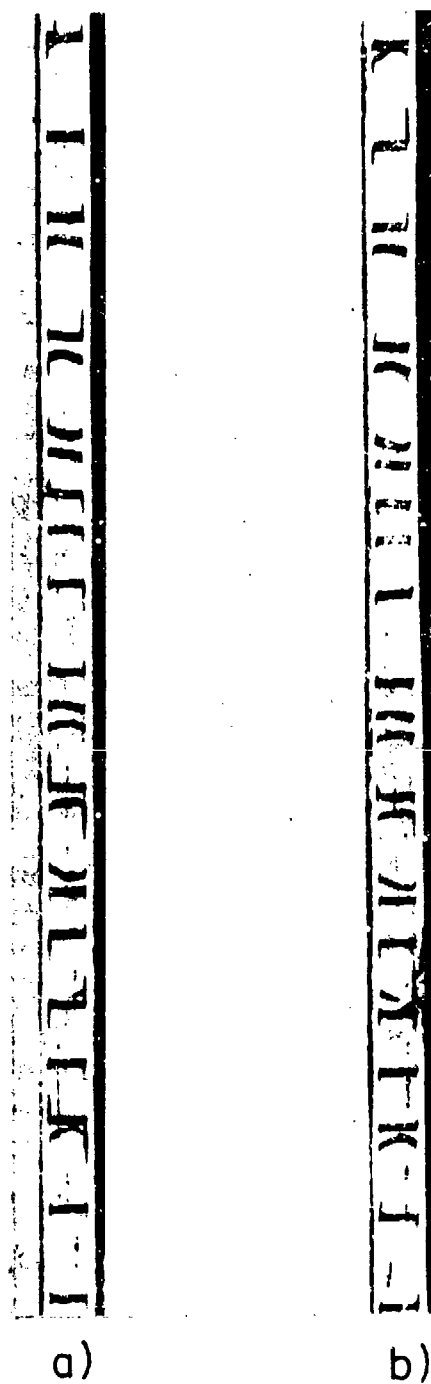
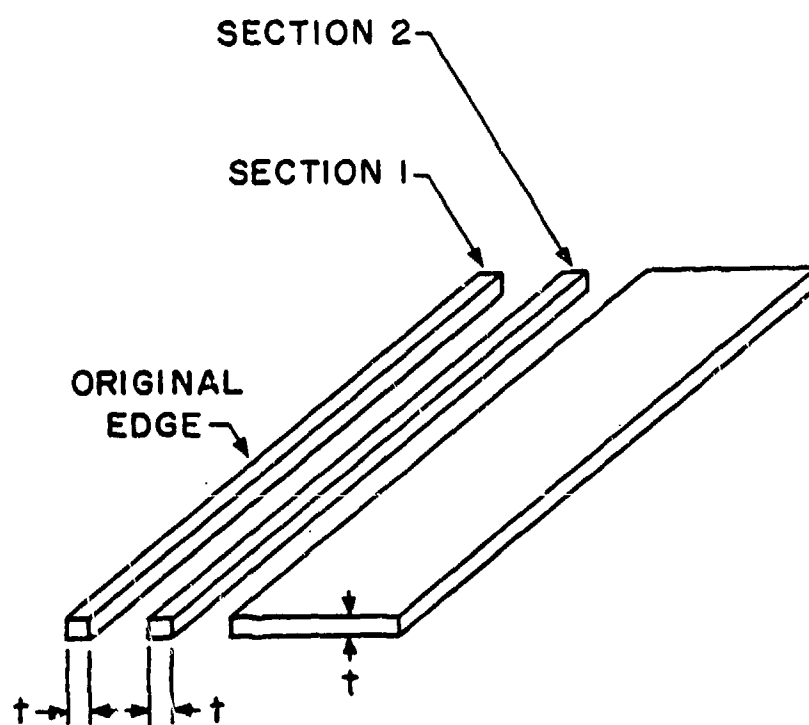


Figure 21. X-ray Radiographs of Sections Removed from a $[0,90_2]_s$ Laminate.



c)

Figure 21. Sectioning Schematic (Cont'd.).

The observations regarding edge delaminations in this type of laminate suggest that they are nucleated by the turning of transverse cracks for which the preferred self-similar path is thwarted by a steep material property gradient existing near the 0/90 degree interface and that their growth along the interface is assisted by the presence of a tensile interlaminar normal stress. The fact that both the interlaminar stress and the observed edge delaminations are confined to narrow boundary layers of approximately the same width dimension suggests that the role of transverse cracks in the formation of these delaminations is that of an aid but not a primary driver.

Figure 22 is a radiograph of a specimen at the end of Stage II. Aside from the transverse cracks, the dominant structures are longitudinal cracks. These cracks are present in Stage I but are few in number and small in length. During Stage II damage development both measures increase. They exhibit a fatigue character on a macroscopic scale, growing slowly and stably with increasing cycles. As will be seen from the discussion of Stage III damage development, this growth is not complete at the end of Stage II. But because the formation of transverse cracks is complete at the beginning of Stage II and other damage modes are only moderately active at this stage, longitudinal cracking predominates.

The key to understanding the formation and growth of longitudinal cracks in 0 degree plies in tensile loading lies in the stress state in that ply. For a uniaxial load in the x-direction, the transverse stress, σ_y , in the y-direction is strongly tensile, owing to the

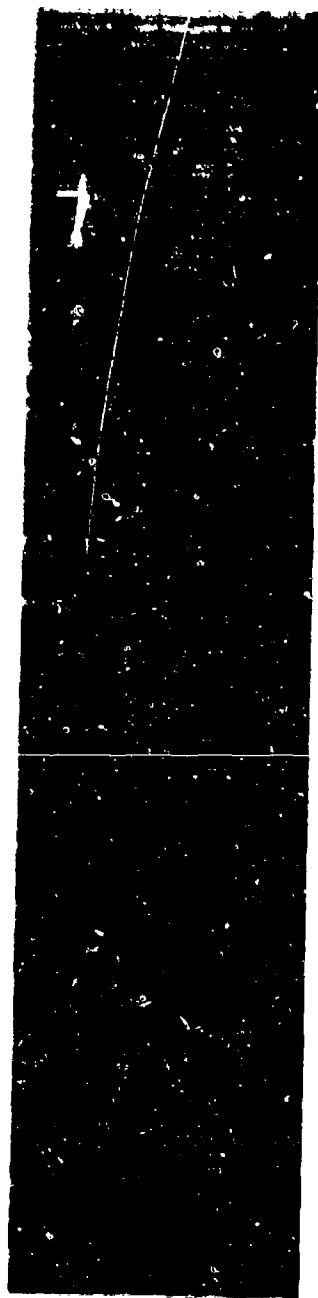


Figure 22. X-ray Radiograph of a $[0,90_2]_S$ Laminate at Stage II.

magnitude of the Poisson mismatch between the 0 degree ply and the adjacent 90 degree plies. The transverse strength of the 0 degree plies, however, is low. In fact, at the maximum operating stress levels used for this laminate type, the σ_y stress is approximately equal to the static transverse strength of the 0 degree ply. However, the interlaminar constraint condition prevents complete cracking on the first cycle.

The growth of longitudinal cracks is gradual with continued cyclic loading. To examine the fatigue nature of this growth, several damaged specimens judged to be in a Stage II or Stage III condition were sectioned to expose the longitudinal crack surface. Figure 23 is an SEM photograph of one such surface. The fibers are oriented horizontally in the photograph and are sheathed in resin. Although polymers do not typically exhibit the striations which characterize fatigue fracture surfaces in metals, the character of this surface was seen to be distinctly different from the appearance of a transverse crack surface, shown in Fig. 24. In this material, transverse cracks grow nearly instantaneously and produce a brittle, glass-like quasi-cleavage fracture surface having characteristic, overlapping structures, sometimes called hackles [55]. Comparing Figs. 23 and 24, the sharp structures seen in the transverse crack are present but smoothed in the longitudinal crack, suggesting a wearing action in the latter case. Such wear might be expected in a cyclic load from the clapping or rubbing together of the crack surfaces after the crack has formed and started to grow.

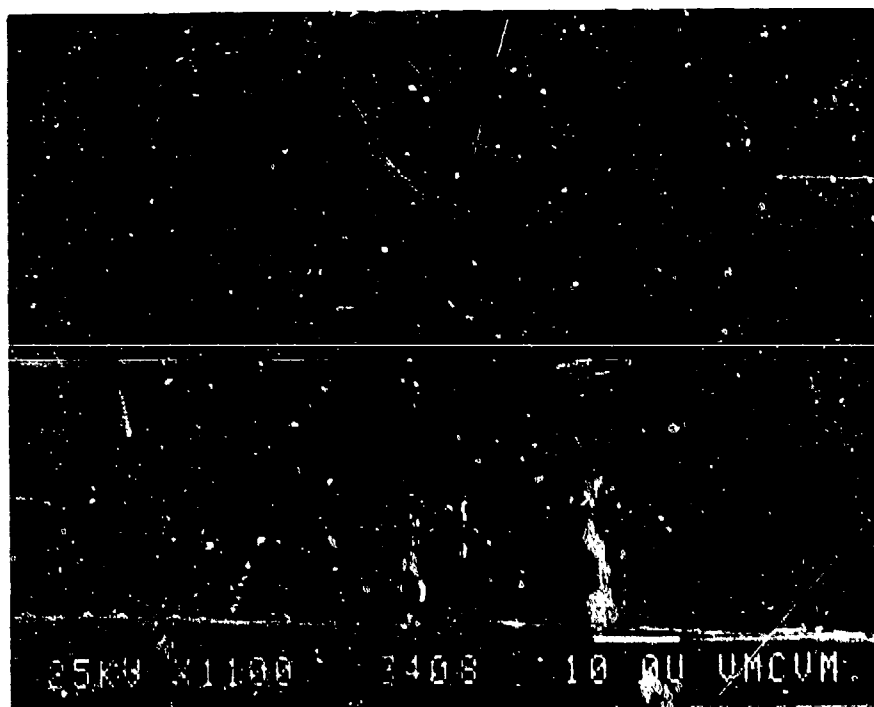


Figure 23. Longitudinal Crack Surface.

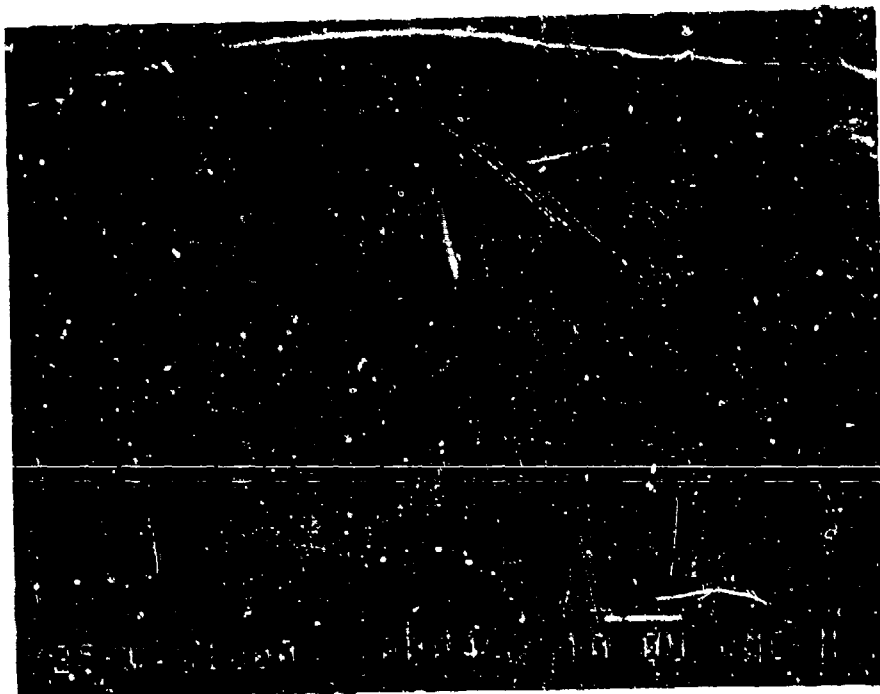


Figure 24. Transverse Crack Surface.

Besides the fatigue aspects of longitudinal crack growth which will be discussed further in the section describing Stage III damage development, an interesting and unexpected phenomenon was observed. Figure 25 is an enlargement of a portion of Fig. 22. Of interest are the dark, halo-like structures associated with some of the longitudinal cracks. Under stereoptical inspection, each of these structures is seen to be at one of the 0/90 degree interfaces and, by comparison with similar radiographic images at the edges of other laminate types, appears to be a delamination. To investigate this suspicion, sections of fatigue-damaged specimens in which longitudinal cracks were identified were prepared such that the plane of the cut was normal to the 0 degree fiber direction and placed so as to be adjacent to, but not intersecting, the longitudinal crack. The section surface was then abraded, polished, and inspected microscopically in a repeated cycle until the end of a longitudinal crack was encountered. Figure 26 is an SEM photograph of the initial encounter of a longitudinal crack in a 0 degree ply. A narrow, irregular crack through the full ply thickness is observed. At the interface, the crack turns downward and travels along the resin-rich zone at the interface. (This phenomenon has been predicted analytically by Nair and Reifsnider [93].) A similar crack turning is frequently observed when cracks in 90 degree plies meet this same interface. Followed to its terminus, this interlaminar crack was seen to extend a distance greater than four times the 0 degree ply thickness.



Figure 25. Detail of X-ray Radiograph of a $[0,90_2]_s$ Laminate at Stage II.

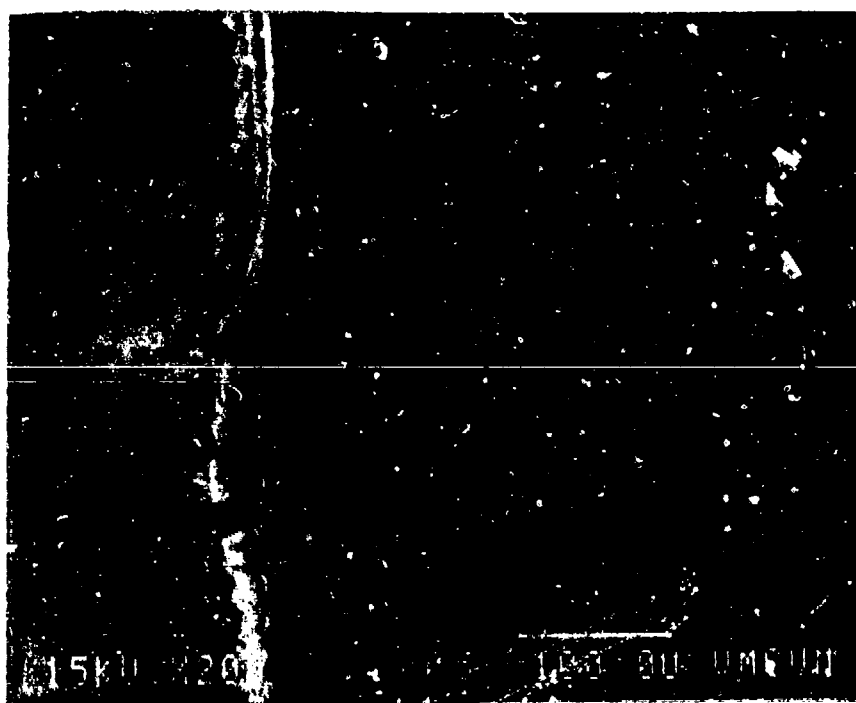


Figure 26. Transverse Section of a Longitudinal Crack (Near Tip).

Figure 27 is an SEM photograph of the same crack at a parallel section approximately 0.010 in. (0.25 mm) from that of Fig. 26. The longitudinal crack is seen to be more widely open and a second branch of the interlaminar crack is evident. The interlaminar crack is also wider. Continued section studies of this and other specimens indicate that the opening dimensions of longitudinal cracks and associated delaminations can be significant when compared to the ply thickness. Successive parallel sections provide a picture of the delamination as a domelike structure with the longitudinal crack as its apex.

In none of the sections examined was a longitudinal crack observed which did not extend completely through the 0 degree ply. This was true of both incipient and well-developed longitudinal cracks. Moreover, no instance was observed when the longitudinal crack was not associated with an interlaminar crack. There appears then to be a rapid or instantaneous nucleation step in longitudinal crack development which involves simultaneously the nucleation of a delamination.

Although the growth of longitudinal cracks can be attributed to the significant transverse stresses which act on the 0 degree plies of this laminate type, the nucleation process may be related to the local stress state about the transverse cracks in the adjacent 90 degree plies. Setting aside for the present the anisotropic, inhomogeneous complexities of the problem and treating the transverse crack as a crack in the infinite, homogeneous isotropic plate of Fig. 28 and assuming plane strain conditions, the stresses in the neighborhood of the crack tip are given by [94]:

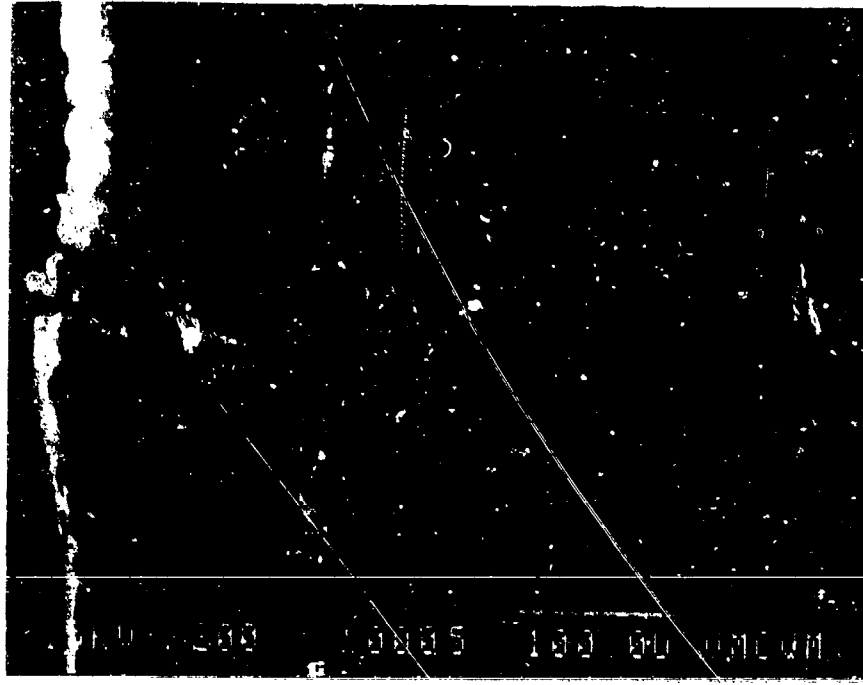


Figure 27. Transverse Section of a Longitudinal Crack (Away from the Tip).

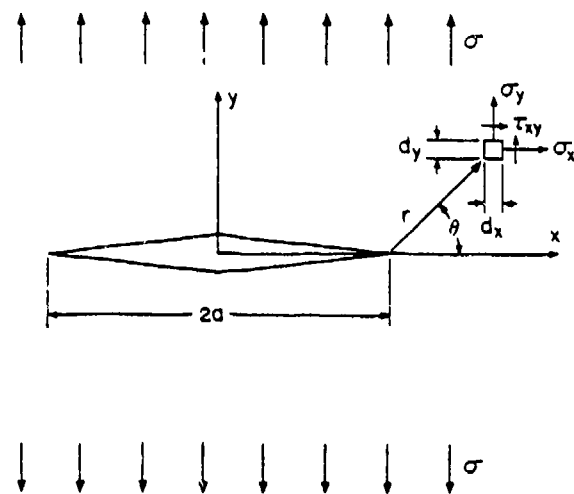


Figure 28. Crack Tip Stresses (from Reference 92).

$$\begin{aligned}
\sigma_x &= \sigma \sqrt{\frac{a}{2r}} \cos \frac{\theta}{2} \left[1 - \sin \frac{\theta}{2} \sin \frac{3\theta}{2} \right] \\
\sigma_y &= \sigma \sqrt{\frac{a}{2r}} \cos \frac{\theta}{2} \left[1 + \sin \frac{\theta}{2} \sin \frac{3\theta}{2} \right] \\
\sigma_z &= \nu(\sigma_x + \sigma_y)
\end{aligned} \tag{1}$$

These equations yield tensile stresses for each of the stress components for all values of θ and r for a tensile applied stress, σ . Nair and Reifsnider [93] have shown by an approximate solution that the stress field about a crack tip in a nonuniform material (spatially variable mechanical properties) is similar in form to that given by equations (1) and that for a positive strength gradient at the crack tip, the stresses are tensile. Such a positive gradient exists at the interfaces of fiber-reinforced composite materials.

Figure 29 shows the implications of the existence of a tensile stress σ_t in the neighborhood of a crack in the 90 degree plies. The material adjacent to the crack tip, in the 0 degree ply, would be subjected to this tensile stress in its lowest strength direction. Hence, the transverse crack can be considered a likely site for the nucleation of longitudinal cracks. Examination of radiographs in which longitudinal cracks appear indicates that the majority of incipient longitudinal cracks do in fact intersect or are adjacent to transverse cracks.

The local stress nucleation concept can be applied to delaminations as well, as Fig. 30 illustrates. Here the local tensile

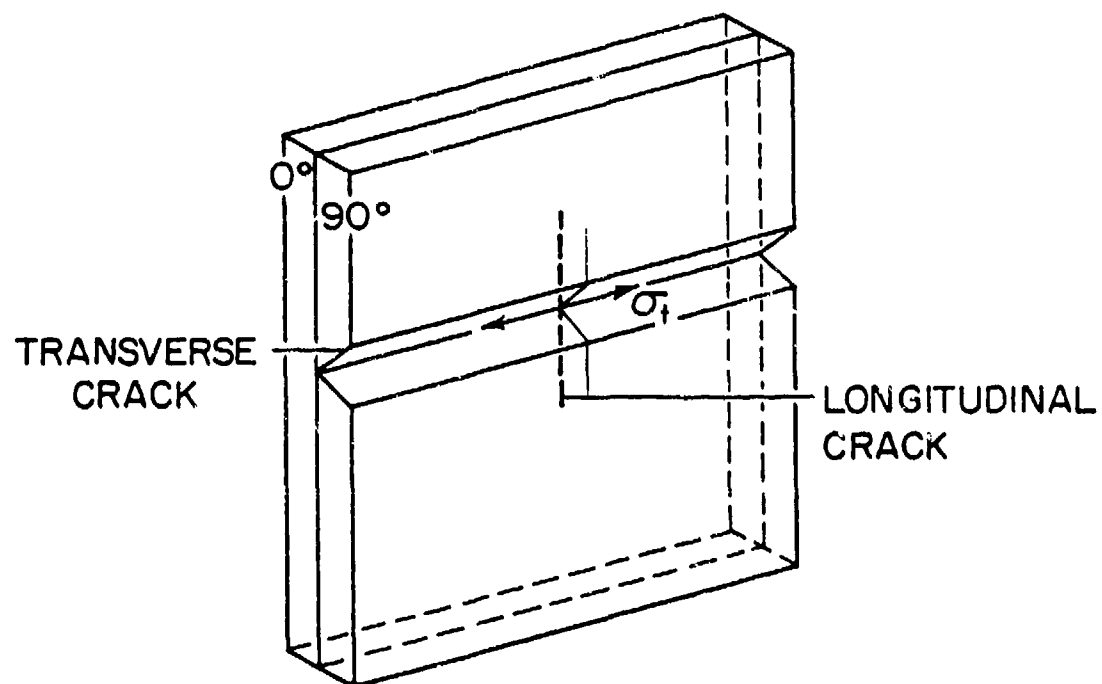


Figure 29. Zero Degree Stresses in the Neighborhood of a Transverse Crack.

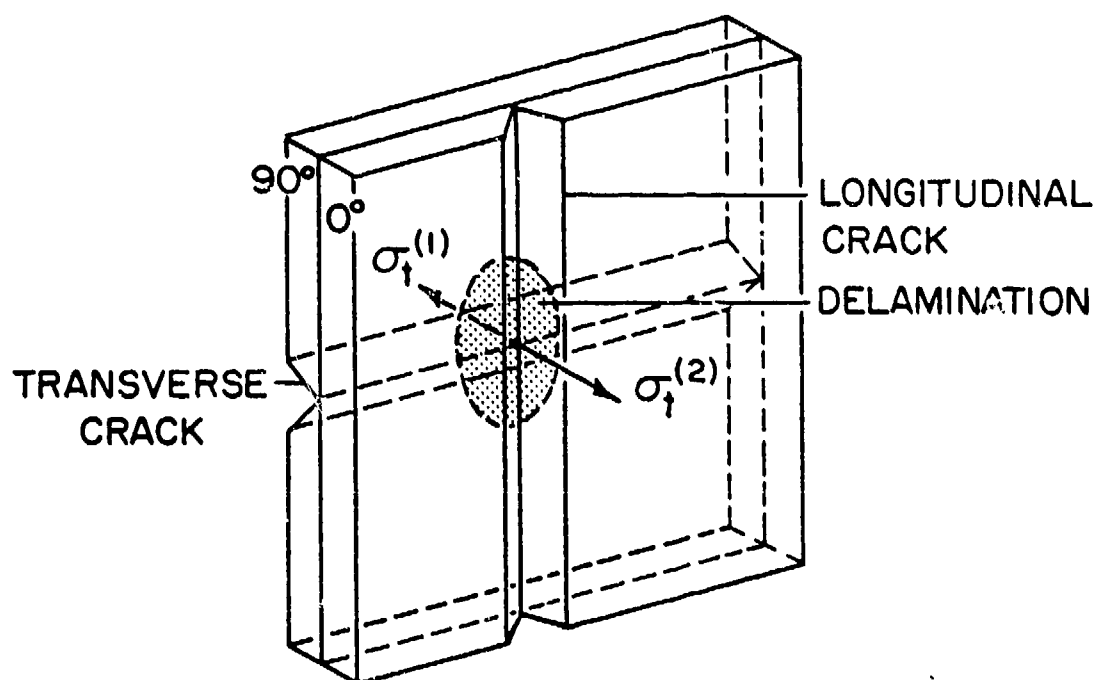


Figure 30. Influence of Longitudinal Crack on Interior Delamination Formation.

stress condition is provided by the longitudinal crack. The tensile nature of the stress in this case produces an out-of-plane tensile stress component, $\sigma_t^{(1)}$, at the interface. In addition, an out-of-plane tensile stress component, $\sigma_t^{(2)}$, is provided by the transverse cracks. At intersections of these cracks, the stresses would be additive and the propensity for the nucleation and growth of delaminations should be highest. This is in fact observed experimentally. The centers of incipient delaminations frequently coincide with crack intersections. These are also the points of maximum delamination opening.

Delaminations created in this way grow in size only moderately during Stage II damage development, apparently by coalescence. However, in the absence of a global driving force, for example interlaminar shear or normal stress components, they remain a local phenomena.

Stage III

Figure 31 is a radiograph of a specimen made at the end of 372,000 cycles of loading with a 5.1 percent stiffness reduction. This stiffness reduction corresponds approximately to Stage III in the characteristic curve. When compared with the Stage II radiograph of Fig. 22, the most notable difference is the increased average length and density of longitudinal cracks. From analysis of radiographs made during stop and go fatigue tests, the spacing shown in Fig. 31 is found to represent a saturation longitudinal crack spacing of approximately 0.063 in. (1.6 mm) corresponding to 16 cracks per in.

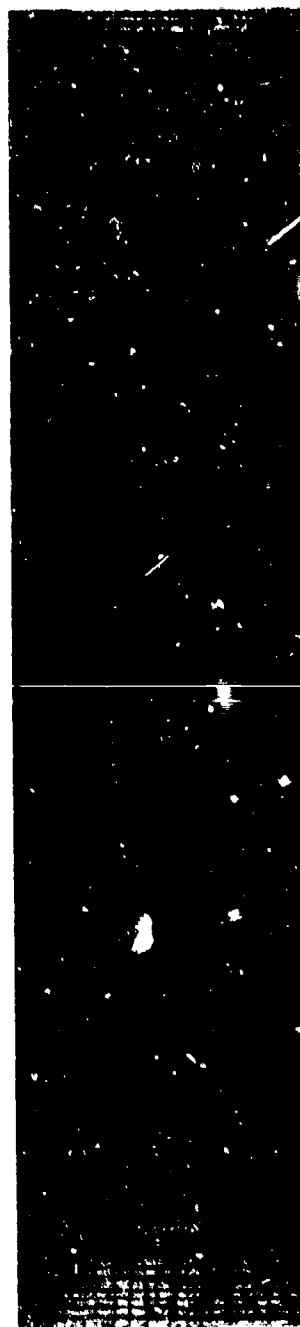


Figure 31. X-ray Radiograph of a $[0,90_2]_s$ Laminate at Stage III.

(0.62 cracks per mm). The spacing was determined by observing and measuring distances between adjacent cracks under the stereoptical microscope. The variation in spacing is similar to that observed for transverse cracks. In fact, the rationale for predicting the existence and measure of such a saturation spacing of longitudinal cracks is identical to that applied to the characteristic damage state of off-axis ply cracking. That is, in order for a crack to be formed between two existing cracks, the stress in the ply must attain a value exceeding the transverse ply strength. However, the reintroduction of stress into the broken ply by shear transfer from neighboring plies requires a minimum distance in order to be complete. This minimum distance controls the saturation spacing of cracks which corresponds to the characteristic damage state for matrix cracking.

Using a modified one-dimensional shear lag analysis, Reifsnider [98] has predicted a longitudinal crack spacing of 0.054 in. (1.4 mm) corresponding to 18.5 cracks per in. (0.72 cracks per mm), which compares favorably with the measured value of 16 cracks per inch.

The longitudinal stiffness reduction attributable to a saturation condition of longitudinal cracks is small: 0.5 percent if total loss of transverse stiffness in the 0 degree plies is presumed in the laminated plate theory; 0.25 percent if a 50 percent discount of transverse stiffness in these plies is presumed.

Microscopic examination of Fig. 31 shows that many short, longitudinal cracks exist at this stage. These are cracks which have been nucleated by the local mechanisms described in the previous section

and which continue to operate in Stage III but which cannot grow in the relaxed global stress field created by the growth of their predecessors.

The growth of longitudinal cracks and the coalescence of delaminations associated with them combine to produce a final damage mode characteristic of State III development--longitudinal splitting. The condition is shown schematically in Fig. 32. When delaminations coalesce between adjacent longitudinal cracks, a volume of fibers in the 0 degree ply is isolated from the remainder of the material. Over the length of the joined delaminations, fibers in this volume have no load-sharing bond with either the adjacent 0 degree fibers or the 90 degree ply and support the applied load in parallel but independent of the rest of the structure. Fiber fractures in this volume directly reduce the net section and increase the stress concomitantly in the remaining fibers of the volume. As will be shown in the next section, fiber fractures occur fairly frequently in this laminate type. When the accumulation of fiber fractures causes the net section stress to exceed the net section strength, then failure of all fibers at that section occurs and all load-bearing capacity is lost in that volume.

These splits frequently occur first at the specimen edge when delamination growth is driven by both longitudinal crack and edge-related mechanisms. Longitudinal splits are observed in the interior of specimens as well. In both cases the splits often have substantial length. In preliminary tests with this laminate type, the splits were seen to frequently initiate at the gripped ends. However, specimens

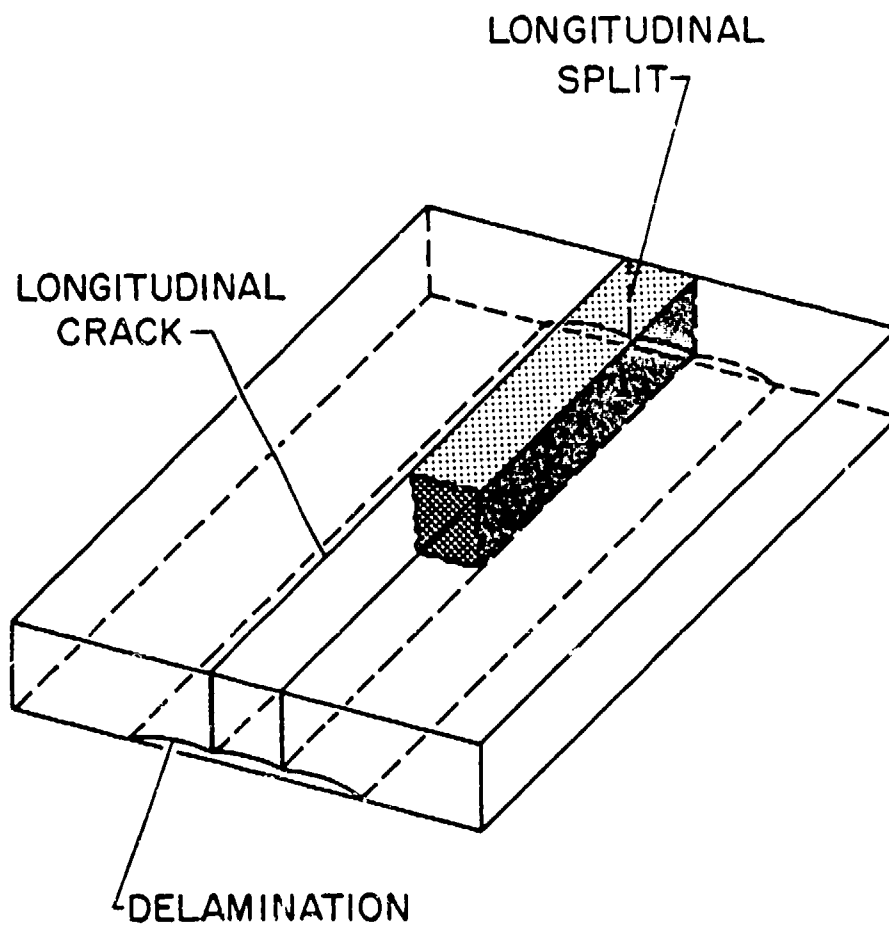


Figure 32. Longitudinal Split Model.

which had thin epoxy layers applied at the ends were less prone to this behavior. It appears that in the former case, the net section fiber failures which initiated the splits may have been caused by the grips.

Longitudinal splitting has a significant effect on laminate stiffness as seen in Stage III of the characteristic stiffness curve. The expected contribution can be simply calculated for a split having a width equal to the average longitudinal crack saturation spacing, 0.063 in. Assuming a linear relationship between the 0 degree ply longitudinal stiffness and the net section width, one can write the following relationship,

$$\frac{E_s}{E_0} = 1 - \frac{W_s}{W_0} \quad (2)$$

where E_s is the 0 degree ply stiffness reduced by the presence of a longitudinal split having a width, W_s ; E_0 is the initial ply stiffness; and W_0 is the original specimen width. In this example, $W_s = 0.063$ in., $W_0 = 1$ in., and $E_0 = 2.055 \times 10^4$ ksi. E_s is calculated from (2) to be 1.926×10^4 ksi (1.328×10^5 MPa). Using this value in a laminated plate analysis, the reduced laminate stiffness is found to be 7.658×10^3 ksi (5.280×10^4 MPa). Comparing this value to the original laminate stiffness of 7.875×10^3 ksi (5.430×10^4 MPa), the calculated stiffness reduction due to the formation of a longitudinal split is 2.8 percent.

This value is approximately twice the average observed value of approximately 1.5 percent. The difference may owe to the fact that in reality a longitudinal split does not result in a total loss of stiffness along the entire length of the specimen. It may also be attributed to the fact that the process of delamination coalescence which precedes longitudinal splitting may occur earlier and more frequently between closely-spaced longitudinal cracks, yielding generally smaller splits than the average spacing would predict.

In summary, fatigue damage development in the $[0,90_2]_s$ laminate type can be characterized as follows: In Stage I the predominant mode is transverse cracking; in Stage II, longitudinal cracks nucleate and grow along the specimen length in the 0 degree plies and produce interior delaminations at the 0/90 degree interfaces; in Stage III these delaminations coalesce in regions between longitudinal cracks, isolating small volumes of material in the 0 degree plies which become longitudinal splits. The measured stiffness reductions can be accounted for by the contributions of the predominant damage modes in each stage of damage.

$[0,\pm 45]_s$ Laminate Type

Overview

The maximum cyclic stress amplitude for all tests was 0.72 S_{ult} . Figure 33 shows the stiffness reduction curve for a typical $[0,\pm 45]_s$ specimen. Stages I, II, and III are marked. Figure 34 shows a series of radiographs made at various points during the fatigue life

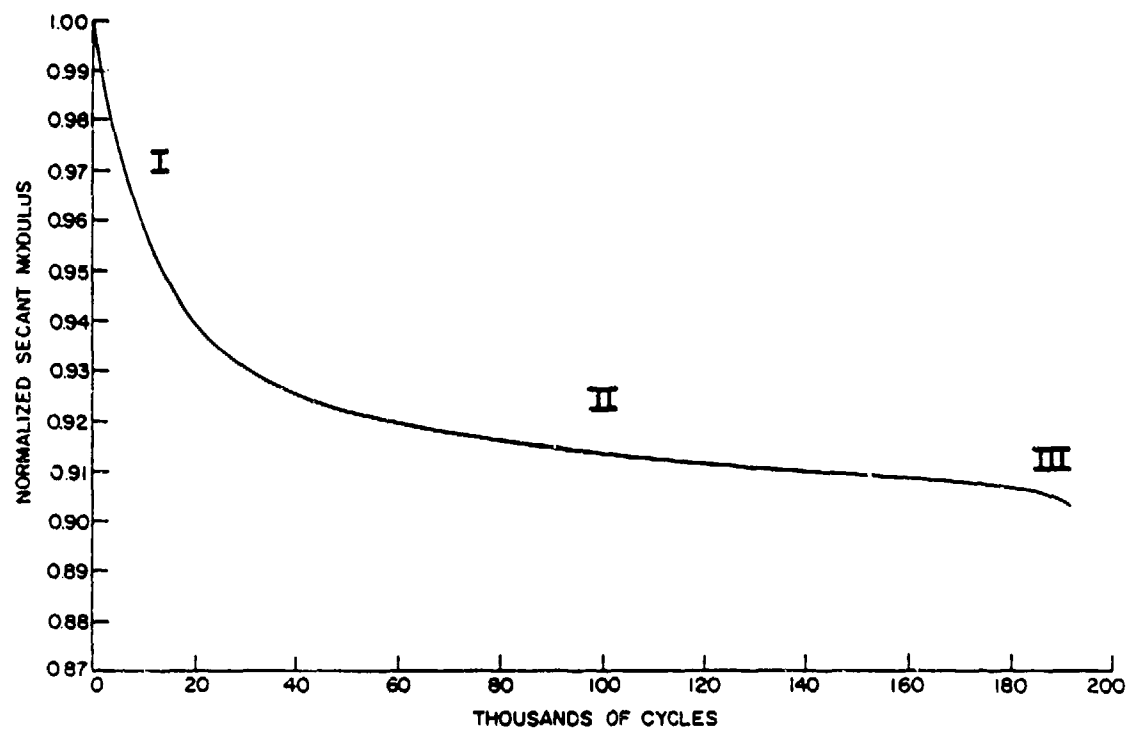


Figure 33. Typical Stiffness Reduction Curve for a $[0, +45]_s$ Laminate.

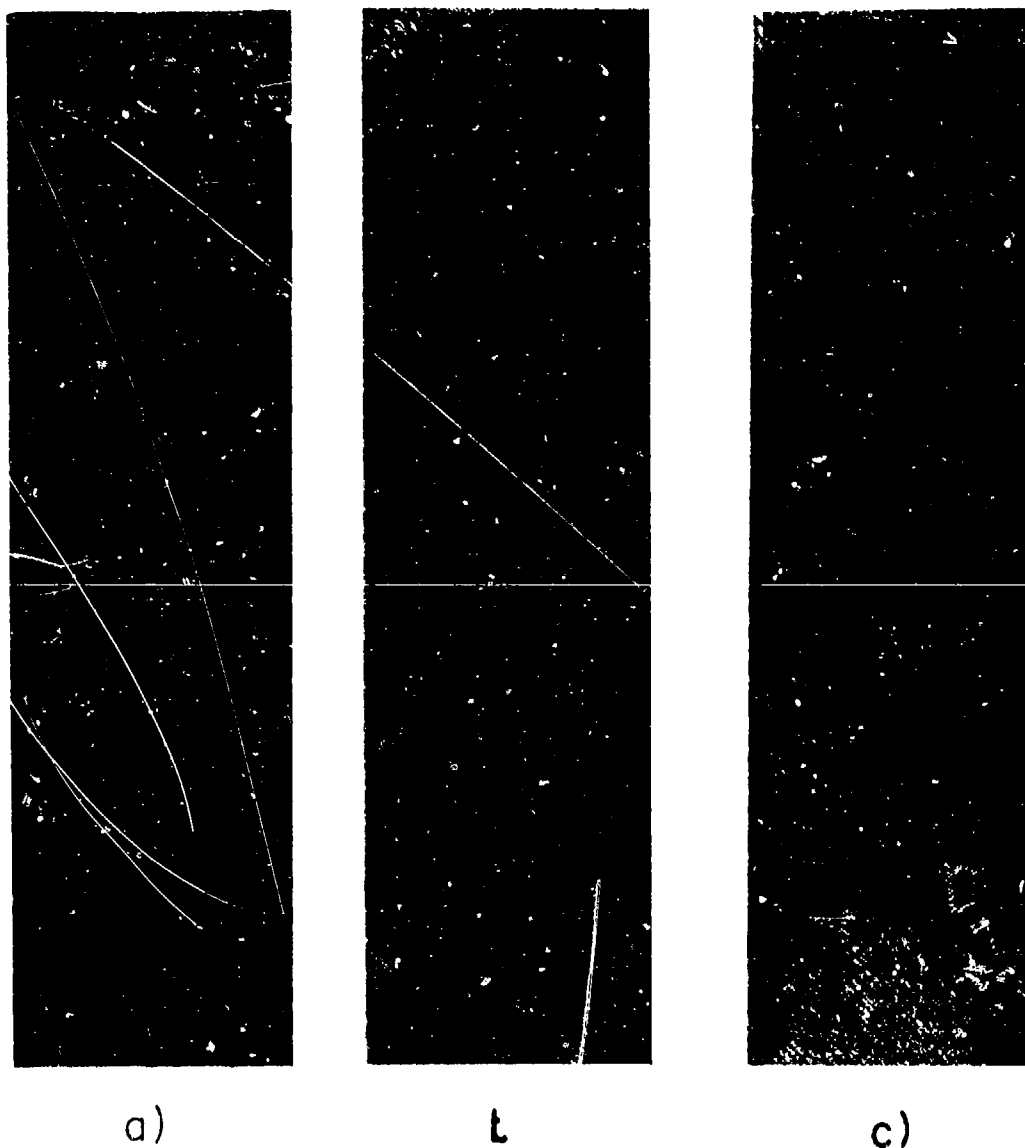


Figure 34. X-ray Radiographs of a Progressively Fatigue-Damaged $[0,+45]_s$ Laminate.

of one specimen. Figure 34(a) shows the virgin specimen. The short diagonal lines above and below the fiducial dot at one edge of the specimen correspond to seams in the laminate where sections of the prepreg tape were joined. Since the tape was 6 in. wide and the specimens were 8 or 9 in. long, such seams were unavoidable. Identification of this detail as a seam was accomplished by deplying virgin specimens for comparison with radiographs, C-scans, and edge micrographs of the specimen. In each case, the apparent flaw could be associated with a distinct irregularity in one of the deplied laminae at that location. The irregularity frequently was a disturbance in the fiber alignment. Misalignment can result from attempts to force adjacent ply tapes together during fabrication. Misalignments also were observed to occur in the prepreg material as received, likely as a result of the fabrication process. Penetrant-enhanced radiography and ultrasonic C-scans proved to be very sensitive to these structures. Fortunately, in most cases, including the specimens of Fig. 34, these flaws were not sites of preferential damage growth or failure. The practice of radiographing virgin specimens, however, provided a basis for separating such defects from damage.

Figure 34(b) is the same specimen after 40,000 cycles of tension-tension cyclic loading, resulting in 4.9 percent stiffness reduction. Patterns of dark, diagonal lines corresponding to cracks in off-axis plies are seen to have formed. The darkest lines are those running from top right to bottom left diagonally across the width of the specimen. These are cracks in the two -45 degree plies

in the center of the laminate. A companion set of lighter lines can be seen running across the width on the opposite diagonal. Edge replicas made at this point indicate that neither of these ply orientations has achieved the predicted characteristic damage state saturation spacing of 0.016 in. (0.40 mm) for the +45 degree plies and 0.029 in. (0.73 mm) for the -45 degree plies. The measured stiffness reduction of 4.9 percent places this specimen in Stage I of damage development.

Figure 34(c) is a radiograph of the same specimen after 114,000 cycles with 10.8 percent stiffness reduction. The density of both sets of off-axis cracks has increased. In addition, cracks which were seen under microscopic examination to be incompletely developed in Fig. 34(b) are now seen to extend fully across the specimen width. Finally, narrow longitudinal cracks are seen to have formed at both edges. The measured stiffness reduction of 10.8 percent places this specimen at the end of Stage II or beginning of Stage III on the characteristic curve.

Details of the damage in the $[0, \pm 45]_S$ laminate type are considered next.

Stage I

Figure 35 is a portion of an edge replica taken at the end of 11,000 cycles with 5.1 percent stiffness reduction. The measured crack spacing of 0.019 in. (0.47 mm) for the +45 degree plies and 0.033 in. (0.85 mm) for the -45 degree plies are 81 percent and 100 percent respectively of the predicted CDS values. There is little

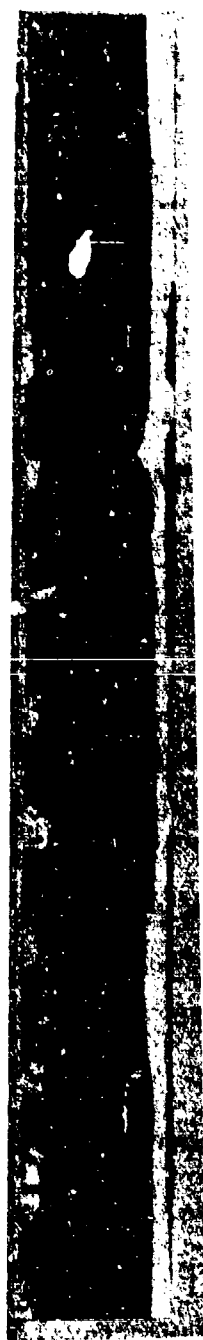


Figure 35. Edge Replica from a $[0, +45]_s$ Laminate at Stage I.

evidence of crack coupling or edge delamination at this stage.

Figure 36 is a radiograph of the same specimen at this stage. The developing off-axis cracks are seen. Microscopic examination shows that the +45 degree plies are significantly more segmented than are the -45 degree cracks. There are perhaps two reasons for this. First, the +45 degree ply cracks are one ply in thickness while the -45 degree cracks are two plies thick. Hence the crack tip stresses in the latter case would be expected to be greater, a factor in transverse crack growth. Second, although the transverse stresses in both plies are comparable from laminated plate theory, the magnitude of the shear stress in the -45 degree plies is approximately 1.5 times greater than the shear stress in the +45 degree plies. To the extent that crack extensions can be attributed to a mode II mechanism, this difference would favor growth of cracks in the -45 degree plies as is observed.

Stage II

Figure 37 is a portion of an edge replica taken at the end of 382,000 cycles, with an 8.2 percent stiffness reduction. The measured crack spacing of 0.018 in. (0.46 mm) for the +45 degree plies and 0.030 in. (0.76 mm) for the -45 degree plies are 82 percent and 112 percent respectively of the predicted CDS values. Except for the increased crack density there is little difference to be observed in comparison to Fig. 35. Figure 38 is a radiograph of the same specimen. Nearly all of the -45 degree ply cracks are seen to extend completely across the specimen width. Under microscopic examination,

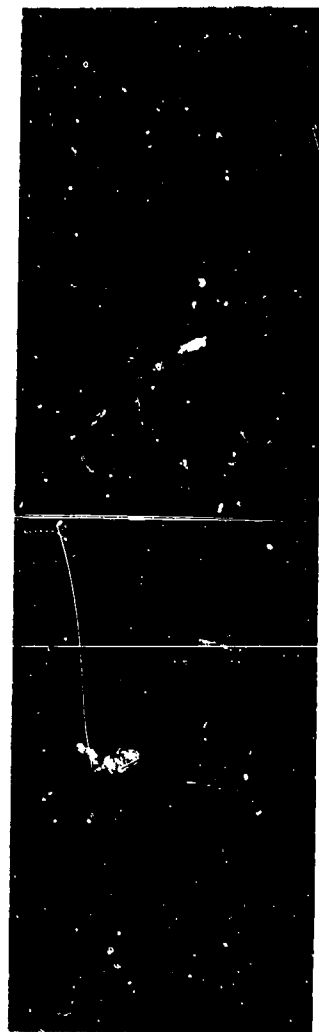


Figure 36. X-ray Radiograph of a $[0,+45]_s$ Laminate at Stage I.

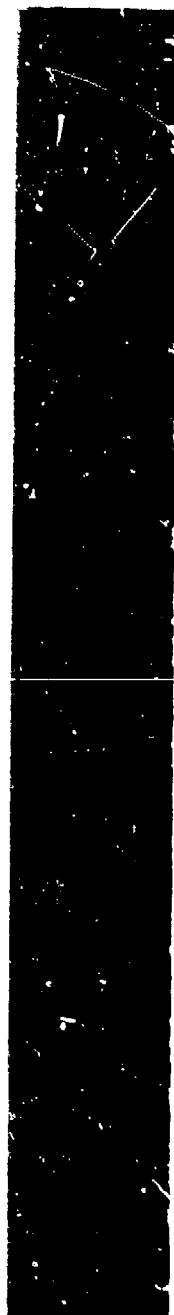


Figure 37. Edge Replica from a $[0, +45]_s$ Laminate at Stage II.

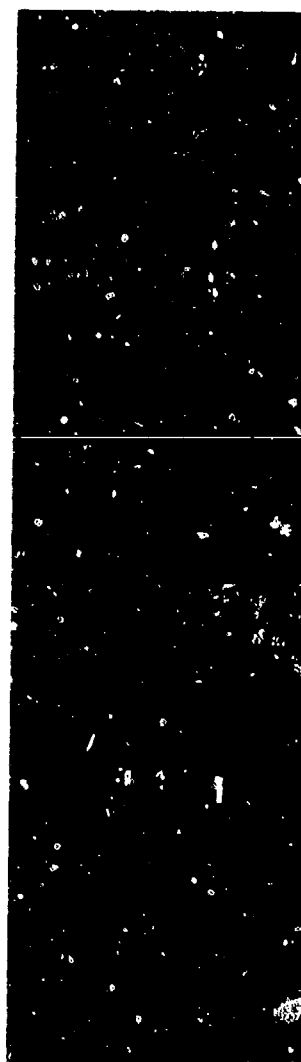


Figure 38. X-ray Radiograph of a $[0, +45]_S$ Laminate at Stage II.

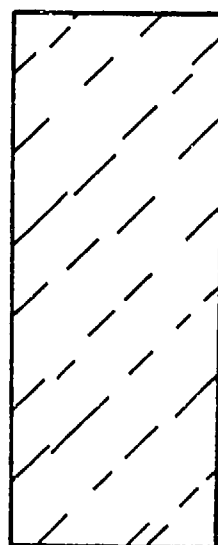
the +45 degree ply cracks have the appearance of the drawing in Fig. 39.

Stage II in the $[0, \pm 45]_S$ laminate types is perhaps best distinguished by what is not happening. There is not a strong interlaminar normal or shear stress condition to promote edge delamination and no apparent internal mechanism, as in the $[0, 90_2]_S$ case, to produce internal delamination. With the exception of narrow delaminations associated with 0 degree ply longitudinal splits which occurred at the edge of some specimens, delamination was, in fact, not observed for this laminate type. The effect on stiffness reduction was marked. Except for the completion of off-axis ply cracking during Stage II, no additional stiffness reduction damage mode was operative and for several specimens there was no further measurable reduction in stiffness. This is somewhat remarkable inasmuch as Stage II often accounted for several hundred thousand cycles of the specimen fatigue life.

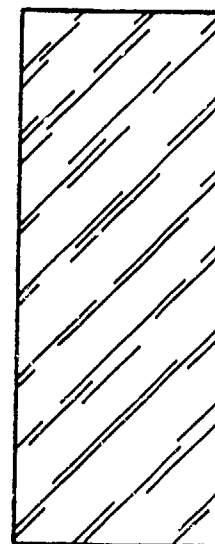
Stage III

Figure 40 is a portion of an edge replica taken at the end of 258,000 cycles with 7.1 percent stiffness reduction. There is some local crack coupling to be noted but little else distinguishes the edge condition from preceding damage stages. In the characteristic curve, Stage III is distinguished by a sudden stiffness reduction of between 0.5 and 1.0 percent terminated by failure of the specimen.

Figure 41 is a radiograph of the same specimen. The radiograph is different from that of Stage II. Dark, diagonal structures along



I



II

Figure 39. Crack Development in the +45 Degree Plies of a $[0, +45]_s$ Laminate.



Figure 40. Edge Replica from a $[0, \pm 45]_S$ Laminate at Stage III.

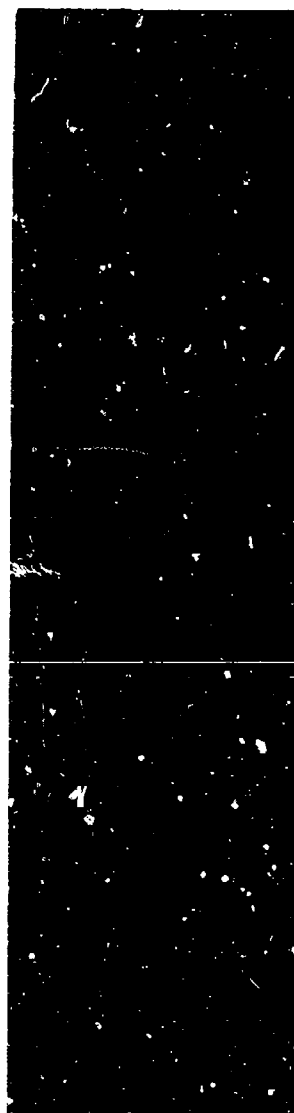


Figure 41. X-ray Radiograph of a $[0,+45]_s$ Laminate at Stage III.

both +45 degrees and -45 degree directions are seen in the stereo microscope to be relatively large angle-ply cracks. At the interfaces adjacent to these cracks are seen in several regions numerous microcracks so closely spaced that they almost constitute small delaminations. The microcrack directions are aligned with the direction of fibers in their plane. Invoking the simple LEFM crack tip stress field model used to describe longitudinal crack nucleation in $[0,90_2]_s$ laminates, Figure 42(a) shows how microcracks in orthogonal directions might form at the interface between +45 degree and -45 degree plies in response to existing cracks in those plies. Such a model would also predict microcracks at the 0/+45 degree interface in the manner of Figure 42(b). Such cracks are observed microscopically as well as macroscopically in the radiograph of Fig. 41.

Is this damage which appears to be characteristic of Stage III sufficient to account for as much as one percent stiffness reduction? Using the laminated plate theory, it is seen that the $[0,\pm45]_s$ laminate stiffness is strongly affected by changes in the transverse and shear moduli of the angle plies and essentially unaffected by changes of those quantities in the 0 degree plies. For example, if these moduli are considered to be fully discounted when the CDS crack spacing is achieved, the net stiffness reduction is 21 percent. If a 50 percent discount in both moduli is assumed, then the stiffness reduction is 10 percent, approximately that which is observed. With such a large influence on longitudinal stiffness, any

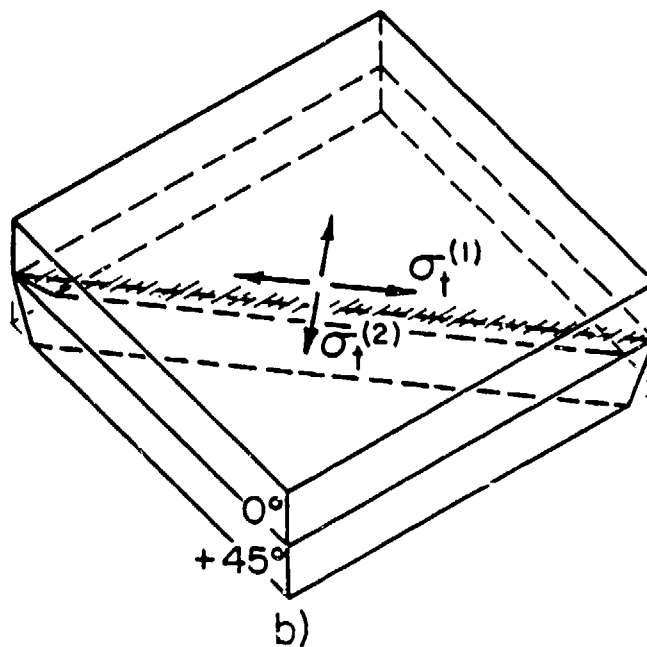
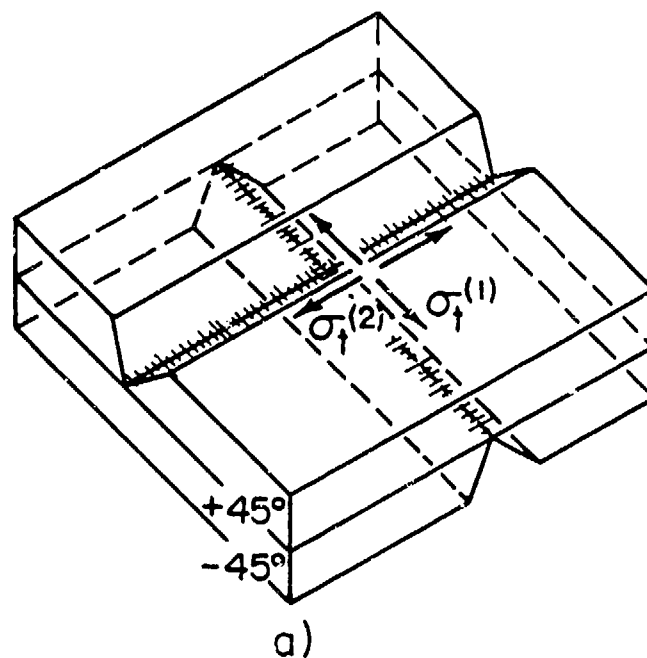


Figure 42. Model for Microcrack Formation in $[0, \pm 45]_S$ Laminates.

damage occurrence which would alter, even in a small or local way the actual stiffness reduction in the ply, could have an observable influence on the measured stiffness. The physical evidence of additional ply cracking suggests the possible existence of such a mechanism in Stage III. However the difficulty of capturing a $[0, \pm 45]_s$ specimen in Stage III has prevented the elevation of this explanation beyond conjecture. Specifically unanswered is the association of the rapid rate of stiffness reduction observed in Stage III with the rate of development of this advanced ply cracking damage.

In summary, damage development in the $[0, \pm 45]_s$ laminate type can be characterized as follows: In Stage I, the predominant mode is cracking of the ± 45 degree plies. This process is relatively slower than for the $[0, 90]_s$ laminate type and when completed yields a much higher contribution to laminate stiffness reduction. In Stage II, there is very little stiffness reduction observed and no evidence of a predominant damage mode. This stage is notable for an absence of delamination. Stage III is quite abrupt when it is observed and of small magnitude.

$[0, 90, \pm 45]_s$ Laminate Type

Overview

The maximum cyclic stress amplitude for all tests was $0.62 S_{ult}$. Figure 42 shows the stiffness reduction curve for a $[0, 90, \pm 45]_s$ specimen with Stage I, II, and III marked. Figure 44 is a series of radiographs made at various points during the fatigue life

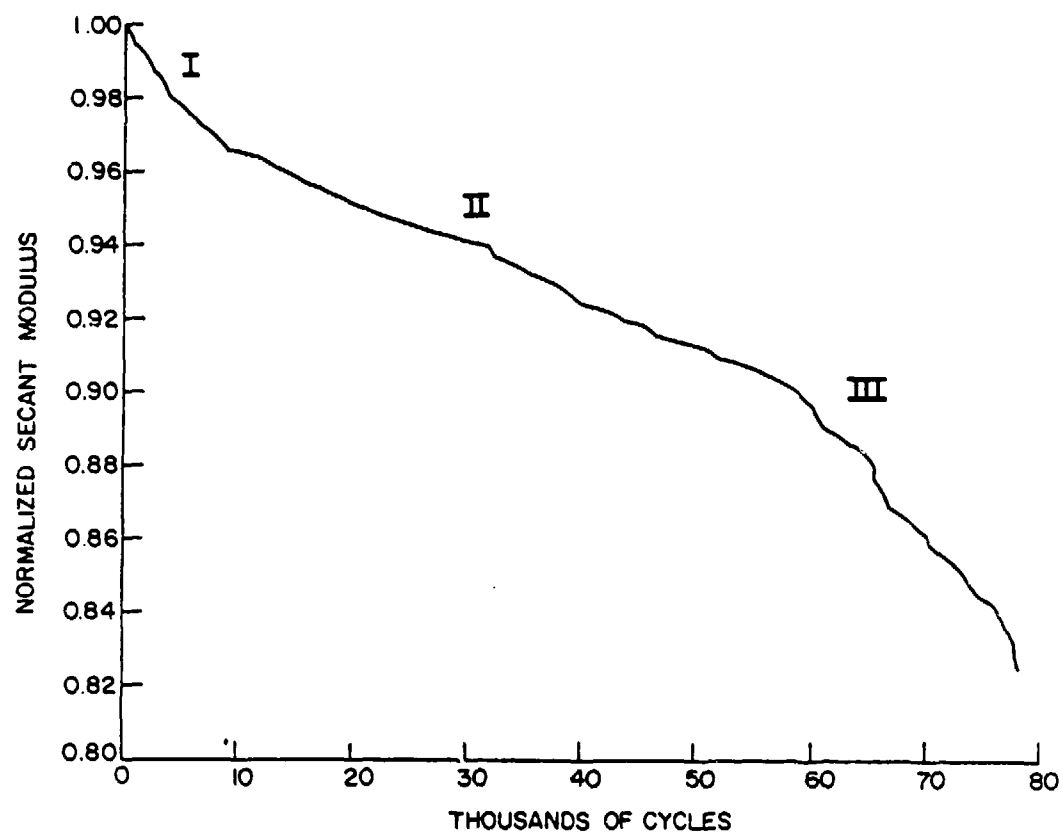
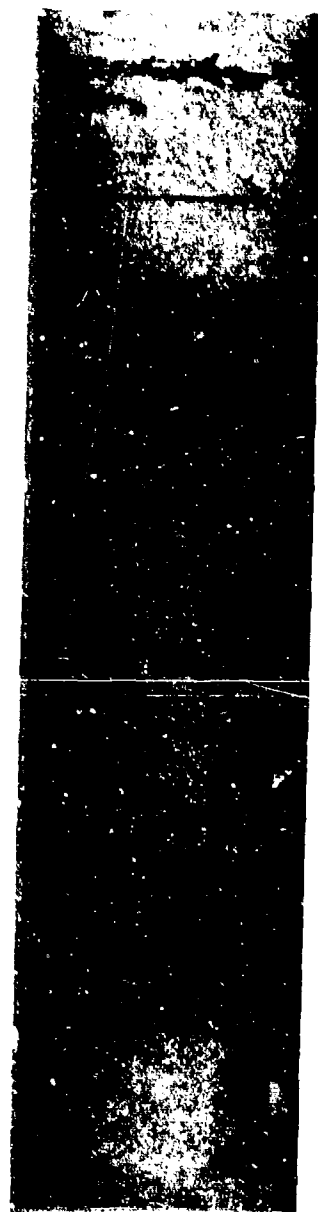
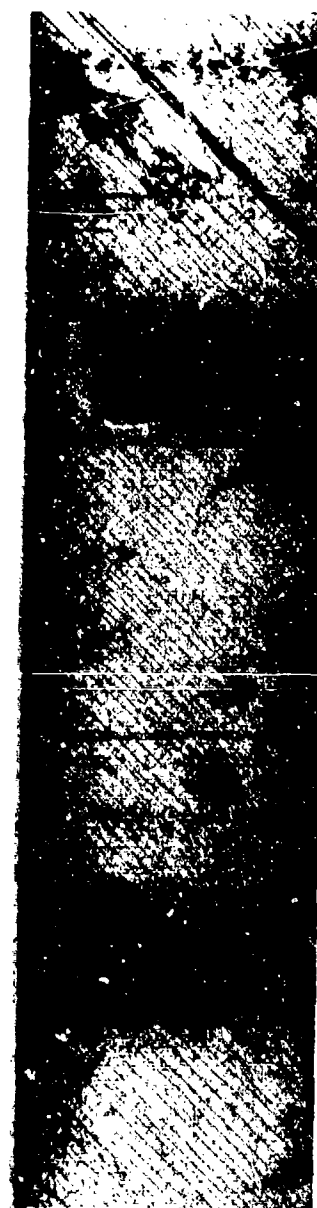


Figure 43. Typical Stiffness Reduction Curve for a $[0,90,+45]_s$ Laminate.

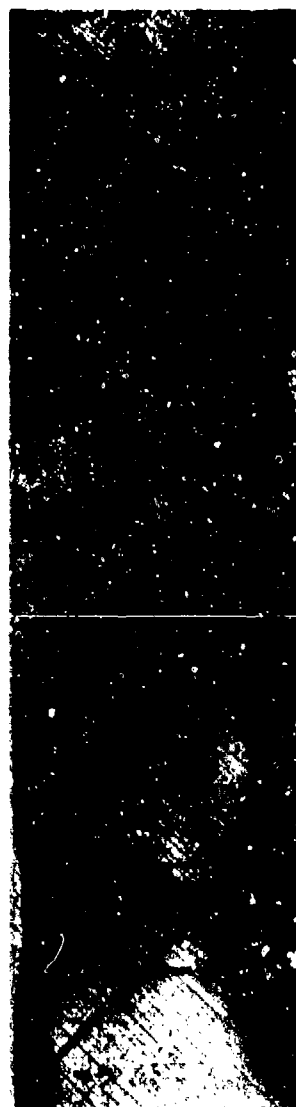


a)

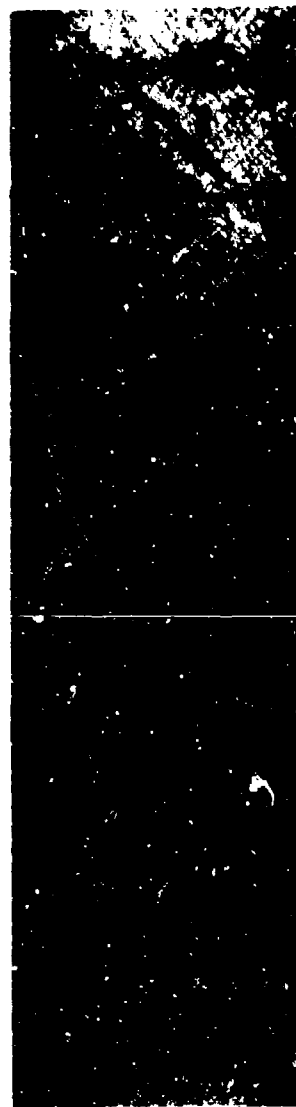


b)

Figure 44. X-ray Radiographs of a Progressively Fatigue-Damaged $[0,90,+45]_s$ Laminate.



c)



d)

Figure 44. X-ray Radiograph of a Progressively Fatigue-Damaged $[0,90,+45]_S$ Laminate (Cont'd.).

of one specimen. Figure 44(a) shows the virgin specimen. Three ply seams are observable, one in each of the inner ply directions. As in the other laminate types, these structures were prominent in radiographs and C-scans but had no apparent involvement in localizing damage development or specimen fracture. Evident also along the specimen edges are web-like structures which are seen stereoptically to be regions of porosity existing at each of the specimen interfaces. They exist in fact throughout the specimen but are not initially reached completely by the zinc iodide X-ray enhancing agent. At higher magnification, each branch of the porosity structures is seen to possess a dark core having a width dimension on the order of the carbon fiber bundle diameter. Examination of the graphite epoxy prepreg tape before fabrication and of deplied laminae afterward showed that these core structures were indeed individual fiber bundles. It appears that a major source of porosity in these specimens are misaligned fiber bundles. These individual fiber bundles become pressed between plies during fabrication and form micro-delaminations which trap gases evolved during curing which otherwise would escape. Fortunately, these zones of porosity appear to be benign in the development of damage in most cases. However, when porosity intersects the edges of delamination-prone interfaces in the $[0,90,\pm45]_S$ laminates, delamination frequently begins at those edges. Figure 44(b) is the same specimen after 32,000 cycles of tension-tension loading, 6 percent stiffness reduction. Patterns of ply cracks are seen to have developed, most prominent those in the

two-ply thick-45 degree plies. Also observed are incipient delaminations at both edges. The largest, to the right of the extensometer mounting tabs, is seen upon stereoptical inspection to be at one of the 0/90 degree interfaces. The wide, horizontal lines between the mounting tabs are fiducial markers.

Figure 44(c) is the same specimen after 78,000 cycles and 18 percent stiffness reduction. Microscopically, the crack density in each ply is seen to be greater than in Fig. 44(b). However, the most dramatic difference lies in the growth of delaminations from the specimen edge significantly into the interior. Stereoptically these delaminations are observed at the +45/-45 degree interfaces as well as the 90/+45 degree interfaces. This observation was confirmed when this specimen was deplated and the gold chloride boundary of each delamination was examined. This method will be discussed fully in a following section.

Figure 44(d) is the same specimen in the same condition of damage development as shown in Fig. 44(c). However the radiograph was made ten days later. Continuing diffusion and evaporation of the zinc iodide mixture has caused the delamination boundaries to consolidate. The true extent of the delamination is more easily distinguished as are regions of delamination overlap. However some loss of definition of the angle ply cracks is seen to have occurred during the interval.

Figure 45 shows a series of edge replicas taken from the same specimen at various stages of damage development. Figure 45(a) shows



a)

b)

c)

Figure 45. Edge Replicas from a Progressively Fatigue-Damaged $[0,90,+45]_S$ Laminate.

the edge condition at 32,000 cycles and 6 percent stiffness reduction. Cracking in each of the angle plies is observed although none has reached the predicted CDS spacing. Small delaminations occur at both of the +45/-45 degree interfaces. A large delamination is observed at one of the 90/+45 interfaces which has joined with one of several crack-coupled delaminations at one of the 0/90 degree interfaces. At 60,000 cycles and 10.4 percent stiffness reduction, shown in Fig. 45(b), the crack density in the 90 degree and +45 degree plies, and more gradually in the -45 degree plies are approaching the CDS condition. The coupled delamination has grown substantially along both the 0/90 degree interface the 90/+45 degree interface. One of the +45/-45 degree interfaces also shows substantial growth along the edge. Figure 45(c) shows the edge condition at 78,000 cycles with 18 percent stiffness reduction. Cracking in each ply is complete at this point and with the exception of crack coupling, particularly between the +45 degree and 90 degree plies, the picture is not remarkably different from that of Fig. 45(b).

The average stiffness reduction exhibited during the first half cycle for the $[0,90,+45]_5$ laminate was 1.7 percent. As in the discussions of the previous laminate types, this amount is not reflected in the measurement of secant modulus reported in the following sections except when noted in calculations involving delamination growth.

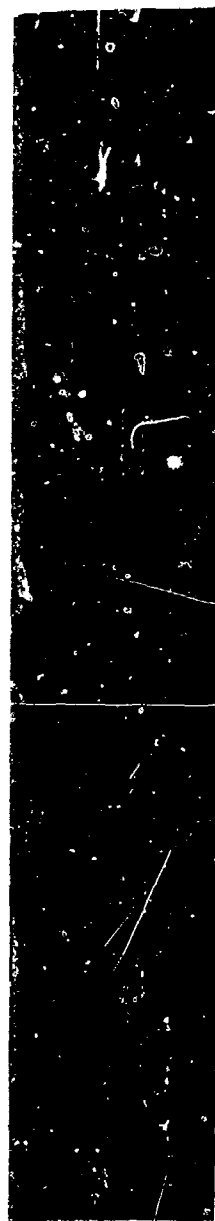
Stage I

Figure 46 shows edge replicas made at the end of 30,000 cycles with 3.5 percent stiffness reduction on the right edge (a), and on the left edge (b). Both replicas show cracks in each of the angle plies. However, the right side replica also shows the beginning of a delamination at one of the 90/+45 degree interfaces which has coupled with a 90 degree crack and entered the 0/90 degree interface. This asymmetry of delamination incipency was frequently observed and may be related to the distribution of porosity in a particular specimen and to slight loading misalignments.

Figure 47 is a radiograph of the same specimen. The planar extent of the delamination at one edge is evident. The dot in the center is a fiducial mark. Extension of ply cracking across the width is seen to be incomplete in the +45 degree plies and to a lesser extent in the -45 degree and 90 degree plies. The development of the CDS crack spacing is also not complete in any ply, although as Fig. 48 shows, a substantial portion of crack formation is typically complete at this point. The stiffness reduction observed in Stage I of the $[0,90,\pm45]_5$ laminate type, as in the other laminate types discussed previously is associated principally with off-axis ply cracking, i.e., with the development of the characteristic damage state.

Stage II

Figure 49 is an edge replica made from another specimen at the end of 326,000 cycles with 13 percent stiffness reduction. Off-axis cracking is essentially complete in each off-axis ply. Delamination



a)



b)

Figure 46. Edge Replicas from a Progressively Fatigue-Damaged $[0,90,+45]_s$ Laminate.

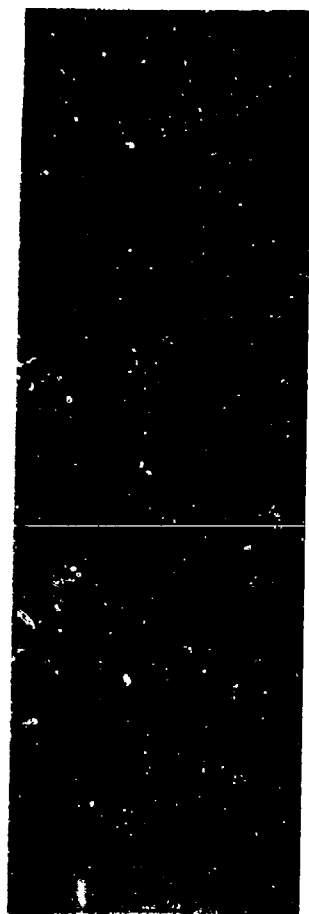


Figure 47. X-ray Radiograph of a $[0,90,+45]_S$ Laminate at Stage I.

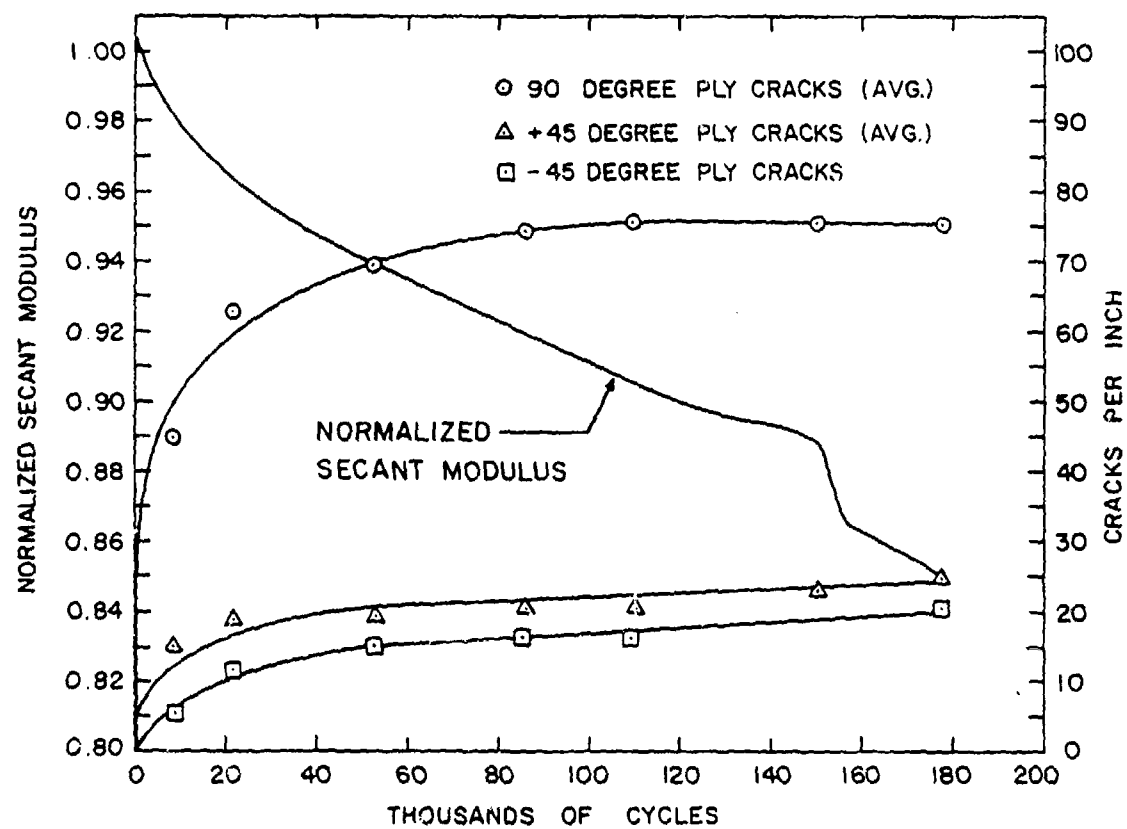


Figure 48. Stiffness Reduction and Crack Development in a $[0,90,+45]_S$ Laminate.

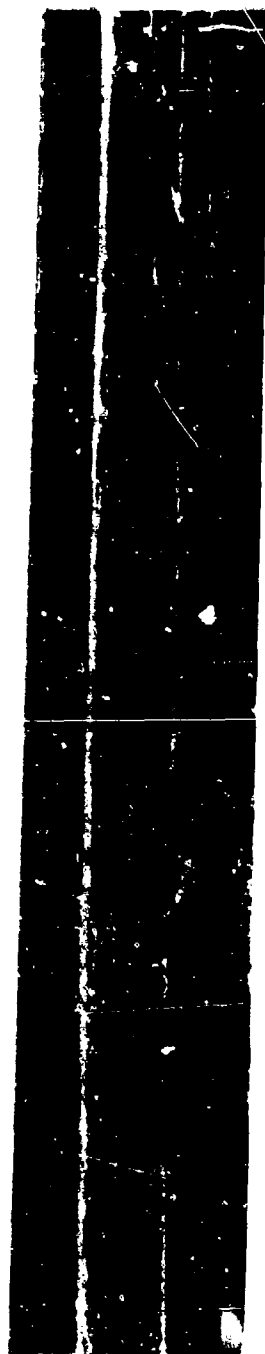


Figure 49. Edge Replica from a $[0,90,_{+45}]_S$ Laminate at Stage II.

growth is apparent by comparison with Fig. 46. Long delaminations are evident at both 90/+45 degree and +45/-45 degree interfaces. These and smaller delaminations are seen to cross from one interface to another at ply cracks to involve each of the laminate interfaces. Figure 50 is a radiograph of the same specimen. Significant delamination incursions into the width are observed. Some asymmetry of development is evident but both edges are fully involved. By stereoptical examination of this radiograph, the widest delaminations were observed to be in the 90/+45 interfaces. Smaller but substantial delaminations were also observed in the +45/-45 degree interfaces. Little delamination was observed at the 0/90 degree interfaces. These assignments of delaminations to interfaces were verified when this specimen was depled for additional examination.

It was noticed in this specimen, as in others, that delaminations typically grew first along the length quickly and then across the width more slowly. The rationale for such behavior lies in the boundary layer isolation of the interlaminar stresses which provide the initial impetus for delamination growth. Once the delamination has grown along the length in response to these stresses, the stress state is modified by the damage. The free edge effectively and selectively moves inward and with it altered but viable interlaminar stresses.

Delamination is the predominant damage mode observed in Stage II for the $[0,90,\pm45]_5$ laminate type. The stiffness reduction curve associated with this stage is approximately linear. Using a simple analysis proposed by O'Brien [62], the relationship between



Figure 50. X-ray Radiograph of a $[0,90,+45]_S$ Laminate at Stage II.

delamination growth and stiffness reduction for this laminate type was examined more closely.

In principle, the analysis is the rule of mixtures for laminate stiffness. From laminated plate theory, the undamaged laminate stiffness, E_{LAM} , is calculated. Next, a complete delamination in one or more interfaces is assumed. Using the rule of mixtures assumption that the sublaminates formed undergo the same axial strain (but not necessarily the same transverse strain), a fully delaminated stiffness E^* , is calculated,

$$E^* = \frac{\sum_{i=1}^m E_i t_i}{\sum_{i=1}^m t_i} \quad (3)$$

where

m = number of sublaminates formed by the delamination

E_i = laminate stiffness of the i th sublaminate

t_i = thickness of the i th sublaminate

For the case where delaminations are not complete, equal sized delaminates strips of width $a/2$ are assumed to exist at both edges of the laminate whose width is b . By assuming that the laminated and delaminated portions of the specimen act as independent components loaded in parallel, the rule of mixtures yields an expression for the partially delaminated laminate stiffness, E ,

$$E = (E^* - E_{LAM}) \frac{a}{b} + E_{LAM} \quad (4)$$

where E_{LAM} is the original laminate stiffness. In terms of the ratio of total delaminated area, A , to the total interfacial area, A^* , equation (4) can be rewritten as

$$E = (E^* - E_{LAM}) \frac{A}{A^*} + E_{LAM} \quad (5)$$

Equation (5) then provides a means by which observed delaminations in the $[0,90,\pm45]_S$ laminate type can be related to measured stiffness reduction. The quantity E_{LAM} can be calculated from laminated plate theory. The quantity A^* , was calculated using an assumed sublaminde development shown in Fig. 51. This choice was based on the experimental observation that in the $[0,90,\pm45]_S$ laminate type, negligible delamination occurred at the 0/90 degree interfaces. In order to calculate the delaminated area at each of these interfaces, specimens representing each stage of damage development were treated with gold chloride and deplated. As noted in Chapter 3, under proper illumination conditions the gold chloride particles marking the delamination boundaries could be clearly distinguished. By placing a sheet of clear plastic film over the ply, the outline of each delamination was traced with an ink marking pen. Figure 52 shows the set of delamination tracings from a typical specimen. The interfacial area, A^* , for each ply was equal to the specimen width (1 in.) times the extensometer gage length (2 in.). The delamination area was measured with a planimeter. Three measurements of each delamination were made to minimize error and the average value was used. Moreover, since two sets of delamination tracings, one for each facing ply, were made,

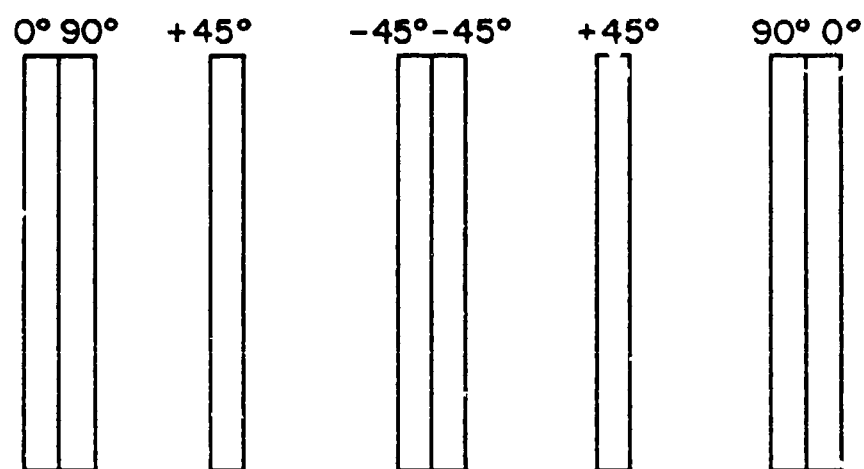


Figure 51. Sublaminates Resulting from Delamination in a $[0,90,+45]_s$ Laminate.

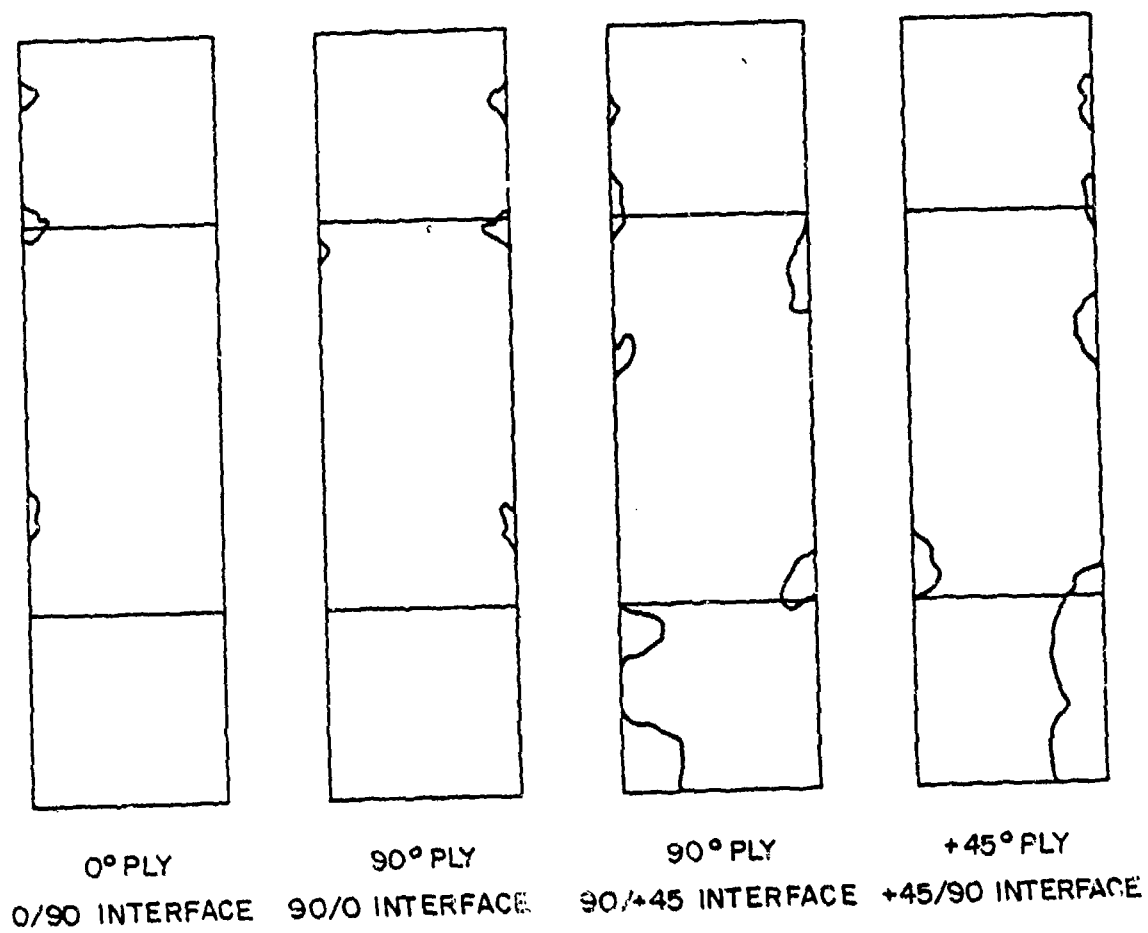


Figure 52. Delamination Boundaries in a $[0,90,+45]_s$ Laminate.

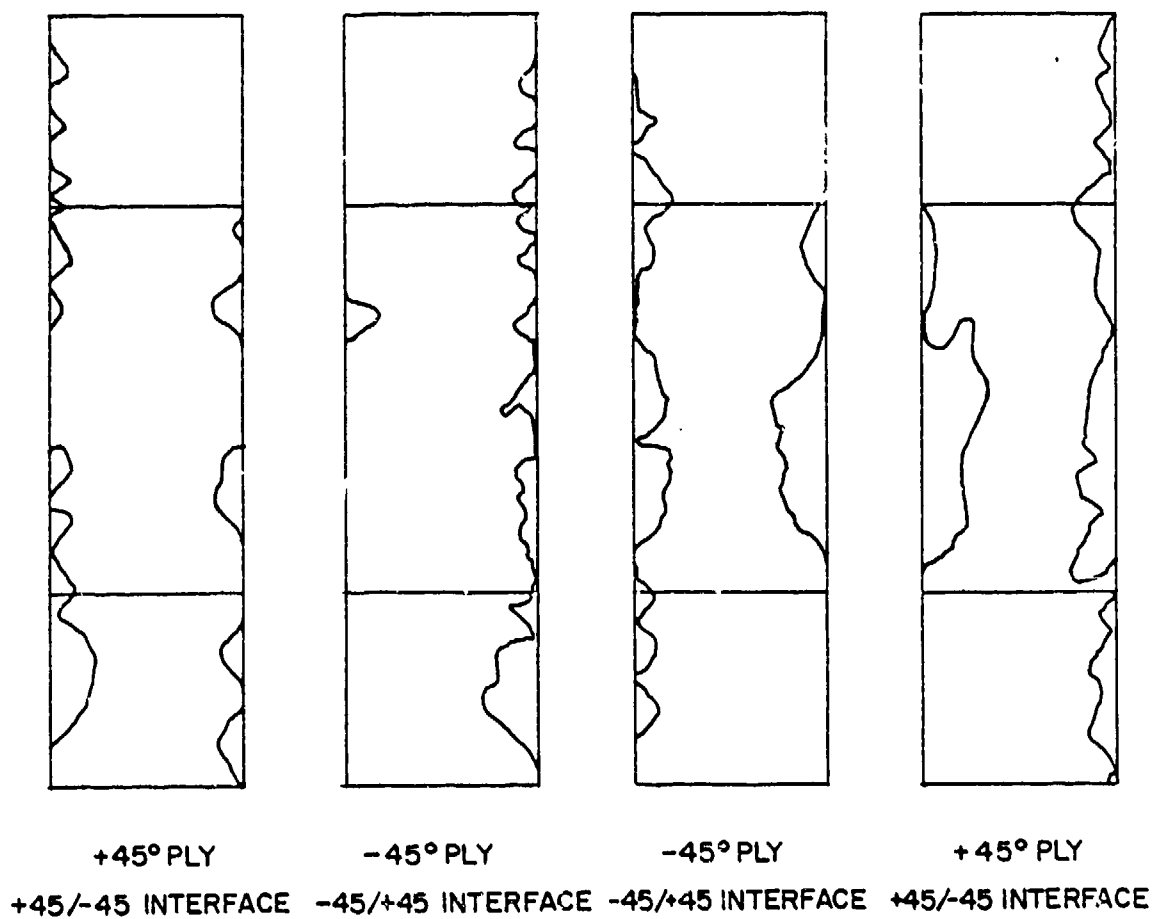


Figure 52. Deamination Boundaries in a $[0,90,+45]_S$ Laminate
(Cont'd.)

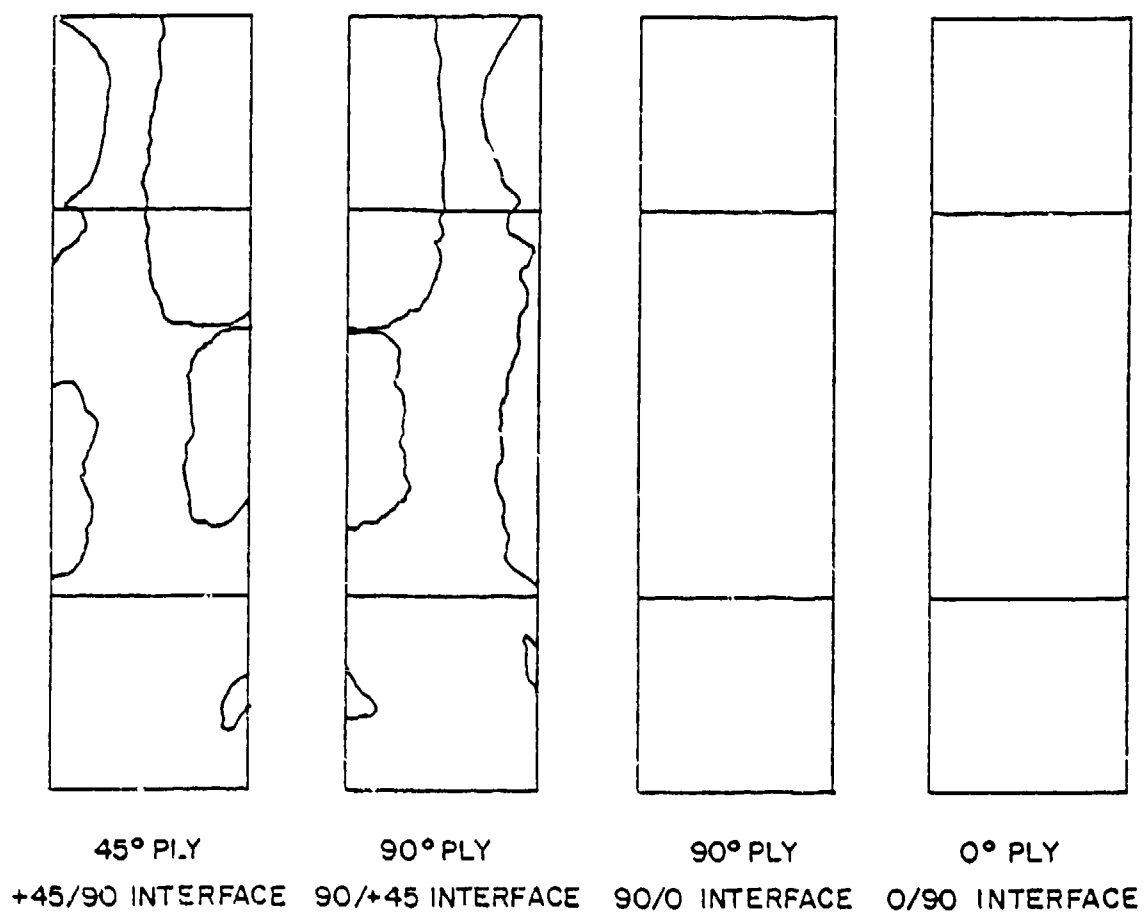


Figure 52. Delamination Boundaries in a $[0,90,+45]_s$ Laminate (Cont'd.).

each delamination area was actually measured twice. The value used for A, the delamination area, was the average of those two measurements.

Table V summarizes the results for four $[0,90,\pm45]_S$ specimens at various stages of damage. The first two columns identify the specimen and condition. The third column shows the fraction of the total sub-laminate interfacial area which was delaminated. The fourth column shows the reduced laminate stiffness as a result of ply cracking and delamination. The quantity ΔE_{DEL} in the next column represents the percentage of stiffness reduction attributable to delamination alone. The next column, ΔE_{TOTAL} , represents the total calculated stiffness reduction including both cracks and delaminations. The last column shows measured values of the total stiffness reduction. The calculated and measured values were taken over the same two inch gage length. Agreement between the calculated and measured values is seen to be reasonably good. The measurement for specimen III--L-1-12 (Stage I condition) is compared to a calculated value of laminate stiffness based on a fifty percent discount of transverse stiffness and shear moduli in off-axis plies to reflect the incomplete development of cracks at the end of Stage I. All other calculations are based on fully-discounted off-axis moduli.

Figure 53 shows the relationship between measured delamination size and measured stiffness reduction due to delamination. The latter quantity represents the difference between the total measured stiffness reduction and the calculated stiffness due to ply cracking. The

Table 5. Calculated and Measured Laminate Stiffness Reduction due to Ply Cracking and Delamination

<u>Specimen</u>	<u>Condition</u>	<u>A/A*</u>	<u>E</u>	<u>ΔE_{DEL}</u>	<u>ΔE_{TOTAL}</u>	<u>ΔE_{MEAS}</u>
		(msi)	(%)	(%)	(%)	
III-L-1-23	Stage I	0.083	7.32 ¹	1.7	<u>7.1</u>	<u>5.2</u>
III-L-1-22	Stage II	0.186	6.64 ²	4.2	<u>15.8</u>	<u>14.7</u>
III-L-1-15	Stage III	0.189	6.60 ²	4.8	<u>16.4</u>	<u>16.7</u>
III-L-1-21	Stage III	0.303	6.41 ²	7.6	<u>18.8</u>	<u>19.7</u>
	NEAR FAILURE					

1. Off-axis ply E_2 and G_{12} discounted 50 percent
2. Off-axis ply E_2 and G_{12} discounted 100 percent

Reference Values:

$E_{(UNDAMAGED)}$ =	7.89 msi
$E_{FULLY CRACKED}$ =	6.93 msi
$E_{50\% CRACKED AND DELAMINATED}$ =	5.90 msi
$E_{FULLY CRACKED AND DELAMINATED}$ =	5.19 msi

A = Delaminated Area

A* = Total Interfacial Area

E = Laminate Stiffness with Partial Delamination

ΔE_{DEL} = Stiffness Reduction due to Delamination Only

ΔE_{TOTAL} = Stiffness Reduction due to Cracking and Delamination

ΔE_{MEAS} = Measured Stiffness Reduction

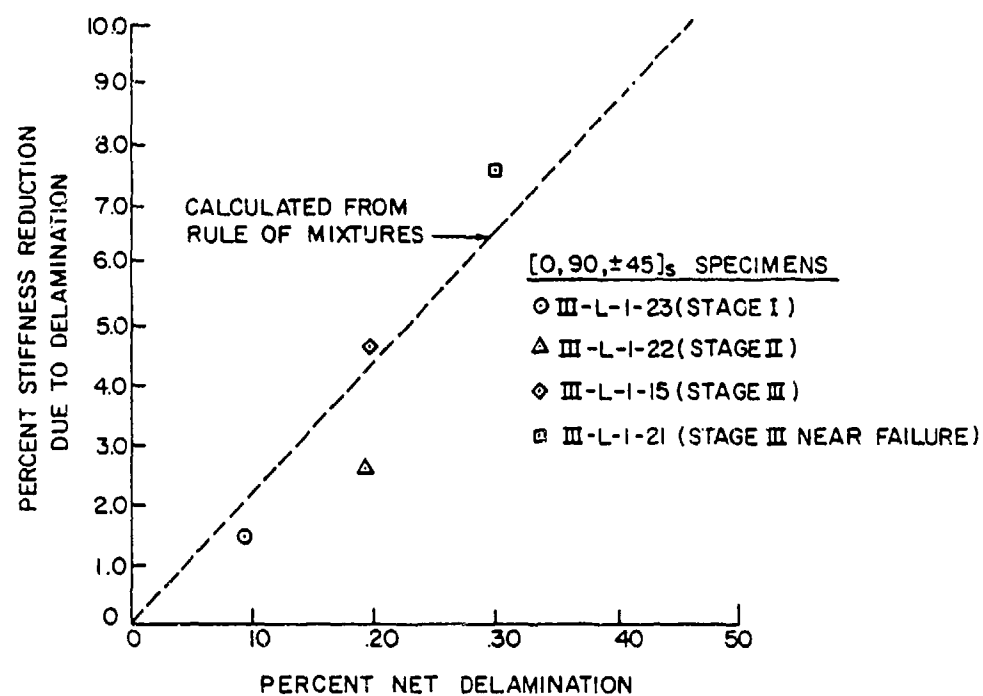


Figure 53. Stiffness and Delamination Relationship for $[0,90,\pm45]_s$ Laminates.

rule of mixtures prediction is also shown. Generally good agreement confirms the linear relationship between stiffness and delamination size for the $[0,90,\pm45]_s$ type.

Stage III

Figure 54 is an edge replica taken from a specimen after 177,000 cycles with 15 percent stiffness reduction. Long edge delaminations are evident, but by comparison with Fig. 49, a Stage II specimen replica, no significant difference in the edge damage condition is observed. The damage is in fact growing into the specimen interior as shown in Fig. 55, a radiograph of the same specimen. Large delamination incursions are observed. Stereoptically they can be placed at the $90/+45$ degree and $+45/-45$ degree interfaces. The net delamination for the specimen is approximately 19 percent.

Figure 56 is an enlargement of the central portion of Fig. 55. Among the dark lines which are the off-axis cracks can be seen a dense substructure of microcracks aligned with the principal fiber directions. Stereoptical examination of this and other Stage III radiographs place these microcracks at or near ply interfaces. Moreover, the majority of microcracks at a given interface are clustered about the ply cracks at that interface. The direction of the microcracks appears to be determined by the fiber direction of the ply in which they form. Examples are shown schematically in Fig. 57.

The appearance of microcracks was observed to a lesser extent in the other laminate types and the same local tensile crack tip stress field model previously proposed can be applied as well to this case.

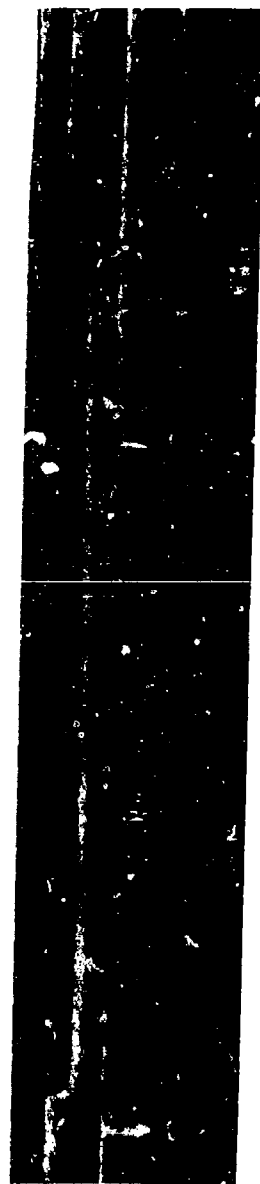


Figure 54. Edge Replica from a $[0,90,+45]_s$ Laminate at Stage III.



Figure 55. X-ray Radiograph of a $[0,90,\pm 45]_s$ Laminate at Stage III.

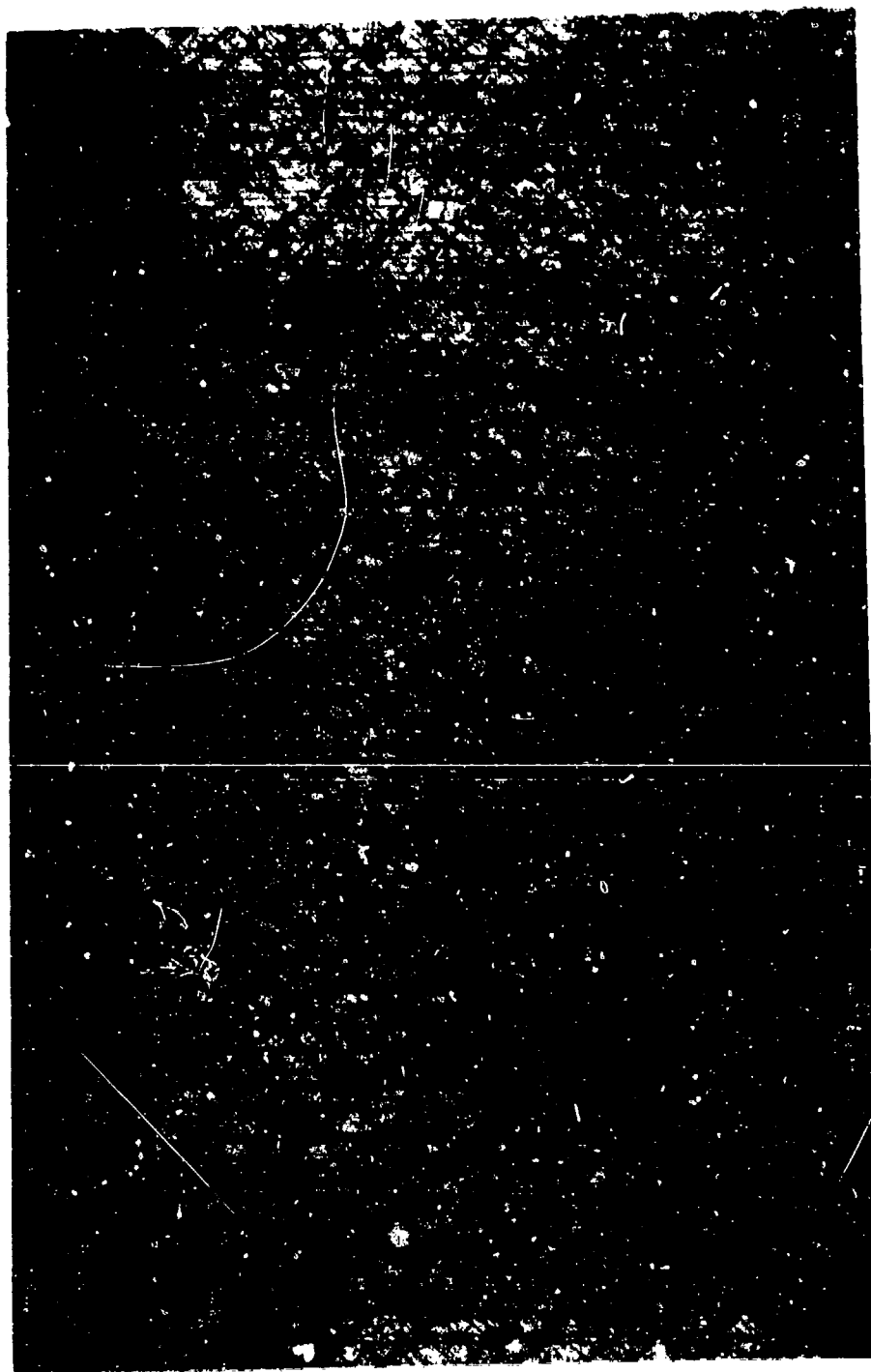
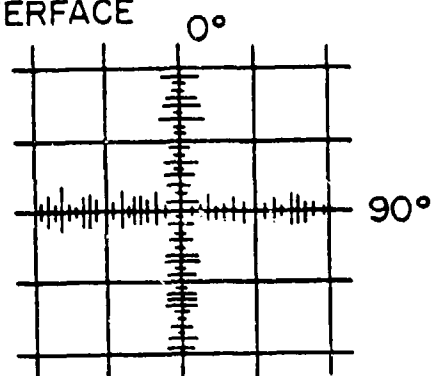
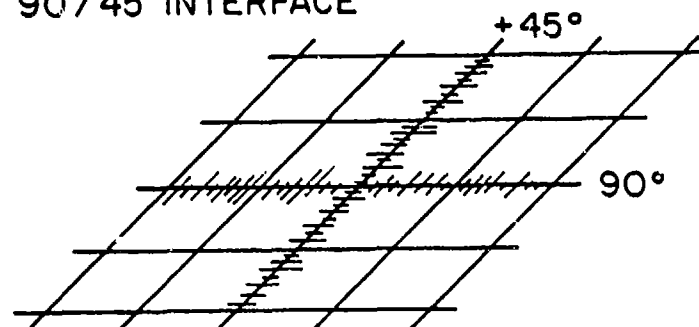


Figure 56. Detail of Figure 55.

0 / 90 INTERFACE



90 / 45 INTERFACE



+45/-45 INTERFACE

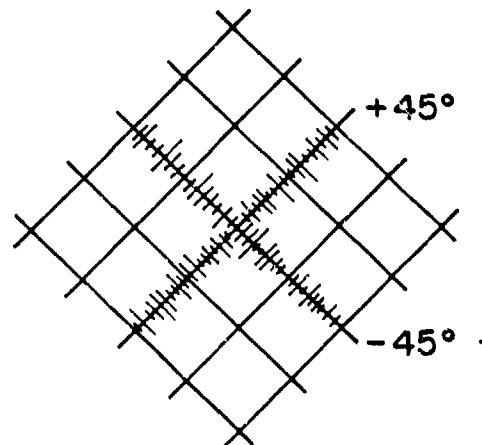


Figure 57. Microcracks in $[0,90,\pm45]_s$ Laminates.

The principal difference among the laminate types is the higher density of microcracks observed in the $[0,90,\pm 45]_S$ case. Close examination of radiographs of $[0,90,\pm 45]_S$ laminates in Stage II reveals the presence of some microcracks. However, the preponderance of these structures appear to develop during Stage III. Their role in global stiffness reduction is not likely to be great. Their maximum potential contribution would be to complete the stiffness reduction normally attributed the saturation condition in the "macrocracks." Their possible effect on fiber fracture is undetermined. If they occur within matrix regions between adjacent fibers in the manner of conventional ply cracks, then no effect would be expected. However, if they occur at the fiber/matrix interface and are thereby distinct from the larger ply cracks, then the local effect on fiber fracture might be significant.

A rapid, large decrease in stiffness in Stage III was observed in every test. A preliminary suspicion was that it might be attributable to fiber fractures. However, this intuition was not supported by fact, as will be discussed in a following section. The predominant damage mechanism in Stage III is the continuation of delamination growth from Stage II. Treating the delamination as a planar crack, O'Brien [62] has shown that the concept of strain energy release rate can be applied successfully to describe the delamination growth rate during fatigue cycling. Following his analysis, the strain energy release rate, G , in a body containing a planar flaw of area A is the difference between the rate of work done, dW/dA , and the rate at which

the elastic strain energy is stored or released, dU/dA , as the flaw area increases,

$$G = \frac{dW}{dA} - \frac{dU}{dA} \quad (6)$$

Expressing U as the product of the strain energy density and the volume of the body, V , then

$$G = V \frac{d(\sigma\epsilon)}{dA} - \frac{V}{2} \frac{d(\sigma\epsilon)}{dA} \quad (7)$$

where σ and ϵ are the laminate longitudinal stress and strain respectively. Substituting Hooke's Law into (7) and noting that in a load-controlled test, σ is constant,

$$G = - \frac{V\epsilon^2}{2} \frac{dE}{dA} \quad (8)$$

Fatigue crack growth laws frequently take the form

$$\frac{dA}{dN} = C (\Delta K)^n \quad (9)$$

where N is the number of cycles, C and n are constants for the material, and ΔK is the stress intensity factor range ($K_{\max} - K_{\min}$). For a cyclic stress ratio of $R=0.1$, $K_{\max} - K_{\min} \approx K_{\max}$ and

$$\frac{dA}{dN} \approx CK_{\max}^n \quad (10)$$

But for plane stress conditions K and G are simply related by

$$\frac{K^2}{E} = G \quad (11)$$

Then the fatigue crack law can be equivalently expressed as

$$\frac{dA}{dN} \approx C' G_{\max}^m \quad (12)$$

Comparing equations (8) and (12) it is seen that dA/dN is an exponential function of ϵ_{\max} . As noted previously, both O'Brien's work and the current results show that delamination area and laminate stiffness are linearly related. Hence

$$\frac{dE}{dN} \propto - \frac{dA}{dN} \quad (13)$$

and

$$\frac{dE}{dN} \propto - \epsilon_{\max}^\beta \quad (14)$$

In load-controlled tests, ϵ_{\max} increases monotonically as shown in Fig. 58. Thus, from (14), the slope of the E versus N curve for a specimen which exhibited edge delamination would be expected to exhibit a progressively more negative slope in the regions where stiffness is controlled by delaminations. This is the observed behavior for the $[0,90,\pm45]_S$ laminates in Stage III (See Fig. 43).

Fiber Fracture

Overview

Discussion of fiber fracture has intentionally been deferred to this point so that the matrix-dominated damage conditions could be developed independently. It would be expected that fiber fracture occurs in each of the damage stages for each laminate type. How it develops, what form it takes when it develops, and whether it is a

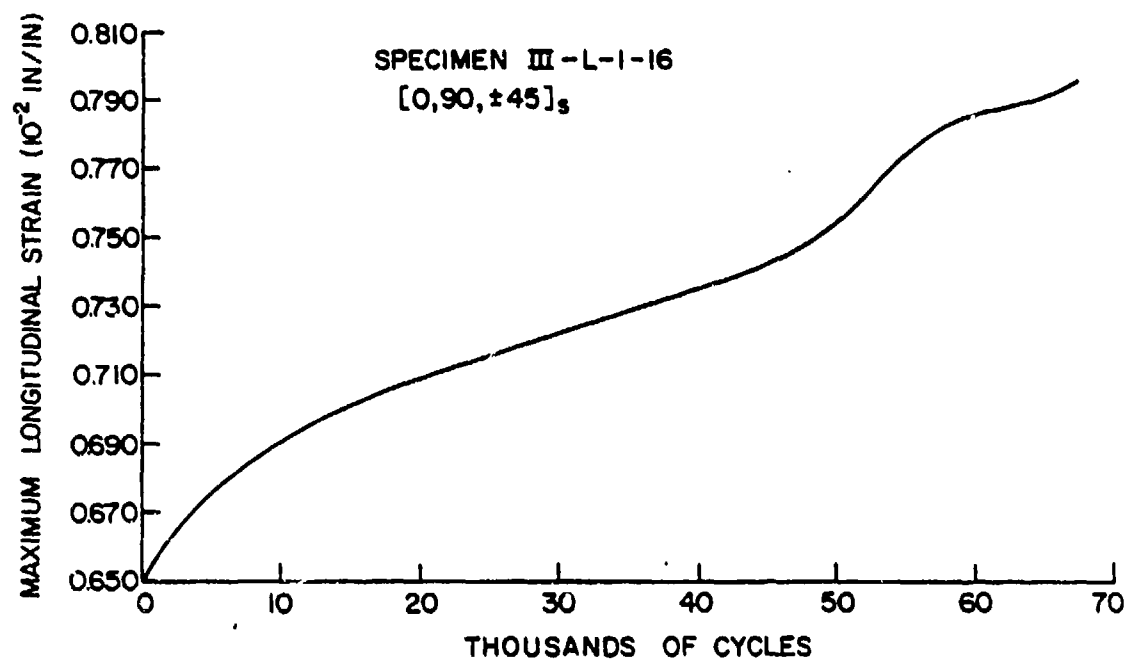


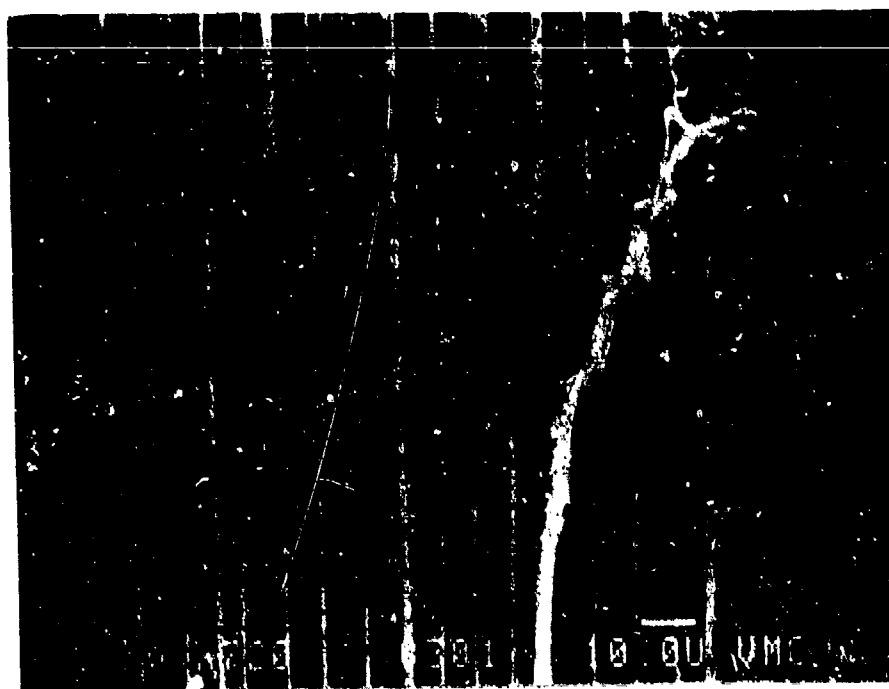
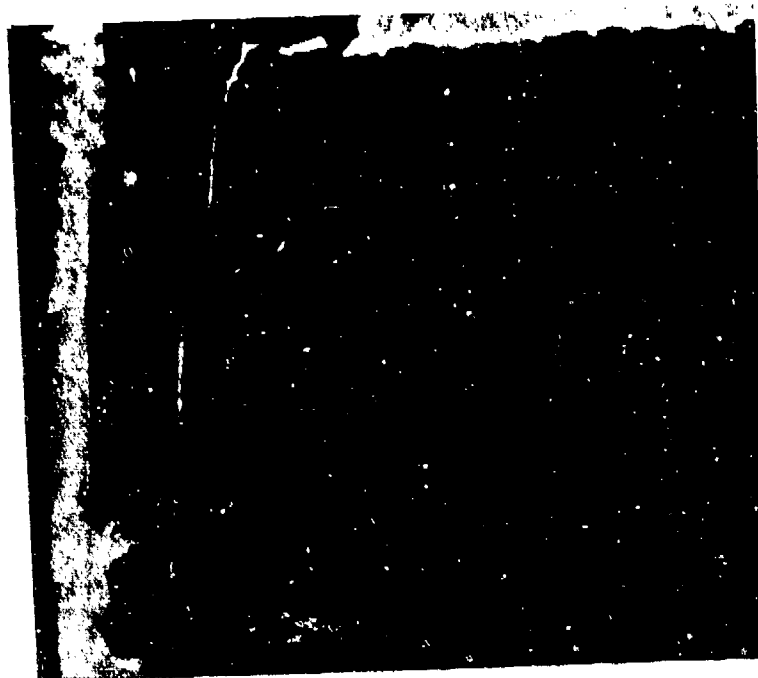
Figure 58. Maximum Longitudinal Strain during Cyclic Loading of a [0,90,±45]_s Laminate.

predominant damage mode in terms of laminate stiffness reduction will be considered in the next sections.

The scanning electron microscope was the principal investigative tool used for this work. Most examinations were performed on coupons cut from deplied laminae. In some cases, portions of edge replicas were examined in the SEM as well for evidence of fiber fracture. The results for each laminate are provided next.

$[0,90_2]_s$ Laminate Type

The initial fiber fracture investigation for this laminate type was motivated by the observation that apparent fiber fractures could be seen in edge replicas taken from fatigue-damaged specimens. Inasmuch as the question of edge involvement in fracture initiation remains unanswered, this was viewed as a fertile area in which to start. By sputter-coating the replicas, they could be viewed in the SEM at higher magnification than was otherwise available. The resolution of detail when viewed in this way was remarkable. Two things were observed. One was that fiber fracture seen at the edge of 0 degree plies frequently occurred in clusters. The spacing between clusters was on the order of the transverse spacing and between clusters there were relatively few fiber breaks. The clusters were not always connected to or even adjacent to transverse cracks. However, when there was a connection it was often a strong one. Figure 59(a) for example shows a transverse crack in the upper portion of the photograph growing aggressively into the 0 degree fibers over a



b)

Figure 59. Fiber Fractures at the Edge of a $[0,90_2]_s$ Laminate.

significant distance from the crack tip. Figure 59(b) shows details of the crack tip incursion into the 0 degree ply. The stairstep pattern is typical of other cracks and other specimens. The crack effectively propagates by probing along the fiber/matrix interface until a fiber weakness is found and exploited, then travels along the interface again as the process is repeated.

Such a mechanism, if operative across the width of the specimen, could account for localized laminate fracture. To examine this possibility, a 1/16 in. (1.6 mm) section was removed from the specimen edge and the edge was repolished and replicated. The result is shown in Fig. 60. The transverse crack is the same one as in Fig. 59. However the crack has not grown into the adjacent 0 degree fibers. Similar results were obtained for other interior cracks. Very few fiber fractures were seen and transverse cracks did not show deep penetration into the 0 degree layer in the interior.

Schulte [63] has shown in fact that edge fiber fracture in this and other graphite/epoxy laminates is substantially diminished at sections only a few fiber diameters from the edge. The effect appears to be extremely localized and may be related to damage developed in the fibers at the edge during cutting and polishing.

Next the 0 degree plies of fatigue-damaged $[0,90_2]_S$ laminates were examined for evidence of interior fiber fractures. Each specimen had been examined by nondestructive means as described previously in this chapter. Coupons measuring approximately 1/4 in. (6 mm) square were cut from each of the deplied 0 degree laminae and examined in the

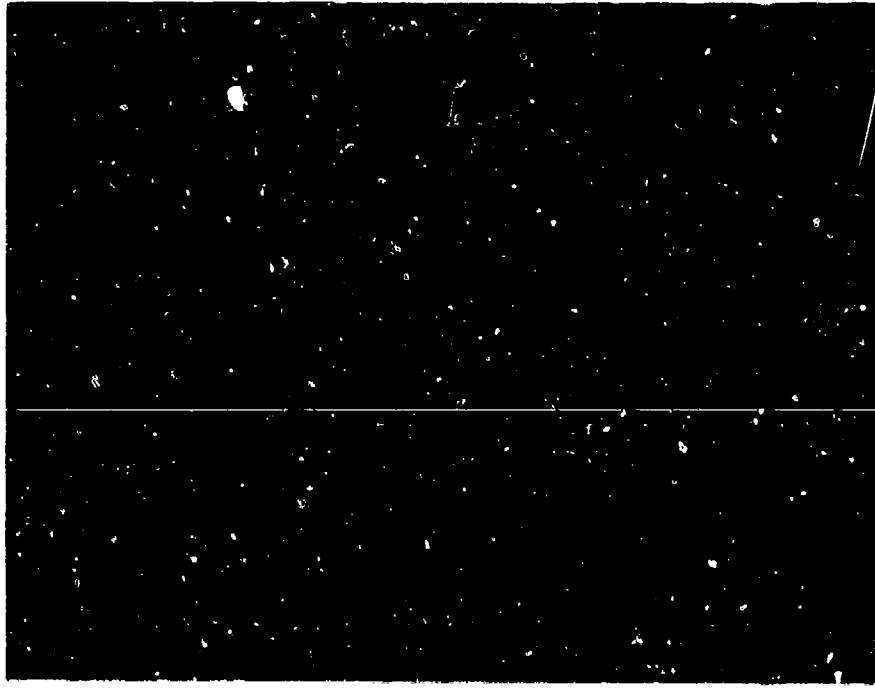


Figure 60. Fiber Fractures at an Interior Section of a $[0,90_2]_s$ Laminate.

scanning electron microscope (SEM). To assure that the process of deplying did not itself produce fiber fractures, a virgin specimen was deplied and examined. Figure 61 shows the result. The fiber arrangement does not show evidence of disturbance either in-plane or out-of-plane. Moreover, fiber fractures are not observed. In fact there were almost no fiber fractures evident in any of the virgin specimen coupons examined. This observation in itself is notable. In discussions of fiber fracture in the literature it is frequently assumed that the laminae in a fabricated plate exhibit a distribution of fiber fracture which are inevitably produced as a result of the fabrication process. O'Brien [99] has shown this to be the case in boron/epoxy laminates by a process of acid leaching the matrix to expose the boron fibers. This does not, however, appear to be true of graphite/epoxy material fabricated in the manner described in Chapter 3. That this fact has not previously been recognized can be attributed to the lack heretofore of a capability for directly observing fibers in laminated plates in situ. The deply technique can now serve that purpose quite adequately.

Deplied 0 degree laminae from fatigue-damaged $[0,90_2]_s$ laminates were examined next. For specimens in Stages I, II, and III of damage development, numerous fiber fractures were observed. These fractures were observed to have a distinct, consistent pattern, shown schematically in Fig. 62. Zones of fiber breaks within horizontal bands were separated by zones in which there were very few fiber breaks. This pattern was repeated along the length of each specimen.

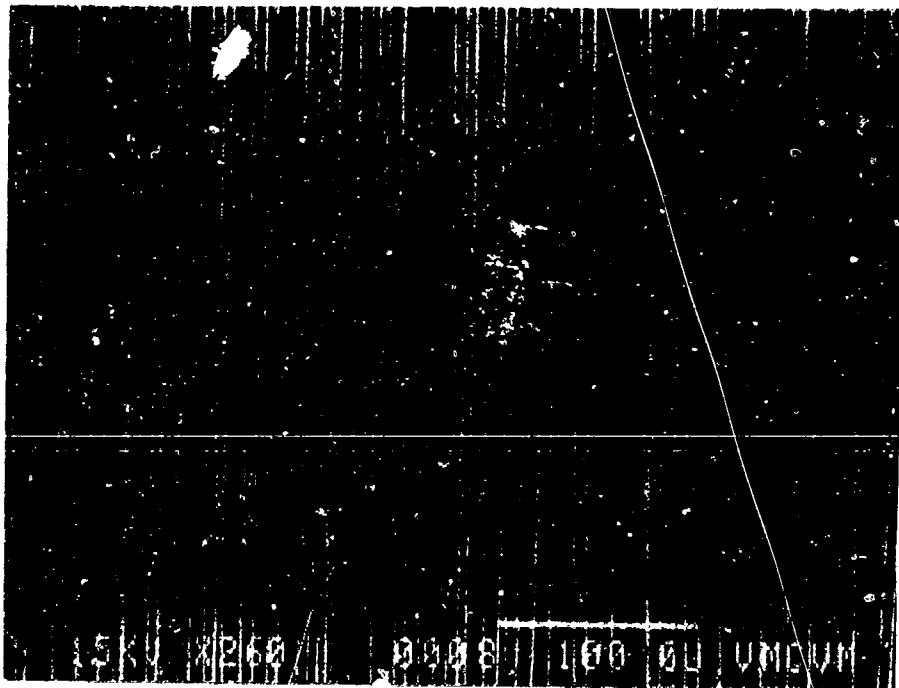
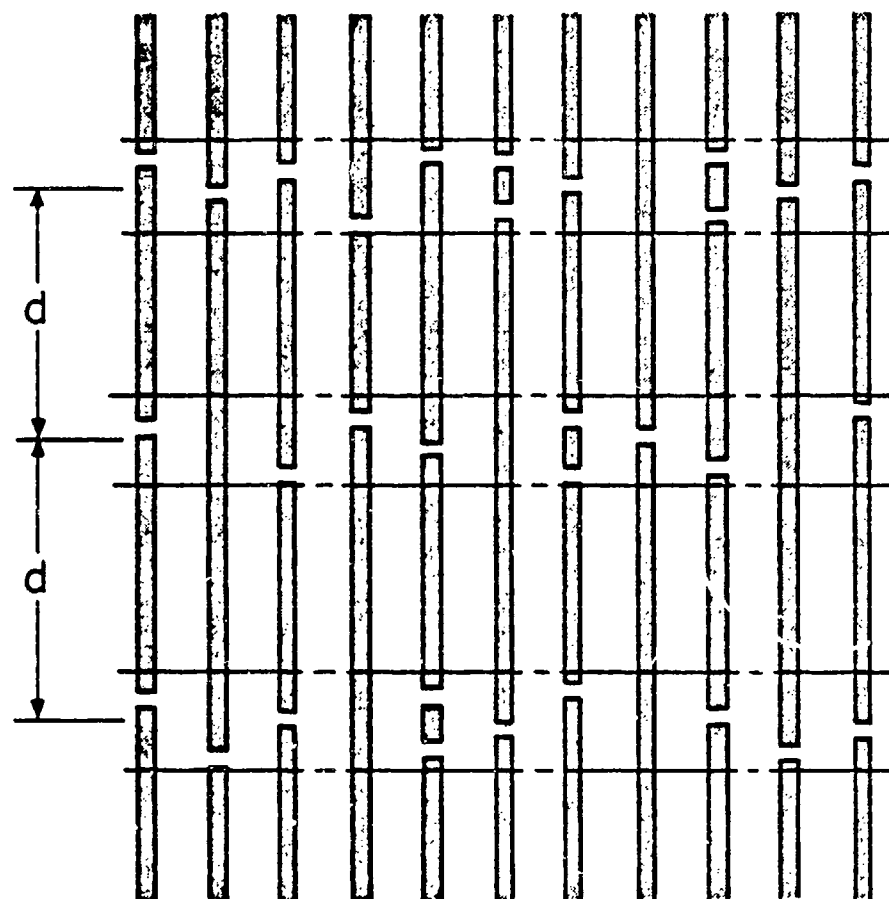


Figure 61. Deplied Virgin $[0,90_2]_S$ Specimen.



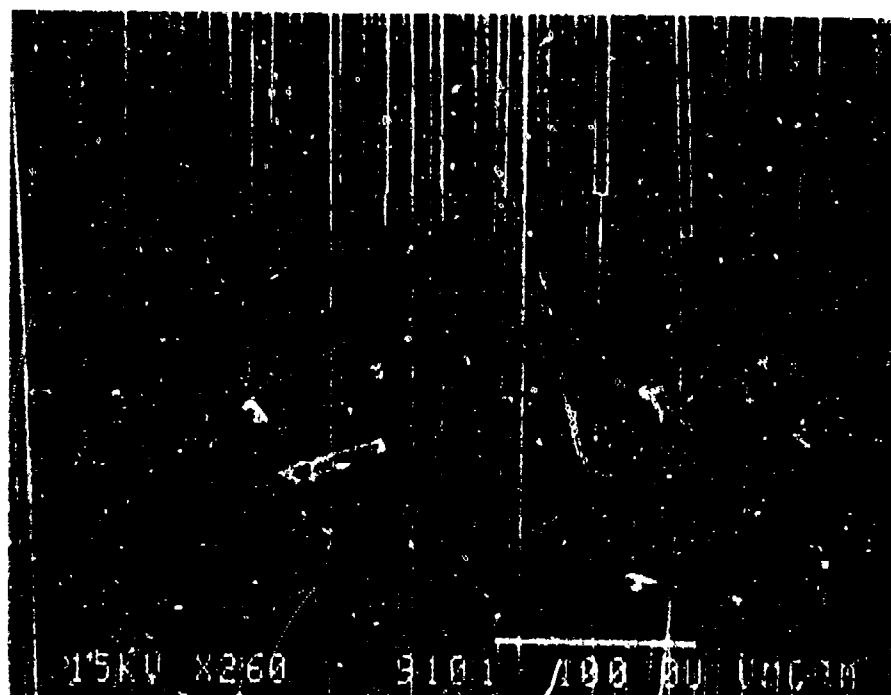
d = ADJACENT PLY CRACK SPACING

Figure 62. Typical Fiber Break Pattern in 0 Degree Plies.

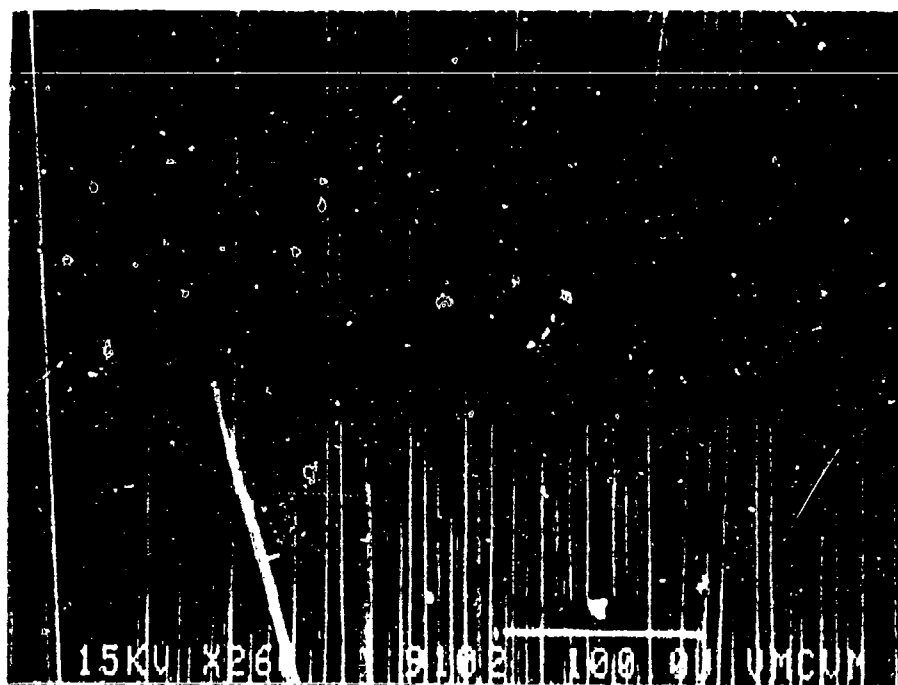
Figure 63(a) shows a region of fiber breaks and Fig. 63(b), an adjacent fracture-free zone taken from a typical specimen. Coupons taken from the edge showed the same pattern as coupons from the center.

The pattern of fiber breaks suggested the involvement of the adjacent transverse cracks whose tips, residing at the 0/90 degree interface, had already been seen to be a fiber fracture initiator at the specimen edge. The question was approached in two ways. First, a series of sequential photographs was taken at 260X magnification of coupons in the SEM and were assembled into a lengthwise strip which included a number of fiber fracture zones. The average distance between the centerlines of these zones was calculated for a series of different coupons in the same specimen. This distance was found to be equal to the crack spacing in the adjacent 90 degree plies, approximately 0.025 in. (0.64 mm).

Second, several specimens were treated with gold chloride prior to being deplied. The gold chloride entered the transverse cracks and left a trace of each crack on the facing 0 degree plies. Under SEM examination, these gold chloride traces were visible and hence the crack locations were known. Figure 64 shows an example. For all specimens examined in this way, the zones of fiber breaks coincided with the locations of gold chloride traces. This was true of specimens in each stage of damage and of coupons taken from various locations in those specimens.



a)



b)

Figure 63. Segregation of Fiber Breaks in the 0 Degree Ply of a $[0,90_2]_s$ Laminate.

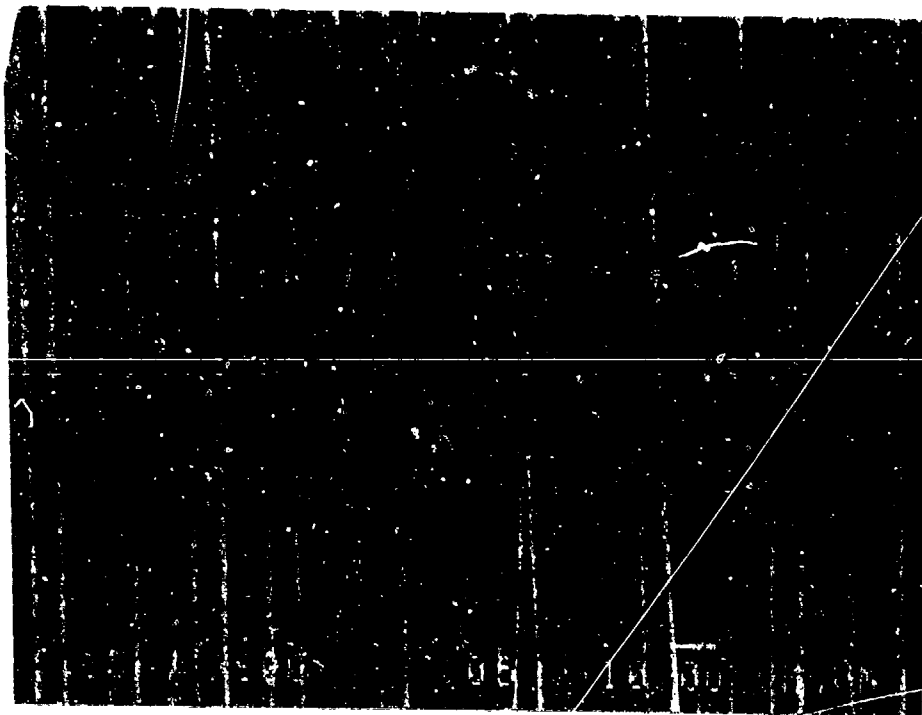


Figure 64. Example of a Gold Chloride Crack Trace.

As a consequence of these corroborative results, it was concluded that the preponderance of fiber fractures in the $[0,90_2]_s$ laminate type which occur during cyclic loading result from the influence of transverse cracks at the 0/90 degree interfaces. This mechanism appears to supersede any tendency of the fibers to break in a random array as determined by the expected strength distribution of single fibers and instead orders the fiber breaks into a more localized configuration than would be predicted from statistical strength arguments.

The role of delamination in the fracture of fibers was also examined for the $[0,90_2]_s$ laminate type. As noted previously, this laminate type delaminates at the 0/90 degree interface across a boundary layer of width approximately equal to the laminate thickness. Coupons were taken from the edge of $[0,90_2]_s$ laminates at the end of Stage I and after edge delaminations had formed. In these coupons, an evident partition between broken and unbroken fibers across each crack track was observed. Over a distance from the edge approximately equal to the laminate thickness, 0.34 in. (8.6 mm), few fiber breaks were observed. However, just beyond this point, fiber breaks were frequent and uniformly distributed across the specimen width. This pattern was repeated in other edge coupons.

Several conclusions can be drawn from these results. First, delamination appears to isolate the 0 degree ply fibers from the transverse cracks and thereby prevents fiber breaks. Second, since crack formation generally precedes delamination in tension-tension

cyclic loading, the mechanisms by which transverse cracks produce fiber fractures appears to require a period in incubation after cracks form before fibers are broken. That is, although the fibers themselves do not exhibit fatigue behavior, the process by which they are in fact broken has a fatigue nature. Third, in light of the previous evidence of fiber fracture at the edge in replicas, it is perhaps necessary now to distinguish mechanisms involving fibers at the edge from those involving fibers near the edge. The former might be termed a "skin" effect, with the term "edge" effect reserved for the latter.

In order to associate the state of fiber fractures in laminates with the three stages of damage previously defined for matrix damage modes, depled 0 degree laminae from specimens in each stage of damage development were examined. The mode of fiber fracture and the banded nature of the fractures were found to be the same for each stage of damage. In order to quantify the fiber fracture state, the total numbers of fiber breaks observed over representative areas were tabulated. Breaks were counted directly from the SEM display screen. An area included by 10 screens width and 10 screens length was chosen as the representative area. At the working magnification of 260X the overall dimensions of the search area were 725 fiber diameters wide and 565 fiber diameters long. The area was sufficiently large that a number of transverse crack traces were included. The total number of fiber breaks was tabulated for several representative areas in coupons taken from the edge and center of both 0 degree plies in each laminate. The results are shown in Fig. 65. The average number of fiber

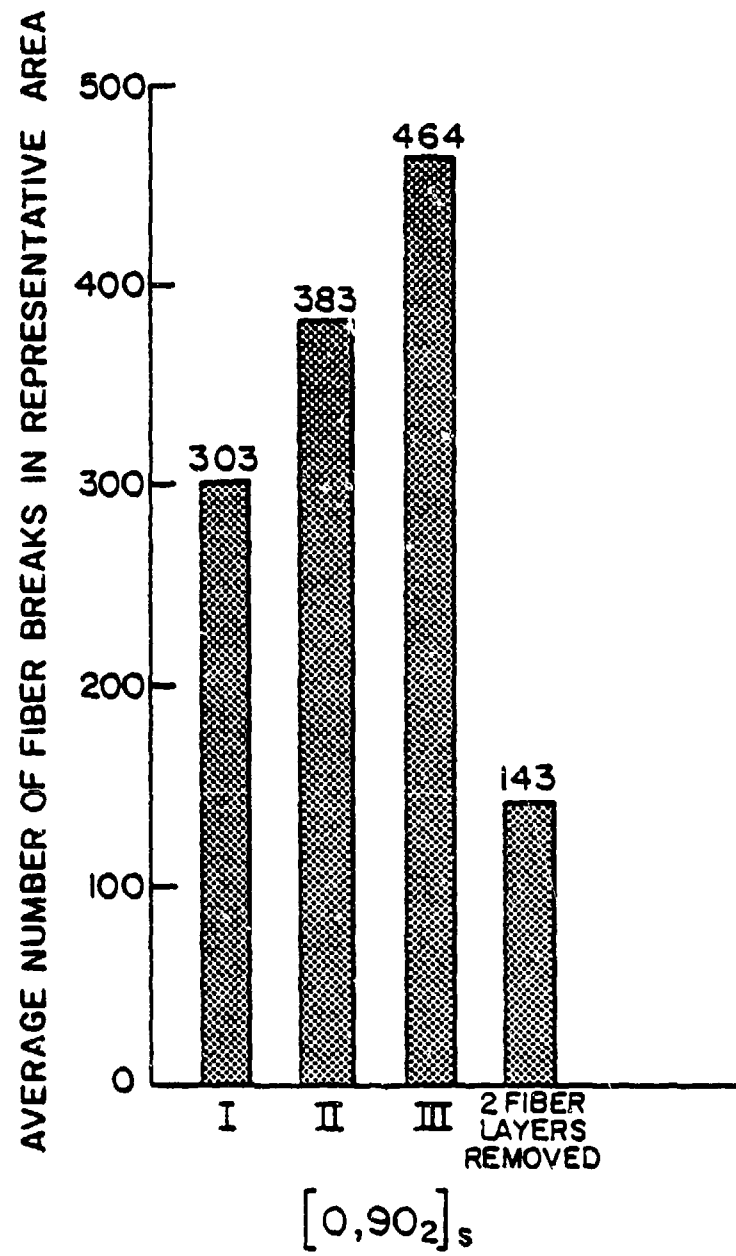


Figure 65. Total Fiber Breaks in $[0,90_2]_s$ Laminates.

fractures is seen to increase with advancing stages of damage, suggesting that fiber fracture is a progressive fatigue process. The fourth column in Fig. 65 represents the total number of fiber fractures in a Stage III specimen with two fiber layers removed. This was accomplished by twice applying adhesive tape to the top fiber layer of a coupon and gently lifting away the adhering fibers. The underlying fibers remained relatively undisturbed.

By comparison with the fiber fractures in the outermost layer, the number of fiber fractures two layers removed from the interface is 70 percent lower. Successive removal of fiber layers shows a continuation of the trend. Fibers only slightly removed from the interface are effectively insulated from the invasive action of the transverse cracks. Moreover, the fractures which are observed there lie within bands somewhat broader than those observed for fiber breaks at the interface. The combination of these effects is summarized schematically in Fig. 66. The influence of the transverse cracks is intense and localized at the interface while it broadens and loses intensity rapidly in the 0 degree ply with distance away from the interface.

A second quantity of interest was the frequency of occurrence of multiple adjacent fiber breaks in these specimens as a function of damage stage. A number of laminate fracture models directly or indirectly predict that failure occurs when a critical number of adjacent fiber fractures occur to form an unstable "crack."

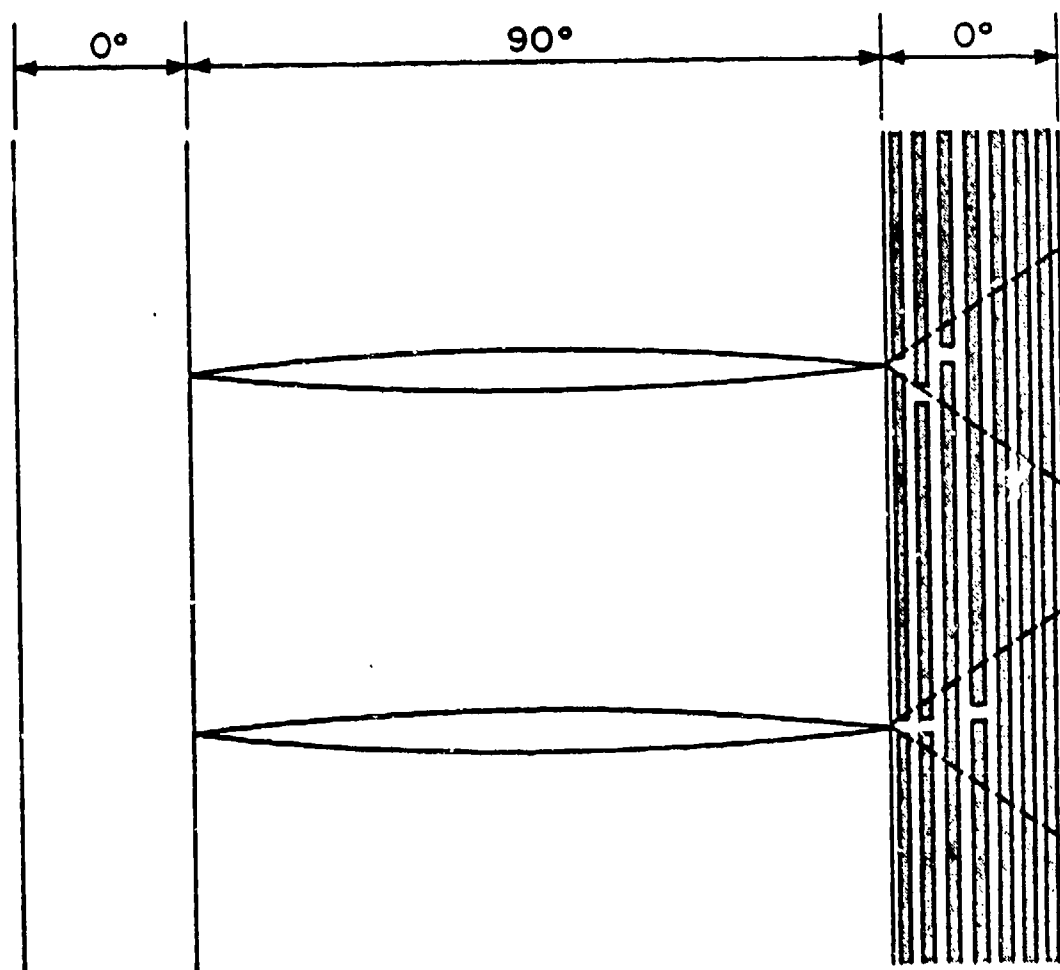


Figure 66. Fan of Influence of Cracks on Fiber Fractures.

To facilitate the categorization of multiple adjacent fiber fractures, some ad hoc definitions were required. A singlet was taken to be a single fiber break bounded by two unbroken fibers; a doublet was defined to be two adjacent broken fibers in which the breaks were separated by a length not greater than five fiber diameters; a triplet was defined as three adjacent fiber breaks in which none of the breaks was separated from the adjacent break by a distance greater than five fiber diameters. Quadruplets and higher order "multiplets" were defined in a similar way. The choice of a five fiber diameter lengthwise separation as a multiplet criterion was arbitrary but was applied uniformly to all specimens. The multiplet distribution was counted at the same time and using the same representative area as that used for the total fiber fractures. The results are shown in Fig. 67. It is seen that for increasing stages of damage the distribution shifts slightly but unmistakably from singlets toward higher order multi-plets. Such a result appears to be consistent with predictions of Tamuzs [30] and Batdorf [26] even though their models are based on static loading of unidirectional laminae. If failure is to be preceded by the development of metastable multi-plets of fiber fractures in the critical load-bearing 0 degree plies and if fiber fractures develop gradually as these results suggest, then such a shift must be anticipated.

The last column of Fig. 67 shows the multiplet distribution for a Stage III specimen at a distance of two fiber layers from the interface. The distribution shows a return to a form characteristic of

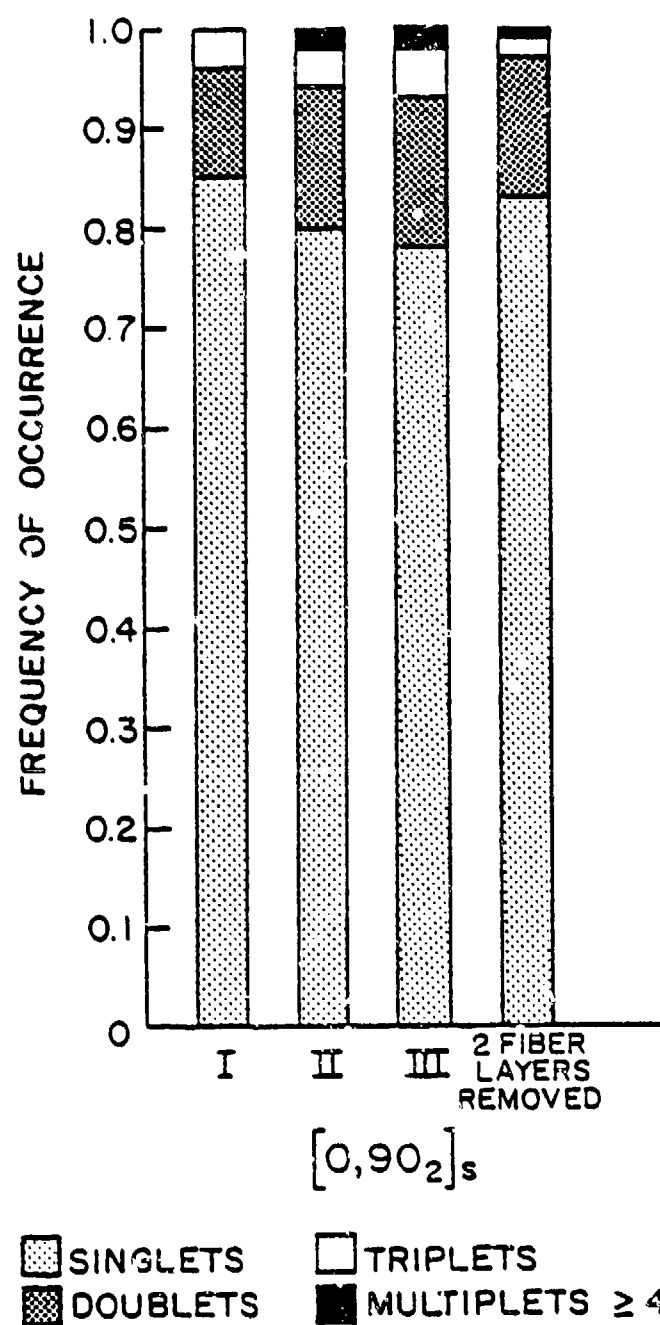


Figure 67. Distribution of Multiplets in $[0,90_2]_s$ Laminates.

earlier damage stages. Coupled with the lower total fiber fracture condition at this level, it appears that fibers located away from the interface are sufficiently insulated from transverse cracks that they are in essence "younger" than those at the interface. If any three-dimensionality in the unstable crack models exist, then through-thickness development of fiber fractures (a relatively slow affair in light of these results) may be the critical factor in the initiation of laminate failure.

Can the extent and distribution of fiber fractures observed for the $[0,90_2]_s$ laminate type account for a significant portion of the observed stiffness reduction? The answer appears to be no based on an analysis proposed by Russel [98,99] in which the broken fibers are modeled as slender, prolate spheroids imbedded in an elastic matrix in dilute concentrations. Although the reality of the actual condition is taxed by this latter assumption, there are not, to the author's knowledge, greatly different results obtained from a better model. The dilute assumption should provide an upper bound on the actual stiffness reduction. For a graphite/epoxy lamina, the analysis based on this model predicts that for a one percent stiffness reduction to occur, every fiber in the ply would have to be broken every 0.03 in. (0.7 mm). Although this is on the order of observed fiber break intervals (0.025 in.)(0.6 mm) for the $[0,90_2]_s$ laminate type, the number of fiber breaks observed in even the most damaged case does not approach the number required. For example, for a one percent stiffness reduction in the $[0,90_2]_s$ laminate type, this would required more

than 6 times as many fiber breaks in a representative area as the minimum number observed at the interface for any specimen. Moreover that pattern would have to be repeated at every fiber layer away from the interface, also contrary to the observed behavior.

On this basis it is concluded that fiber fracture has a negligible role in global stiffness reduction for the $[0,90_2]_s$ laminate type. This does not of course diminish its role in local stiffness and strength reduction which may be critical in the initiation of fracture.

$[0,\pm 45]_s$ Laminate Type

Each ply in this laminate type was examined for fiber fracture since the ± 45 degree plies provide a considerable strength and stiffness contribution. Proceeding in the same manner as for $[0,90_2]_s$ specimens, coupons were cut from various locations in each lamina of depled, fatigue-damaged specimens for SEM examination. These observations, made for specimens in each damage stage, yielded several interesting results. First, the number of fiber fractures at each damage stage was considerably smaller than observed for the $[0,90_2]_s$ counterparts, approximately one-quarter as many on the average. Second, the fiber breaks which were observed were segregated into zones separated by zones of few fiber breaks. The mean distance between these zones was equal to the spacing of cracks in adjacent cracks. This is the same result as found in the $[0,90_2]_s$ laminate type, and applied to the 0 degree, +45 degree, and -45 degree plies

equally. That is, the fiber fracture zones in the 0 degree plies in Stage III had a mean separation of approximately 0.015 in. (0.38 mm), the CDS spacing of the cracks in the adjacent +45 degree plies; the fiber fracture zones in the +45 degree plies at the +45/-45 degree interface had a mean spacing of 0.029 in. (0.73 mm), the CDS spacing of the -45 degree plies; and the -45 degree ply fiber breaks were separated by a distance approximately the same as those in the 0 degree plies since the +45 degree ply cracks act simultaneously on these plies.

Additional evidence of the crack involvement in fiber fracture was provided by the fact that the line of fiber breaks in a given ply was parallel to the crack direction in the adjacent plies: 0 degree ply fiber breaks fell along parallel, +45 degree diagonal lines, +45 degree ply fiber fractures fell along -45 degree diagonal lines, and -45 degree ply fiber fractures fell along +45 degree diagonal lines. The banded nature of fiber breaks was observed at every stage of damage and at every location in the plies.

Perhaps the most interesting result was provided by examining the mode of individual fiber fractures. In the $[0,90_2]_s$ laminate type, fiber fracture exhibited a cleavage character with the fracture plane normal to the fiber axis, as in Fig. 63(a). The same appearance was observed for the 0 degree ply fibers in the $[0,\pm 45]_s$ laminate type. However, the fracture appearance of fiber breaks in the +45 degree and -45 degree plies was quite different. Figure 68 shows an example taken from a +45 degree ply. The fractures have a shear mode or mixed

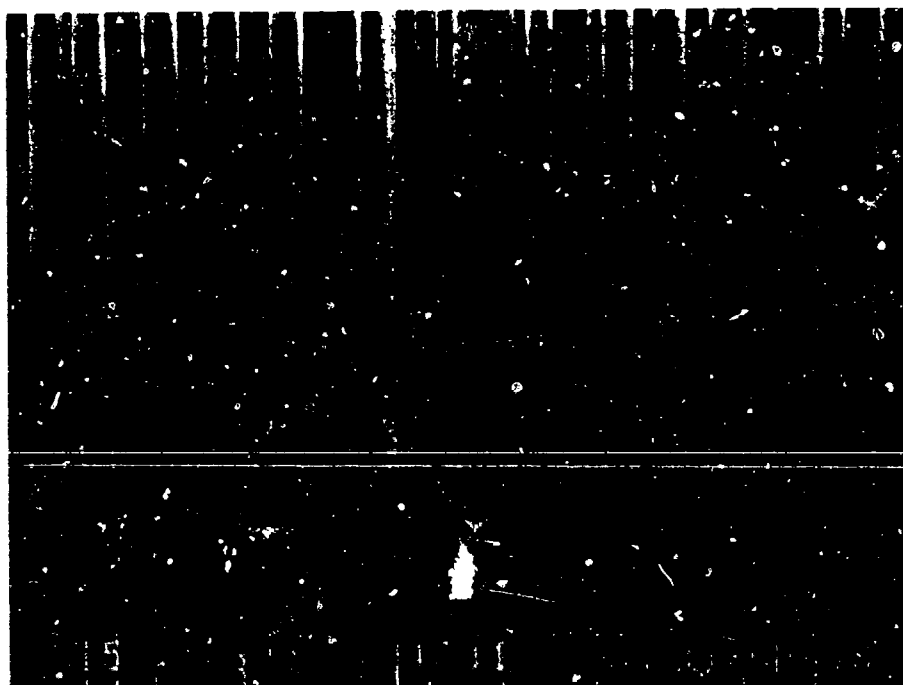


Figure 68. Mixed Mode of Fiber Fracture in $[0, \pm 45]_S$ Laminates.

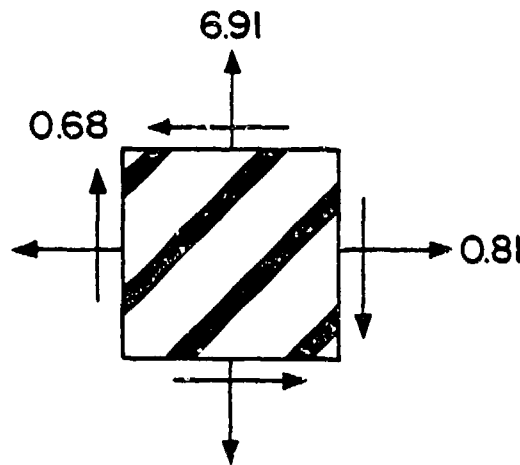
mode appearance. With few exceptions, the fiber fractures observed in off-axis plies in $[0, \pm 45]_s$ laminates at every stage of damage exhibited this apparent shearing influence.

An explanation is provided by considering the stress state in these plies under tensile loading. For an applied uniaxial load of 1000 lbf (4.45kN) the stresses in the inner plies are shown in Fig. 69. In both the +45 degree and -45 degree plies the normal and shear stresses acting on the fibers in the material coordinate system are approximately equal. This differs significantly from the stresses acting on the 0 degree ply fibers in which the shear component of stress is less than one-twentieth of the normal stress. The influence of a substantial shear stress on the fracture mode in graphite fibers is also increased by the highly anisotropic structure of these fibers in which transverse properties are typically much lower than axial properties.

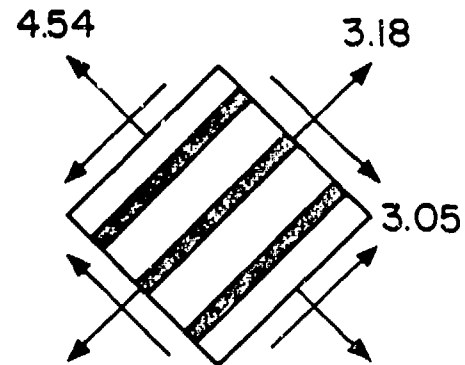
The angle of fracture surface to the fiber axis varied. However, the majority of breaks were observed to be at an angle of approximately 45 degrees to the fiber direction.

Schulte [63] has proposed a model by which fiber fractures having this appearance might be produced by the action of in-plane cracks. In this model fiber fracture occurs in shear by transfiber growth of the crack along a path generally parallel to fibers in the manner of Fig. 70. Schulte has observed such behavior by longitudinal cracking in some laminates of graphite/epoxy. To examine this mechanism for the $[0, \pm 45]_s$ laminate type, fiber fractures in the +45 degree plies at

+45 DEGREE PLY STRESSES (KSI)

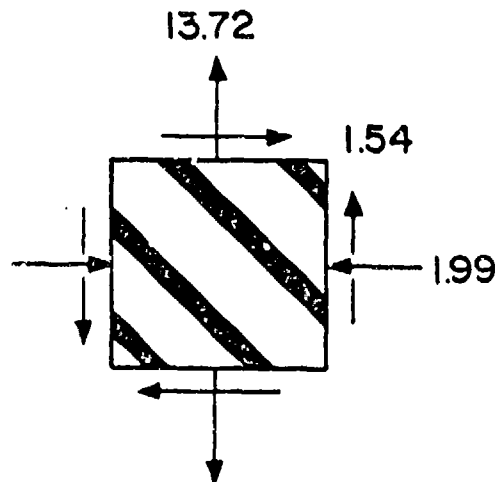


BODY COORDINATES

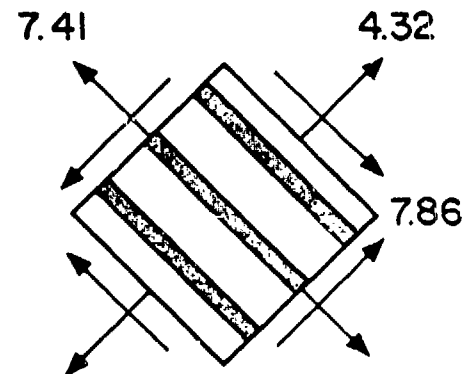


MATERIAL COORDINATES

-45 DEGREE PLY STRESSES (KSI)



BODY COORDINATES



MATERIAL COORDINATES

Figure 69. In-plane Stresses for a $[0, +45]_s$ Laminate Loaded to 1000 lbf. in Uniaxial Tension.

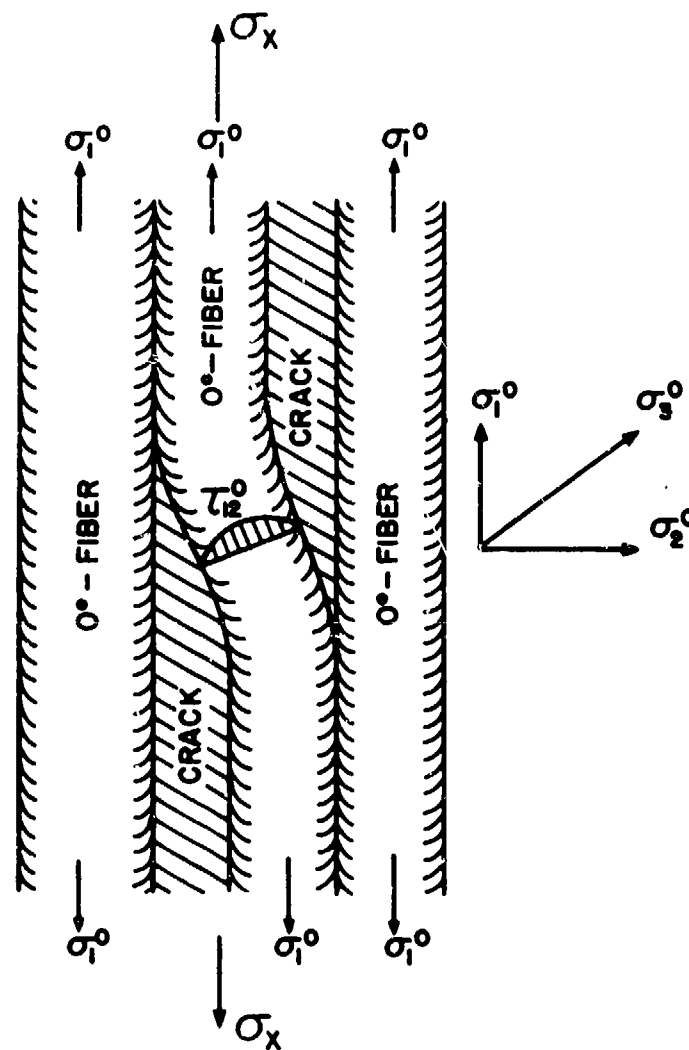


Figure 70. Model of Fiber Fracture by In-plane Cracks
(from Reference 63).

both the 0/+45 degree interface and the +45/-45 degree interface were considered. At the +45/-45 degree interface, mixed mode fiber fractures were observed. At the 0/+45 interface, no fiber fractures were found. The plies examined had numerous in-plane cracks which typically extend completely through the ply. If these cracks produce fiber fractures in their own plane, then the effect should be observed at both interfaces. That it was not suggests that this mechanism is not active in the $[0, \pm 45]_S$ laminate.

In summary of the $[0, \pm 45]_S$ laminate fiber fracture results, it is concluded that both the location and locus of fiber breaks in each ply is determined almost entirely by the action of cracks in adjacent plies. However, the mode of the fracture can be either normal or mixed mode determined primarily by the in-plane stress state of the ply in which they occur. Finally, the average number of fiber fractures observed in the 0 degree plies of this laminate was significantly smaller than observed in the $[0, 90_2]_S$ laminate.

$[0, 90, \pm 45]_S$ Laminate

The 0 degree and ± 45 degree plies were examined for fiber fracture in specimens representing each stage of damage. The most surprising result was also the most obvious--there were almost no fiber breaks in any ply at any stage of damage for this laminate type. Figure 71 shows the results of counting fiber breaks over a number of representative areas having the same dimensions as those used in discussing the results from the $[0, 90_2]_S$ case. The results

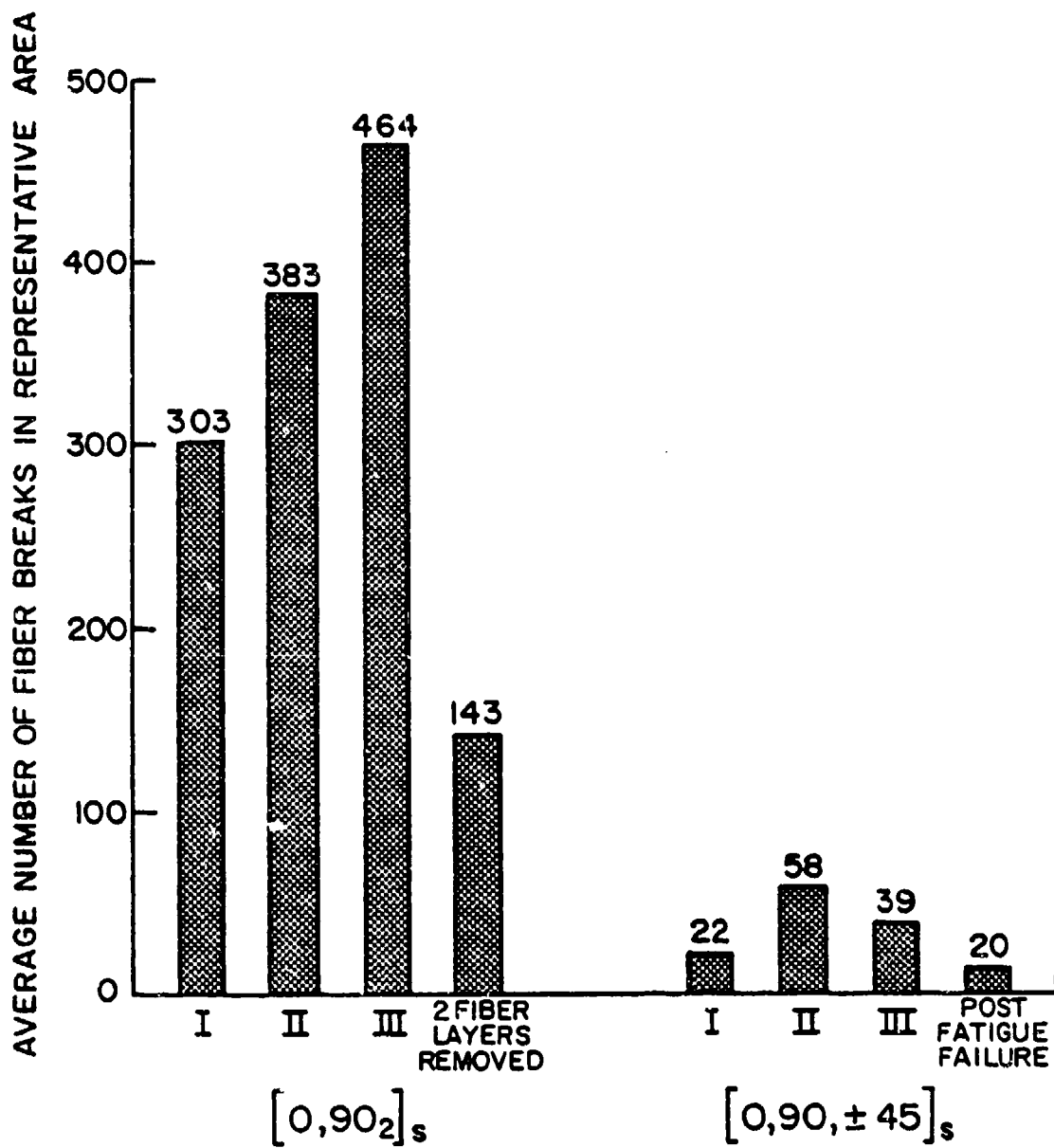


Figure 71. Total Fiber Fractures in $[0,90,\pm 45]_s$ Laminates.

from that laminate are repeated for comparison. The numbers are different by an order of magnitude. The scatter in this type of measurement is on the order of the total number of breaks in the $[0,90,\pm45]_S$ case and consequently no clear trend related to damage development stages is apparent. However, the occurrence of multiple adjacent fiber breaks does exhibit a familiar trend as shown in Fig. 72. With increasing damage, the multiplet distribution shifts slightly from singlets to doublets. For comparison, the $[0,90]_S$ multiplet results are repeated. It can be seen that the proportion of singlets in the $[0,90,\pm45]_S$ laminate is uniformly higher and the occurrence of triplets and higher order multiplets is almost nonexistent.

The fourth columns of the $[0,90,\pm45]_S$ results in Fig. 72 are results for a coupon taken from the center of a specimen which had failed after 263,000 cycles of tension-tension cyclic loading. The specimen was depled after failure and an undisturbed area approximately 1 1/2 in. (38 mm) from the fracture site. The multiplet distribution for this specimen appears to be an extension of the trend indicated in the progressively more damaged specimens. It is noted that even in the failed condition, no multiplets of order greater than three were observed, suggesting that if laminate fracture is initiated by the development of an unstable multiplet of fiber fractures, then that number may be as small as four for this laminate type.

Fiber fracture mode in the $[0,90,\pm45]_S$ laminate followed precisely the same model as the other laminates discussed: normal mode in the 0 degree plies, mixed mode in the +45 degree plies. An example of the

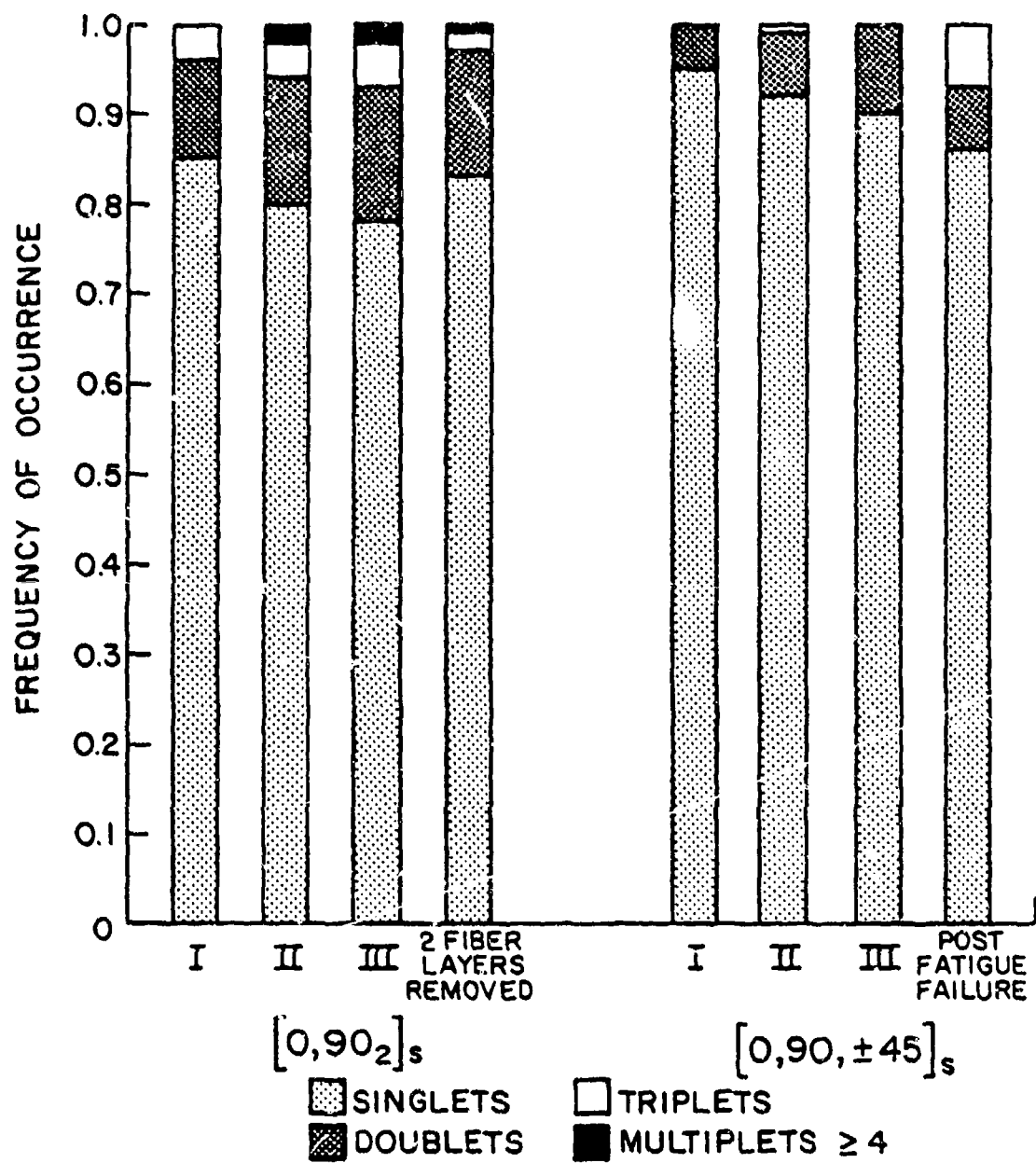


Figure 72. Distribution of Multiplets in $[0,90,\pm45]_s$ Laminates.

mixed mode appearance of two doublet fiber fractures in a +45 degree ply adjacent to a 90 degree ply is shown in Fig. 73.

The results then for the $[0,90,\pm45]_S$ and the other two laminate types consistently and convincingly implicate off-axis ply cracks in the fracture of fibers in adjacent plies. The global result of this local process is the development of a banded structure of fiber fractures separated by regions in which fibers are unbroken. With increasing stages of damage the fiber fracture distribution moves toward multiplets of adjacent breaks. The influence of adjacent cracks on fiber fracture locations and locus does not extend to determining the mode of fracture which appears to depend instead on the state of stress in the plane of the fiber.

Finally, there are relatively few fiber fractures to be seen in any of the laminate types examined even at advanced stages of damage. The density of breaks observed is not sufficient to predict a significant effect on laminate stiffness.

The fiber fracture density, although small, may be significant in laminate failure. Is there a way to anticipate the near-absence of fiber fractures in the $[0,90,\pm45]_S$ laminates or the tenfold larger incidence of fiber fractures in the $[0,90_2]_S$ laminate? Table VI provides some insight into a possible answer. It shows for all three laminates the stresses in the 0 degree plies at static failure and at the cyclic stress amplitudes used in this study. Of particular interest are stresses in the 0 degree plies at the average measured laminate static strength with the off-axis ply elastic moduli, E_2 and



Figure 73. Fiber Fracture Mode in $[0,90,+45]_s$ Laminates.

Table 6. Comparison of Laminate Strength Margins

	$[0,90,\pm45]_s$ (ksi)	$[0,90_2]_s$ (ksi)	$[0,\pm45]_s$ (ksi)
Laminate Stress at Static Failure (Measured)	74	81	96
0 Degree Ply Stress at Static Failure with--			
• No Plies Cracked	187	206	220
• Off-Axis Plies 50% Discounted	<u>203</u>	<u>224</u>	<u>245</u>
• Off-Axis Plies Completely Discounted	223	244	280
Laminate Stress at Maximum Cyclic Load (Calculated)	46	57	67
0 Degree Ply Stress at Maximum Cyclic Load--			
• No Plies Cracked	116	147	164
• Off-Axis Plies Fully Cracked	142	<u>175</u>	<u>209</u>
• Off-Axis Plies Cracked and Fully Delaminated	<u>188</u>	Does not Delaminate	Does not Delaminate
0 Degree Strength Margin after Full Damage Develops	7.1%	21.6%	14.7%

G_{12} , discounted by 50 percent. This assumes that the laminate effectively reaches the end of Stage I damage development at static failure. The choice of a 50 percent discount is that used previously in matching measured and predicted stiffness reductions at the end of Stage I. The 0 degree ply stress calculated in this way can then be considered the critical stress for last ply failure in the laminate.

For comparison, the 0 degree ply stress in a laminate subjected to cyclic loading is calculated based on the maximum stress amplitude used for each laminate. Under the condition of complete ply cracking and delamination (if the latter occurs) the maximum 0 degree ply stress under cyclic loading is calculated. When this operating stress is compared to the critical stress (both quantities are underlined in the table) a "strength margin" can be computed. This margin, by which the 0 degree ply strength exceeds the 0 degree ply stress after the full development of matrix damage, provide a basis for anticipating the role of damage other than ply cracking and delamination in producing laminate failure. The greater the strength margin, the greater the role of other modes in bringing about laminate failure.

From the results of this investigation, fiber fracture is this other principal damage mode. Based on Table VI, the $[0,90,\pm 45]_S$ laminate has the lowest strength margin and consequently requires the lowest contribution of fiber fracture in order to produce the requisite 0 degree ply stress increase to produce laminate failure. The $[0,\pm 45]_S$ laminate requires a higher fiber fracture contribution for laminate failure and the $[0,90_2]_S$ laminate requires the greatest fiber

fracture contribution. This ordering is precisely the ordering of laminates according to the observed density of fiber fractures: fewest in the $[0,90,\pm45]_S$ laminates, followed by $[0,\pm45]_S$ laminates, with the most in the $[0,90_2]_S$ laminates. Hence, perhaps the paucity of fiber fractures in the $[0,90,\pm45]_S$ laminates should not have been surprising. It would be unlikely that a large number would exist globally when only a 7 percent broken fiber density at any net section would be sufficient in theory for laminate failure. On the other hand, a relatively large proportion of fibers must be broken in the $[0,90_2]_S$ laminate to produce the required 0 degree ply stress increase. If fiber breaks develop stably with increasing cycles as suggested by the results presented previously, then the strength margin at the operating stress used provided sufficient opportunity for a significant number of breaks to occur prior to laminate fracture.

It should be noted that the calculation of a strength margin involves assumptions regarding the extent of matrix damage at static failure as well as at fatigue failure. By inspection of Table VI the value of the strength margin is sensitive to these assumptions. However, when an assumed damage condition is applied uniformly to each of the laminate types, the relative relationships of the resulting strength margin values are unchanged. Hence the real value of the concept of strength margin in the context of fiber fracture studies is in assessing the relative role of fiber breaks in the failure of different laminates.

V. CONCLUSIONS AND SUMMARY

The purpose of this investigation was to establish the character and sequence of development of advanced damage resulting from tension-tension cyclic loading of graphite/epoxy laminates. Advanced damage development was defined to be that damage produced by the part of the loading history which is applied subsequent to the development of the characteristic damage state for matrix cracking. Three laminate types, $[0,90_2]_s$, $[0,\pm45]_s$, and $[0,90,\pm45]_s$, chosen to represent a broad range of intralaminar and interlaminar stress conditions, were subjected to tensile fatigue loading. Post-fatigue analysis was accomplished by both nondestructive and destructive (microscopic) means. The dynamic secant modulus was computed continuously during the course of each cyclic test, and changes in this quantity served as a damage analogue.

It was found that for each laminate type and cyclic load level, the relationship between secant modulus and number of cycles was repeatable and unique to that laminate. Each of these characteristic relationships exhibited three distinct stages. These stages of stiffness reduction were used as a basis for ordering and interpreting the damage which caused them. Damage which developed during the first stage for each laminate consisted of the development of off-axis cracks which ultimately formed a saturated pattern of cracks in each ply, a well-defined and predictable condition for matrix cracking which has been termed the characteristic damage state. The subsequent two stages were related to advanced damage. In the $[0,90_2]_s$ laminate,

this advanced damage took the form of longitudinal cracking and interior delamination; the latter was related to the development of tensile interlaminar normal stress at the intersections of longitudinal and transverse cracks at the 0/90 degree interfaces. In the Stage III damage condition, the $[0,90_2]_s$ laminates exhibited longitudinal splitting, a condition in which small volumes of 0 degree fibers are liberated from both in-plane and interlaminar constraint as the result of the coalescence of longitudinal cracks and their associated delaminations, fracture at a net section within that volume, and separation from the laminate over a considerable lengthwise distance. The result is an abrupt and significant loss of laminate stiffness and a redistribution of stress into the remaining 0 degree fibers.

For the $[0,\pm45]_s$ laminate, Stage II was notable for the lack of any delamination development. Except for the completion of off-axis cracking, no matrix damage was observed and little measurable stiffness reduction occurred. Stage III damage in the $[0,\pm45]_s$ laminate type was the most elusive of the three laminates examined. There was some evidence that Stage III is characterized by the development of localized microcracks in the off-axis plies which may contribute to an observed stiffness reduction of between 0.5 and 1.0 percent which occurs as a very rapid punctuation to the nearly horizontal Stage II portion of the stiffness versus cycles curve. But Stage III was not always observed prior to laminate failure. The sensitivity of the $[0,\pm45]_s$ laminate to any asymmetry of loading and to the presence of

stress concentrations required that many specimens be tested to yield a sufficient representation of damage conditions for analysis. Often a specimen would exhibit quite predictable Stage I behavior and then fail without warning; or pass through both Stage I and Stage II normally only to fail abruptly without evidence of Stage III development. Clearly there are competing processes in operation during tension-tension fatigue loading of this laminate: those which produce global damage and perhaps forestall the initiation of fracture (a prima facie localization); and those which proceed in parallel, having a local nature throughout but variable in the interval required to achieve predominance. The importance of local mechanisms in the fatigue failure of $[0, \pm 45]_S$ laminates may owe to the absence of competing global mechanisms, particularly delaminations. When the material is unable to relax local stress concentrations by diffusing it through the creation of local damage, then the number of possible fracture initiation sites and hence the likelihood of fracture is increased. In this regard, the $[0, \pm 45]_S$ laminate recommends itself as a potentially useful geometry for the study of fracture initiation.

For the $[0, 90, \pm 45]_S$ laminate, Stage II was dominated by the development of edge delaminations. A linear relationship between stiffness reduction and delamination length was predicted on the basis of a rule of mixtures analysis and was confirmed experimentally by measuring the actual delamination areas at each interface of depled specimens. The deply technique served, as well, to corroborate the

assignment of delaminations to the interface in which they lay from microscopic examination of stereo X-ray radiographs.

Stage III damage in $[0,90,\pm45]_s$ laminates was found to be a continuation of edge delamination growth and the development of a dense localized microcrack condition. These microcracks in each ply were seen to be clustered along cracks in adjacent plies. The proposed mechanism for the development of such cracks was based upon the existence of tensile stress components at the tips of these cracks. The rate of stiffness reduction in Stage III increased rapidly. Such an increase was shown to be predictable in a load-controlled test for any laminate subject to delamination growth, by modeling the delamination as a planar crack and applying Griffith-type crack growth concepts.

Fiber fracture was studied in the same three laminates concurrently with the study of matrix damage modes using scanning electron microscopy of deplied laminae. A number of conclusions were drawn from these observations. First, deplied virgin specimens of these laminates exhibited almost no fiber breaks, suggesting that the density of initial fiber fractures sometimes ascribed to the fabrication process may be overstated in graphite/epoxy laminates. Second, the fiber breaks which were observed to occur in each of the laminates at each stage of damage development were found to be not randomly distributed as would be predicted from unidirectional results but were arrayed in a banded structure. This structure, in which zones of fiber breaks are separated by zones in which breaks are not observed, was found to be closely associated with the spacing of cracks in the

ply adjacent to the plane of the fibers. This relationship was confirmed for fiber breaks in each ply of each of the three laminate types studied by comparisons of the average fiber break zone separations and average crack spacing, and by the infusion of gold chloride penetrant into the cracks which left residual particles at the interface to confirm that their locations were coincident with the fiber break concentrations in adjacent plies. The results of each method were consistent and together provided a firm basis for concluding that, in tension-tension cyclic loading of graphite/epoxy laminates at stress levels at which off-axis ply cracks develop, the preponderance of fiber breaks which occur do so adjacent to, and in response to, the action of cracks in facing plies.

The density and distribution of these fiber breaks were shown to be a function of the type of laminate and the state of matrix damage. The density of breaks was greatest for the $[0,90_2]_s$ laminate and smallest for the $[0,90,\pm 45]_s$ laminate. The two crack densities differed by a factor of ten. The observed fiber fracture density in the $[0,90,\pm 45]_s$ laminates was, in fact, surprisingly small even in specimens which were considered to be near failure. The relative differences were explained in terms of the concept of a laminate strength margin, the difference between 0 degree ply static strength and the stress in the 0 degree plies at the conclusion of the development of all of the matrix damage modes operative in that laminate. Based on a discounting of certain of the elastic properties in a laminated plate analysis, it was shown that the $[0,90_2]_s$ laminate

possessed the highest strength margin, the $[0,\pm45]_s$ laminate, a lower value, and the $[0,90,\pm45]_s$ laminate the lowest strength margin. This was the same descending order as that of the observed fiber density. The connection between the two evidently suggests the relationship of fiber fracture to the redistribution of stress within the 0 degree ply. For laminates cyclically loaded at a fixed fraction of the static fracture stress, those laminate types which are able, by mechanisms such as matrix cracking and delamination, to transfer much stress into the 0 degree plies during fatigue damage will have a small "strength margin" since very few fibers must subsequently break to create a situation where the local stress or strain is sufficiently high to initiate final fracture, while those types which have less effective stress transfer mechanisms to elevate the 0 degree stress-components during cyclic loading must experience larger numbers of fiber failures to create a local situation which is sufficiently severe to initiate fracture and are said to have a large strength margin. The presence or absence of fiber fractures at or near laminate fracture is a reflection and verification of this association.

The study of fiber fracture in these laminates yielded two additional results. First, the frequency of occurrence of multiple adjacent fiber breaks increased with increasing stages of matrix damage in both the $[0,90]_s$ and $[0,90,\pm45]_s$ laminates. Such a shift may be consequential to the study of laminate failure especially as represented by models based on critical multiplet size. The through-thickness variation of both fiber fracture density and multiplet

distribution in the 0 degree plies of the $[0,90_2]_s$ laminate was shown to be large, suggesting that fibers removed only slightly from the interface are insulated from the action of adjacent cracks. The second result was an indication that although the location and locus of fiber breaks was determined by the off-axis cracks, the mode of fiber fracture was dependent upon the state of stress in the plane of the fiber, showing a normal mode in plies having low shear stress and a mixed mode in planes having high shear stress.

We believe that the results of this study contribute to several areas of our understanding of composite materials. First is the area of material characterization. By combining several existing techniques, it was possible for the first time to critically examine several modes of damage occurring at the microstructural level. It is likely that in future research on laminate fracture will require this combined approach.

Also, by parallel analysis of NDE observations with destructive tests which yielded damage characterization, the interpretation of the NDE results was aided. This was particularly true of X-ray radiography which, in the case graphite/epoxy laminates, was shown to provide a wealth of highly resolved microscopic information, when properly interpreted. The benefit of more complete damage characterization also applies to NDE methods which were not extensively used in this investigation. Central to the development of ultrasonic or acoustic techniques, for example, is the ability to distinguish initial flaws from damage, to discriminate one damage mode from

another, and to assess the size and location of the damage in terms of the measured NDE parameters. Each of these decisions requires a knowledge of the precise damage state; the confidence attached to the technique can be no greater than the confidence attached to the damage characterization.

Another conclusion of this investigation relates to the issue of composite laminate failure. Although the where and why of fracture initiation remains elusive, the results of the Stage III characterizations, both in terms of damage and stiffness reduction, have re-emphasized the very short period during which critical conditions apparently develop. It will be necessary to expand this period experimentally, to isolate the processes which tend to localize damage, and to critically examine the interaction of the matrix damage modes with the fracture of fibers. It is, in the author's opinion, this interaction which will have the greatest potential role in developing an understanding of the final laminate failure event.

Several generalizations are suggested by our collective results. One of the most salient such generalizations is made possible by our discovery of the local delamination regions near interior matrix cracks and the new understanding of fiber failure processes during fatigue loading obtained from the study. We are able to conclude that internal stress redistributions are much larger than previously suspected and can be large enough to cause strength reductions of as much as 30-50 percent, levels which are commonly observed in long-term cyclic loading. It appears that fiber failure is much

less consequential in these large strength reductions than has been suggested in the literature, and that the acceleration of damage quite near the end of life for laminates of this type is caused by a localization of damage, primarily secondary matrix cracking and local delamination. We have found no evidence of accelerating fiber fracture in that region. Thus, it can be concluded that, at this point, internal stress redistribution appears to be the most important strength reduction mechanism for composite laminates similar to those studied.

A second salient conclusion is that during low-level cyclic loading, fiber-fractures occur almost exclusively at locations which are adjacent to the termination of a matrix crack in the adjacent plies. Stated in another way, matrix cracks in off-axis plies of angle-ply laminates seem to be important for long-term fatigue behavior primarily in the sense that they act as initiation points of fiber failure and local delamination. Hence, while matrix cracks alone do not reduce the residual strength during cyclic loading, the events associated with and nucleated by their presence are central to the development of subsequent damage which does reduce the strength, stiffness and life of composite laminates.

The third salient generality has to do with stiffness change. The longitudinal engineering modulus of composite laminates changes during long-term cyclic loading in large, systematic and reproducible ways which are directly and quantitatively related to the details of the micro-events which influence the residual properties of such

laminates. Moreover, when nondestructive techniques are used to obtain a precise and complete characterization of all of the internal damage in a specific specimen following long-term fatigue loading, and if proper models are used to relate those damage details to global response, the change in the longitudinal engineering stiffness of that specimen can be predicted with generally excellent agreement (usually within a percent or so) with experimentally measured values. Moreover, these changes can be associated with internal stress redistributions using the same models, and the residual strength of the laminates can be implied. While this last conclusion is supported by limited data, the concept has shown general agreement with experimental data in every instance tested.

REFERENCES

1. K. L. Reifsnider, "Fatigue Behavior of Composite Materials," Int'l. J. of Fracture, vol. 16, no. 6, Dec. 1979, pp. 563-583.
2. W. W. Stinchcomb and K. L. Reifsnider, "Fatigue Damage Mechanisms in Composite Materials: A Review," Fatigue Mechanisms, Proc. of an ASTM-NBS-NSF Symp., Kansas City, MO, May 1978, J. J. Fong, ed., ASTM STP-679, 1979, pp. 762-787.
3. P. W. R. Beaumont and Alan S. Tetelman, "The Fracture Strength and Toughness of Fibrous Composites," Failure Modes in Composites, I. Toth, ed., Metallurgical Society of AIMMPE, May 1972, pp. 49-80.
4. K. G. Kreider and L. Dardi, "Fracture Toughness of Composites," Failure Modes in Composites, I. Toth, ed., Metallurgical Society of AIMMPE, May 1972, pp. 193-230.
5. J. Awerbach and H. T. Hahn, "Crack-Tip Damage and Fracture Toughness of Borsic/Titanium Composite," Experimental Mechanics, Oct. 1980, pp. 334-344.
6. C. C. Poe, "A Single Fracture Toughness Parameter for Fibrous Composite Laminates," NASA TM 81911, March 1981.
7. T. S. Cook and C. A. Rau, "A Critical Review of Anisotropic Fracture Mechanics," Prospects of Fracture Mechanics, G. Sih, ed., 1974, pp. 509-523.
8. T. A. Cruse and H. J. Konish, "Elastic Fracture Mechanics for Advanced Fiber Composites: A Macromechanics Treatment," Polymer Plastic Technology and Engineering, vol. 4, no. 1, 1975, pp. 41-91.
9. G. Marom and A. C. Johnsen, "On the Applicability of Linear Elastic Fracture Mechanics to the Longitudinal Fracture of Unidirectional Composites," Materials Science and Engineering, vol. 39, 1979, pp. 11-14.
10. F. Erdogan, "Fracture of Composite Materials," Prospects of Fracture Mechanics, G. Sih, ed., 1974, pp. 477-492.
11. S. W. Tsai and H. T. Hahn, "Recent Developments in Fracture of Filamentary Composites," Prospects of Fracture Mechanics, G. Sih, ed., 1974, pp. 493-508.
12. D. H. Morris and H. T. Hahn, "Mixed Mode Fracture of Graphite/Epoxy Composites: Fracture Strength," J. of Composite Materials, vol. 11, April 1977, pp. 124-138.

13. Sih, G. C., "Fracture Mechanics of Composite Materials," Fracture of Composite Materials, G. Sih, ed., 1978, pp. 111-130.
14. Kanninen, M. F., Rybicki, E. G., and Brinson, H. F., "A Critical Look at Current Applications of Fracture Mechanics to the Failure of Fiber-Reinforced Composites," Composites, Jan. 1977, pp. 17-22.
15. Smith, C. W., "Limitations of Fracture Mechanics as Applied to Composites," Inelastic Behavior of Composite Materials, C. T. Herakovich, ed., AMD vol. 13, 1975, pp. 157-175.
16. Zweben, C., "Fracture Mechanics and Composite Materials: A Critical Analysis," Analysis of the Test Methods for High Modulus Fibers and Composites, ASTM STP-521, 1973, pp. 65-97.
17. Wu, E. M., "Strength and Fracture of Composites," Fracture and Fatigue, 1974, pp. 191-247.
18. Tsai, S. W. and Hahn, H. T., "Failure Analysis of Composite Materials," Inelastic Behavior of Composite Materials, C. T. Herakovich, ed., AMD vol. 13, 1975, pp. 73-96.
19. Chou, P. C., "Cumulative Damage Rule for Fatigue of Composite Materials," Modern Developments in Composite Materials and Structures: Proc. of the Winter Annual Meeting, New York, Dec. 1979.
20. Bolotin, V. V., "Stochastic Models of Cumulative Damage in Composite Materials," Engineering Fracture Mechanics, vol. 8, 1976, pp. 103-113.
21. Rosen, B. W., "Tensile Failure of Fibrous Composites," AIAA Journal, vol. 2, no. 11, Nov. 1964, pp. 1985-1991.
22. Zweben, C., "The Influence of Stress Nonuniformity and Size on the Strength of Composite Materials," J. of Material Science, vol. 12, 1977, pp. 1325-1337.
23. Zweben, C. and Rosen, B. W., "Statistical Theory of Material Strength with Application to Composite Materials," J. of the Mechanics and Physics of Solids, vol. 18, 1970, pp. 189-206.
24. Harlow, D. G. and Phoenix, S. L., "The Chain of Bundles Probability Model for the Strength of Fibrous Materials I: Analysis and Conjectures," J. of Composite Materials, vol. 12, 1978, pp. 195-213.

25. D. G. Harlow and S. L. Phoenix, "Probability Distributions for the Strength of Fibrous Materials II: A Numerical Study of Convergence," J. of Composite Materials, vol. 12, pp. 314-334, 1978.
26. S. B. Batdorf, "Tensile Strength of Unidirectionally Reinforced Composites--I," private communication, to be published.
27. S. B. Batdorf and R. Ghaffarian, "Tensile Strength of Unidirectionally Reinforced Composites--II," private communication, to be published.
28. R. L. Smith, "A Probability Model for Fibrous Composites with Local Load Sharing," Proc. of the Royal Society, vol. 372, 1980, pp. 539-553.
29. J. Hedgepeth and P. VanDyke, "Local Stress Concentrations in Imperfect Filamentary Composite Materials," J. of Composite Materials, vol. 1, 1967, pp. 294-309.
30. V. Tamuzs, "Dispersed Fracture of Unidirectional Composites," Fracture of Composite Materials, G. Sih, ed., 1978, pp. 13-24.
31. V. Tamuzs, "Some Peculiarities of Fracture in Heterogeneous Materials," Proc. of the Second USA-USSR Symp. on Fracture of Composite Materials, Lehigh Univ., Mar. 1981.
32. S. S. Wang and H. T. Wang, "Interlaminar Crack Growth in Fiber Reinforced Composites during Fatigue," Transactions of the ASME, vol. 101, Jan. 1979, pp. 34-41.
33. V. A. Kotchetkov and R. D. Maksimov, "Redistribution of Stresses Due to Fracture of Brittle Fibers in a Multilayer Composite," Mekhanika Kompozitnykh Materialov, no. 6, Nov.-Dec. 1980, pp. 1014-1028.
34. Y. Korczynsky and J. G. Morley, "Constrained Cracking in Cross-Ply Laminates," J. of Materials Science, vol. 16, 1981, pp. 1785-1795.
35. P. C. Chou and R. Croman, "Degradation and Sudden-Death Models of Fatigue of Graphite/Epoxy Composites," Composite Materials: Testing and Design, (Fifth Conf.), ASTM STP-674, 1979, pp. 431-454.
36. A. Kelly, "Multiple Fracture of Laminates," Fracture of Composite Materials, G. Sih, ed., 1978, pp. 193-202.

37. A. S. D. Wang and C. E. Lau, "An Energy Method for Multiple Transverse Cracks in Graphite-Epoxy Laminates," Modern Developments in Composite Materials and Structures, ASME Winter Meeting, New York, 1979.
38. Z. Hashin, "Fatigue Failure Criteria for Unidirectional Fiber Composites," Transactions of the ASME, vol. 48, Dec. 1981, pp. 846-852.
39. S. B. Batdorf, "Experimental Determination of Stresses in Damaged Composites Using an Electric Analogue," UCLA Report UCLA-ENG-82-36, May 1982.
40. G. A. Cooper, "Micromechanics Aspects of Fracture and Toughness," Fracture and Fatigue, pp. 415-448.
41. V. R. Regel and V. P. Tamuzs, "Fracture and Fatigue of Polymers and Composites," Polymer Mechanics (USSR), vol. 13, no. 3, May-June 1977, pp. 458-478.
42. R. J. Nuismer, "Predicting the Performance and Failure of Multidirectional Polymeric Matrix Composite Laminates: A Combined Micro-Macro Approach," Advances in Composite Materials, A. Bunsell, ed., ICCM 3, vol. 1, pp. 436-452.
43. J. G. Goree and R. S. Gross, "Analysis of a Unidirectional Composite Containing Broken Fibers and Matrix Damage," Engineering Fracture Mechanics, vol. 13, 1979, pp. 563-578.
44. J. G. Goree and R. S. Gross, "Stresses in a Three-Dimensional Unidirectional Composite Containing Broken Fibers," Engineering Fracture Mechanics, vol. 13, 1980, pp. 395-405.
45. J. E. Bailey and A. Parvizi, "On Fibre Debonding Effects and the Mechanism of Transverse Ply Failure in Cross-Ply Laminates of Glass Fibre/Thermoset Composites," J. of Materials Science, vol. 16, 1981, pp. 649-659.
46. A. Rotem and Z. Hashin, "Failure Modes of Angle Ply Laminates," J. of Composite Materials, vol. 9, April 1975, pp. 191-206.
47. J. H. Sinclair and C. C. Chamis, "Fracture Surface Characteristics of Off-Axis Composites," NASA TM-73700, 1977.
48. J. H. Sinclair and C. C. Chamis, "Fracture Modes in Off-Axis Fiber Composites," NASA TM-79036, 1979.
49. J. H. Sinclair and C. C. Chamis, "Mechanical Behavior and Fracture Characteristics of Off-Axis Fiber Composites, I--Experimental Investigation," NASA TP-1081, 1977.

50. M. Munro and P. W. R. Beaumont, "Fracture Mechanisms and Toughening of Fibre Composites," ICM 3, vol. 3, Cambridge, England, Aug. 1979, pp. 253-261.
51. B. Harris, "Micromechanisms of Crack Extension in Composites," Metal Science, Aug-Sept. 1980, pp. 351-363.
52. G. A. Cooper and Piggott, "Cracking and Fracture in Composites," Fracture 1977, ICF4, vol. 1, Waterloo, Canada, Jun. 1977, pp. 557-605.
53. R. J. Morgan, E. T. Mones and W. J. Steele, "The Microscopic Failure Processes of Kevlar/Epoxy Composites," Composites Technology Review, vol. 2, no. 3, 1980, pp. 3-5.
54. D. Purslow, "Some Fundamental Aspects of Composites Fractography," Composites, vol. 12, Oct. 1981.
55. G. E. Morris, "Determining Fracture Directions and Location of Fracture Origins on Failed Graphite/Epoxy Surfaces," Nondestructive Evaluation and Flaw Criticality for Composite Materials: Proc. of the Symp., Philadelphia, Oct. 1978, ASTM STP-696, 1979, pp. 274-297.
56. R. S. Williams and K. L. Reifsnider, "Fracture Analysis of Fatigue Damage Mechanisms in Fiber Reinforced Composite Materials Using Scanning Electron Microscopy," AFOSR-TR-75-0041, 1975.
57. R. A. Kline and F. H. Chang, "Composite Failure Surface Analysis," J. of Composite Materials, vol. 14, Oct. 1980, pp. 315-323.
58. K. L. Reifsnider, "Mechanics of Failure of Composite Materials," Fracture Mechanics Symp. on Naval Structural Mechanics, Sept. 1978, pp. 317-331.
59. K. L. Reifsnider, E. G. Henneke and W. W. Stinchcomb, "Defect-Property Relationships in Composite Materials," AFML-TR-76-81, June 1979.
60. J. E. Masters, Jr., "An Experimental Investigation of Cumulative Damage Development in Graphite Epoxy Laminates," Ph.D. Dissertation, Virginia Polytechnic Institute and State University, Mar. 1981.
61. S. V. Kulkarni, R. B. Pipes, R. L. Ramkumar and W. R. Scott, "The Analytical, Experimental, and Nondestructive Evaluation of the Criticality of Interlaminar Defect in a Composite Laminate," ICCM 2, pp. 1057-1071.

62. T. K. O'Brien, "Characterization of Delamination Onset and Growth in a Composite Laminate," Damage in Composite Materials, ASTM STP-775, 1982, to be published.
63. K. L. Reifsnider, K. Schulte and J. C. Duke, "Long-Term Fatigue Behavior of Composite Materials," Presented at ASTM Conf. on Long-Term Behavior of Composites, Williamsburg, VA, Mar. 1982.
64. R. D. Jamison, "Damage Development in Fiber-Reinforced Composite Materials," Presented at the Virginia Academy of Science Spring Meeting, Apr. 1982.
65. H. W. Herring, J. L. Lytton and J. H. Steele, "Experimental Observations of Tensile Fracture in Unidirectional Boron Filament Reinforced Aluminum Sheet," Metallurgical Transactions, vol. 4, Mar. 1973, pp. 807-817.
66. D. O. Stalnaker and W. W. Stinchcomb, "Load History-Edge Damage Studies in Two Quasi-Isotropic Graphite Epoxy Laminates," Composite Materials: Testing and Design (Fifth Conf.), ASTM STP-674, 1979, pp. 620-641.
67. C. T. Herakovich, "On the Relationship Between Engineering Properties and Delamination of Composite Materials," J. of Composite Materials, vol. 15, Jul. 1981, pp. 336-348.
68. F. W. Crossman, "Analysis of Free Edge Induced Failure of Composite Laminates," Fracture of Composite Materials, G. Sih, ed., 1978, pp. 291-302.
69. N. J. Pagano and R. B. Pipes, "Some Observations on the Interlaminar Strength of Composite Laminates," Int'l. J. of Mechanical Sciences, vol. 15, 1973, pp. 679-688.
70. N. J. Pagano and R. B. Pipes, "The Influence of Stacking Sequence on Laminate Strength," J. of Composite Materials, vol. 5, Jan. 1971, pp. 50-57.
71. R. B. Pipes and N. J. Pagano, "Interlaminar Stresses in Composite Laminates Under Uniform Axial Extension," J. of Composite Materials, vol. 4, 1970, pg. 538.
72. W. W. Stinchcomb, K. L. Reifsnider and R. S. Williams, "Critical Factors for Frequency-Dependent Fatigue Processes in Composite Materials," Experimental Mechanics, vol. 16, no. 9, Sept. 1976, pp. 343-348.
73. C. T. Sun and W. S. Chou, "Frequency Effect on the Fatigue Life of a Laminated Composite," Composite Materials: Testing and Design (Fifth Conf.), ASTM STP-674, 1979, pp. 418-430.

74. W. W. Stinchcomb, K. L. Reifsnider, P. Yeung and J. Masters, "Effect of Ply Constraint on Fatigue Damage Development in Composite Material Laminates," Fatigue of Fibrous Composite Materials, ASTM STP-723, 1981, pp. 64-84.
75. W. Johnson and S. K. Ghosh, "Some Physical Defects Arising in Composite Material Fabrication," J. of Materials Science, vol. 16, 1981, pp. 285-301.
76. R. D. Kriz, W. W. Stinchcomb and D. R. Tenney, "Effects of Moisture, Residual Thermal Curing Stresses, and Mechanical Load on the Damage Development in Quasi-Isotropic Laminates," VPI-E-80-5, Virginia Polytechnic Institute and State University, 1980.
77. T. K. O'Brien and K. L. Reifsnider, "Fatigue Damage: Stiffness Strength Comparisons for Composite Materials," J. of Testing and Evaluation, vol. 5, no. 5, Sept. 1977, pp. 384-393.
78. T. K. O'Brien and K. L. Reifsnider, "Fatigue Damage Evaluation Through Stiffness Measurements in Boron-Epoxy Laminates," J. of Composite Materials, vol. 15, Jan. 1981, pp. 55-70.
79. A. Highsmith and K. L. Reifsnider, "Stiffness-Reduction Mechanisms in Composite Laminates," Damage in Composite Materials, STP-775, Apr. 1982, pp. 103-117.
80. J. J. Nevadunsky, M. J. Salkind and J. J. Lucas, "Early Fatigue Damage Detection in Composite Materials," J. of Composite Materials, vol. 9, no. 4, Oct. 1975.
81. M. J. Owen, "Fatigue Processes in Fiber Reinforced Plastics," Philosophical Transactions of the Royal Society, vol. 294, 1980, pp. 535-543.
82. H. T. Hahn and R. Y. Kim, "Fatigue Behavior of Composite Laminates," J. of Composite Materials, vol. 10, Apr. 1976, pp. 156-180.
83. H. T. Hahn, "Fatigue Behavior and Life Predictions of Composite Laminates," Composite Materials: Testing and Design (Fifth Conf.), ASTM STP-674, 1979, pp. 383-417.
84. R. Harris, "Fatigue and Accumulation of Damage in Reinforced Plastics," Composites, Oct. 1977, pp. 214-220.
85. J. Awerbach and H. T. Hahn, "Off-Axis Fatigue of Graphite/Epoxy Composite," Fatigue of Fibrous Composite Materials, ASTM STP-723, 1981, pp. 243-273.

83. Hahn, H. T., "Fatigue Behavior and Life Predictions of Composite Laminates," Composite Materials: Testing and Design (Fifth Conf.), ASTM STP-674, 1979, pp. 383-417.
84. Harris, B., "Fatigue and Accumulation of Damage in Reinforced Plastics," Composites, Oct. 1977, pp. 214-220.
85. Awerbach, J. and Hahn, H. T., "Off-Axis Fatigue of Graphite/Epoxy Composite," Fatigue of Fibrous Composite Materials, ASTM STP-723, 1981, pp. 243-273.
86. Bader, W. G., Bailey, J. E., Parvizi, A. and Curtis, P. T., "The Mechanisms of Initiation and Development of Damage in Multi-Axial Fiber-Reinforced Plastic Laminates," Mechanical Behavior of Materials: Proc. of the Third Int'l. Conf., 1979, vol. 3, pp. 227-239.
87. Freeman, S. M., "Characterization of Lamina and Interlaminar Damage in Graphite-Epoxy Composites by the Depley Technique," Composite Materials: Testing and Design (Sixth Conf.), STP 787, 1982.
88. Reifsnider, K. L., "Some Fundamental Aspects of the Fatigue and Fracture Response of Composite Materials," Proc. of the Fourteenth Annual Meeting of the Society of Engineering Science, Lehigh Univ., Nov. 1977.
89. Reifsnider, K. L. and Talug, A., "Analysis of Stress Fields in Composite Laminates with Interior Cracks," VPI-E-78-23, Sept. 1978.
90. O'Brien, T. K., "An Evaluation of Stiffness Reduction as a Damage Parameter and Criterion for Fatigue Failure in Composite Materials," Ph.D. Dissertation, Virginia Polytechnic Institute and State University, Oct. 1978.
91. Rummel, W. D., Tedrow, T. and Bunkerhoff, H. D., "Enhanced Stereoscopic NDE of Composite Materials," AFWAL Technical Report 80-3053, 1980.
92. Sendekyj, G. P., Maddux, G. E. and Porter, E., "Damage Documentation in Composites by Stereo Radiography," in Damage in Composite Materials, STP 775, K. L. Reifsnider, Editor, American Society for Testing and Materials, 1982, pp. 16-26.
93. Nair, P. and Reifsnider, K. L., "A Stress Function Formulation and Approximate Solution of the Unsymmetric Deformation Problem for Cracks in Non-uniform Materials," VPI-E-73-31 Report, Sept. 1973.

94. Broek, D., "Elementary Fracture Mechanics", Sijthoff & Nordhoff, 1978.
95. Post, D., "Optical Interference for Deformation Measurements-- Classical, Holographic and Moire Interferometry," Mechanics of Nondestructive Testing, W. W. Stinchcomb, ed., Sept. 1980.
96. Jamison, R. D., "An Investigation of Damage Development in Fiber-Reinforced Composite Materials," presented at the ASNT Fall Conference, Oct. 1981.
97. Highsmith, A. L. and Reifsnider, K. L., "Non-uniform Microstrain in Composite Laminates," Composites Technology Review, vol. 4, no. 1, 1982, pp. 20-22.
98. Reifsnider, K. L., Private communication.
99. O'Brien, T. K. and Reifsnider, K. L., "Fatigue Damage: Stiffness/Strength Comparisons for Composite Materials," Journal of Testing and Evaluation, vol. 5, no. 5, 1977.
100. Russel, W. B., "On the Effective Moduli of Composite Materials: Slender, Rigid Inclusions at Dilute Concentrations," Journal of Applied Mathematics and Physics, (ZAMP), vol. 23, 1972.
101. Russel, W. B., "On the Effective Moduli of Composite Materials: Effect of Fiber Length and Geometry at Dilute Concentrations," Journal of Applied Mathematics and Physics, (ZAMP), vol. 24, 1973.

APPENDIX. Moiré Interferometry

In the early stages of this investigation, the need for a full field, real time quantitative nondestructive measure of damage development in composite materials was recognized. Such a technique might make possible the location of damage as well as a measure of its intensity. With such information the effect of the interior damage upon the exterior 0 degree plies could be studied. If the technique could provide this information in a stress-related form, then difficult, unanswered questions about the stress redistribution which occurs in these critical load-bearing plies could be approached. Answers to such questions must precede, in the author's opinion, a full understanding of the fracture process, both static and fatigue.

A technique which could potentially meet these requirements is moiré interferometry. As part of the damage development investigation undertaken, moiré interferometry was applied to the study of behavior in notched and unnotched laminates of several different materials. The feasibility of this application was demonstrated and the sensitivity of the method to subsurface damage was assessed. Although the results were not central to the investigation of fatigue damage for reasons to be described, the potential of the method to become an important NDE technique in the study of damage development and failure of composite materials warrants a brief discussion of--(i) the fundamental concepts, (ii) the practical application and (iii) the results of some preliminary testing.

Principle

Moiré interferometry is a classical optical technique which has been used for many years in a wide range of applications in which measurement of very small displacements or displacement gradients is required. Interferometry describes a technique by which the phenomenon of wave interference can be used in such a way that the interference pattern produced can be related to some physical entity. This is most often accomplished by using gratings of uniformly spaced parallel lines. Such gratings pose alternating barriers and openings for the passage of light. At grating frequencies above 1000 lines/inch (40 lines/mm), light passing through the grating is diffracted into a fan of light rays maintaining the characteristic wavelength but each diminished in intensity.

Practical benefit is realized when one of the diffraction gratings is kept fixed in frequency and orientation (the "reference" grating) while the other, (which initially has the same frequency and orientation) is permitted to rotate and deform. This is normally accomplished by affixing this "active" grating to the surface of a body which itself rotates, stretches or compresses. The reference grating need not be real. It is equally suitable and, for some applications more desirable, to use a "virtual" grating formed by two intersecting beams of light. When the active and reference grating are adjacent, the interaction of diffracted light from each produces a pattern of alternately dark and light bands in space termed moiré fringes. Moiré fringes represent the locus of points of constant

displacement in the plane of the active grating and in the direction perpendicular to the lines of the reference grating.

In order to measure the displacements in the deformed state, each moiré fringe is assigned a fringe order, N . This is the number of cycles of intensity fluctuation (light to dark) experienced as the displacement changes from zero to its final value. Its relationship to displacement is given by:

$$\begin{aligned} u &= gN_x \\ v &= gN_y \end{aligned} \tag{A-1}$$

where u and v are orthogonal components of in-plane displacement in x and y directions respectively, g is the pitch of the reference grating (reciprocal of the frequency), and N_x and N_y are fringe order numbers where lines on the reference grating are perpendicular to the x and y coordinate axes respectively. Strains are related to displacements by:

$$\begin{aligned} \epsilon_x &= \frac{\partial u}{\partial x} \\ \epsilon_y &= \frac{\partial v}{\partial y} \\ \gamma_{xy} &= \frac{\partial u}{\partial y} + \frac{\partial v}{\partial x} \end{aligned} \tag{A-2}$$

Stresses can, in principle, be obtained from the strains if the constitutive relation for the material is known.

Production of Diffraction Gratings

For the work to be reported here, the method of Post [95] was applied. By this method gratings are replicated from a photographic mold onto a thin layer of epoxy which itself is bonded to the specimen surface. The mold is made by exposing an ultra-high resolution photographic plate to two intersecting beams of coherent light. The frequency of the grating is controlled by the frequency and angle of interference of these beams. When the plate is developed, silver grains remain in the exposed zones while the silver is leached out in the unexposed zones. The gelatin matrix shrinks upon drying; but, because it is partially constrained by the silver, shrinkage is greatest in the unexposed zones. The result is a photographic plate with a furrowed surface which can be used as a mold.

To replicate the grating, epoxy is squeezed into a thin layer between the specimen and mold. Upon curing, the mold releases easily from the epoxy, leaving a replicated grating on the specimen. The epoxy material used was essentially transparent. A ten-to twenty-fold increase in intensity of the diffracted beams can be achieved by reflectorizing the surface of the grating. This is accomplished by aluminizing the master grating using a vapor deposition technique. Upon replication, the aluminum film releases from the master but adheres to the epoxy. The result is a reflectorized grating of undegraded quality. An example is shown in Fig. A-1.



Figure A-1. Example of a Reflectorized Grating on a Graphite/Epoxy Specimen.

Experimental Arrangement

The optical elements necessary for forming a virtual grating and for observing and photographing the moiré fringe pattern are shown in Fig. A-2(a). The light source (A) was a 5 mW continuous-wave helium-neon laser having a wavelength of 633 nm manufactured by Spectra Physics. The narrow beam of coherent light emitted by the laser was spread into a cone by a diverging lens (B), passed through a 10 μ m diameter spatial filter (C) to exclude all but the uniformly intense inner core and finally through a 3.5 inch (89 mm) diameter collimating lens (D) to make the beam once more parallel. One-half of this beam illuminated the active grating (E) directly; the other half was reflected by a front surface mirror (F) onto the grating. In the region of coincidence of these incident and reflected beams, a virtual reference grating having a frequency of 15,000 lines/inch (600 lines/mm) was formed adjacent and parallel to the active grating on the specimen. (Detail of this region is shown in Fig. A-2(b)).

The moiré fringe pattern developed passed through a camera lens (G) which produced a full sized image on the ground glass (H) for observation or photographic negative for photography. Observation was by a 5X hand magnifier. Photography was accomplished with Kodak Contrast Pan sheet film. Exposure times depended upon the reflectivity of the grating but were typically 1/15 sec. for reflectorized gratings.

All of the optical elements were affixed to a flat plate which in turn was fixed within a rigid steel frame. The frame and optics

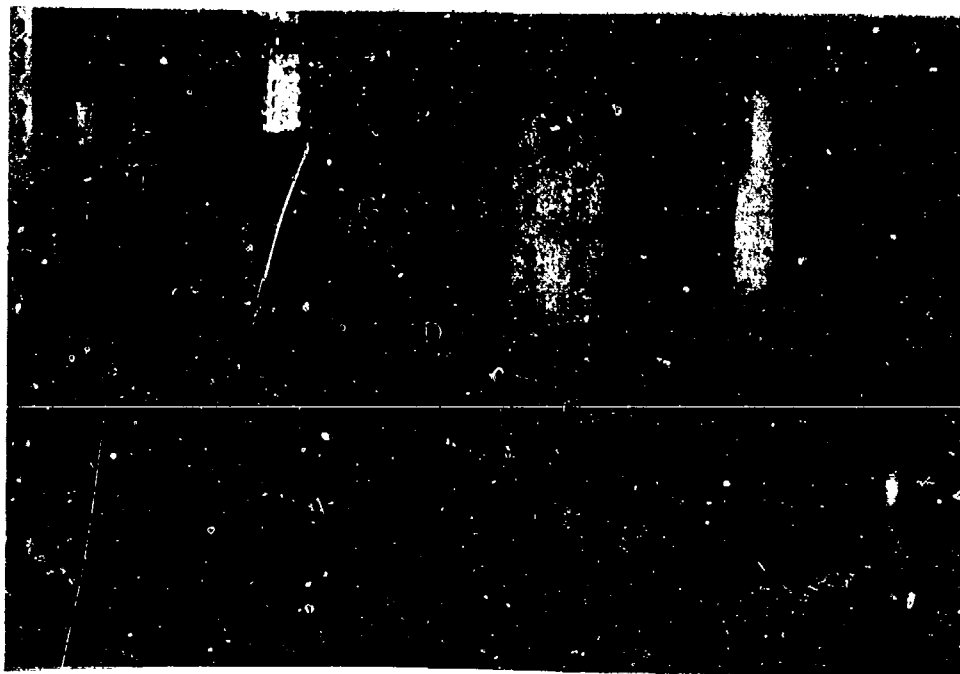


Figure A-2. (a) Moire Interferometry Optical Arrangement.

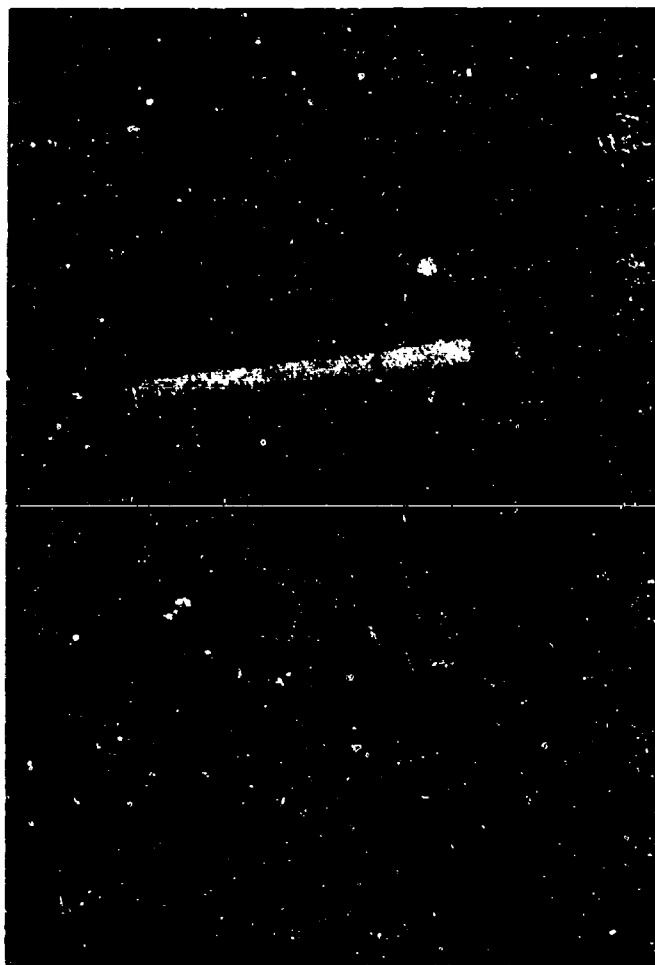


Figure A-2. (b) Moire Interferometry Optical Arrangement.
(Cont'd.)

assembly was attached to the crosshead support columns of an MTS testing machine. There existed sufficient adjustability in the optics plate-to-frame assembly attachment that the proper orientation between the optical path fixed by the elements on the plate and the specimen loaded in the testing machine grips could be achieved. Once this orientation was fixed, moiré fringe patterns could be developed easily and routinely by adjusting the orientation of the front surface mirror.

Since the method of moiré interferometry is by design a sensitive displacement measuring technique, it is perhaps not surprising that the stability of the moiré fringe pattern is sensitive to very small amplitude vibrations occurring in the optics or in the specimen. The first of these was approached by stiffening the frame and by providing additional attachment points to the MTS columns to compensate for its cantilever profile. In addition, it was found that very low frequency vibrations, on the order of 6 to 10 HZ, were being transferred to the optics assembly through the floor. For example a door closing fifty feet away was sufficient to upset a stable fringe pattern, as were a variety of pumps and motors located throughout the building. It was necessary therefore to isolate the MTS machine itself from the floor. This was accomplished by the installation of four air shock mounts at the machine base. The pressure in the shock mounts was adjusted to optimize the damping of the highest amplitude and most common frequencies. The result was a notable, although not complete, reduction of fringe instability.

The second source of instability was related to the function of the MTS machine itself. Being a hydraulically-controlled servo-feedback system, it is constantly applying small corrections to the specimen displacement in order to control load or displacement. The resultant destabilizing effect on the fringe pattern was both anticipated and unavoidable. Fortunately, the disturbance was high frequency and low amplitude and did not adversely affect either observation or photography.

One additional destabilizing effect was not anticipated. By the arrangement of the optics on the plate, the laser was situated below most of the other elements when the plate was attached to the MTS machine. Heat generated by the laser produced convective currents which disturbed the optical path above the laser and resulted in a very slow oscillation in the fringe pattern. The problem was solved by enclosing the entire optical arrangement, including the specimen but excluding the laser. This provided a marked improvement in fringe stability by eliminating not only the laser heat influence but also other convection currents which existed in the room. The box enclosure was made of cardboard sheets painted black and sealed with tape at the joints. The result was essentially a camera with which moiré interferometry patterns could be photographed under any external lighting conditions.

The preliminary investigation of the moiré technique was conducted on the MTS machine. Despite the unavoidable contribution of machine-induced vibration, the results, which will be described in a

following section, confirmed the feasibility of the technique. The quality of the interferometry photographs produced was more than adequate for interpretation and analysis.

However, in an effort to eliminate the contribution of the MTS machine itself to fringe instability, an ATS dead load testing machine was procured. This 8000 lbf (36 N) capacity machine was completely manually operated. The optics plate and frame assembly was transferred from the MTS machine and attached to an air-shock mount-supported frame on which the dead load machine rested. Hence, a rigid, isolated coupling of all of the elements required in the moiré interferometry study was accomplished. Figure A-3 shows this arrangement. The testing machine was modified so that both load-controlled and displacement-controlled modes of loading were possible. Load-controlled testing was accomplished with the machine in the deadload configuration for which it was designed. Displacement-controlled loading was not used in the work reported here.

Procedure and Results

Preliminary static testing was performed with laminates fabricated locally from Scotchply 1002 E-glass/epoxy material manufactured by 3-M Company. The cure cycle used was 325°F (163°C), 70 psi (0.5 MPa) for 35 minutes. Specimens were prepared and examined as described for graphite/epoxy material in Chapter 3. The gratings, some reflectorized, were attached to the specimens in the as-fabricated condition. The surface was lightly sanded with 600 grit silicon carbide wetted paper to improve adhesion of the gratings. The

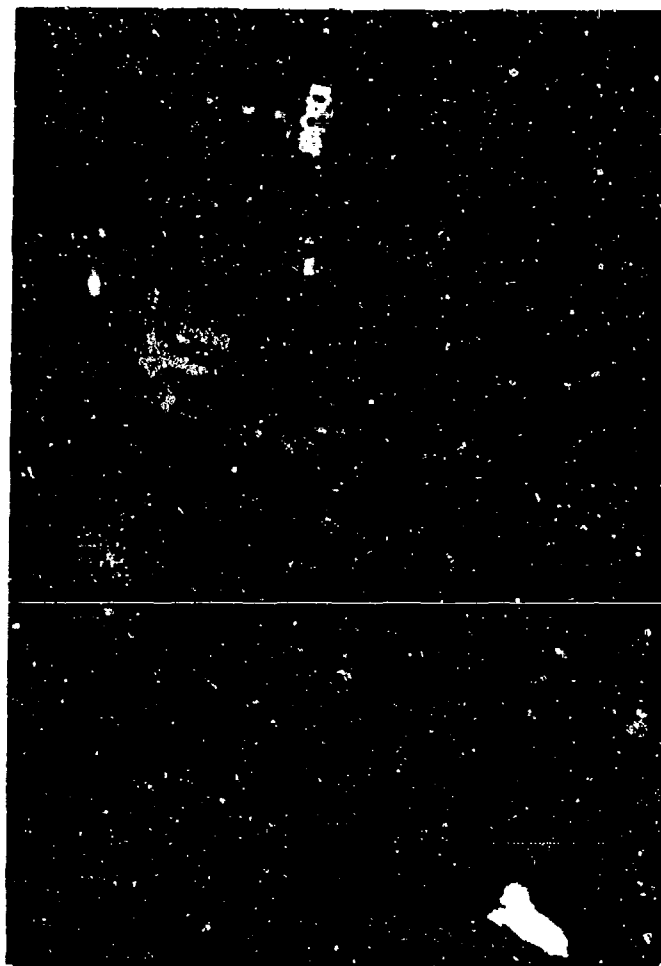


Figure A-3. Moire Interferometry Optical/Loading Machine Arrangement.

specimens were then loaded statically and the fringe pattern corresponding to the longitudinal (u) displacement field was observed. Figure A-4 shows results from one such test. The specimen was a $[0_4]$ laminate with dimensions 1 inch (25.4 mm) wide, 8 inches (203 mm) long and 0.025 inches (0.635 mm) thick. In the center of the specimen was placed a 0.25 inch (6.4 mm) through notch prior to curing. The notch was oriented perpendicular to the direction of loading.

Figure A-4(a) shows the u-displacement field at a load sufficiently low that the epoxy ligament which sealed the crack during curing had not been broken. Figure A-4(b) shows the displacement field after the addition of a small load increment sufficient to open the crack. As one would expect, large strains (displacement gradients) exist at the notch tip and the disturbance created by the presence of the notch diminishes with increasing distance from the notch.

Figure A-5 shows the displacement field for a $[0,90_3]_S$ E-glass/epoxy specimen having dimensions 1 inch wide, 8 inches long, and 0.05 inches (1.3 mm) thick. Figure A-5(a) corresponds to a load of approximately 100 lbf (0.4 N) and the displacement field is effectively uniform. Figure A-5(b) is the displacement field for the same specimen after it had been loaded to approximately 1200 lbf (5.3 N) and then unloaded. Such a load is sufficient to produce cracks in the 90 degree plies. The disturbances caused by these cracks are seen as disturbances in the moiré fringe pattern. Regions of high fringe density (high displacement gradient) are regions of residual strain

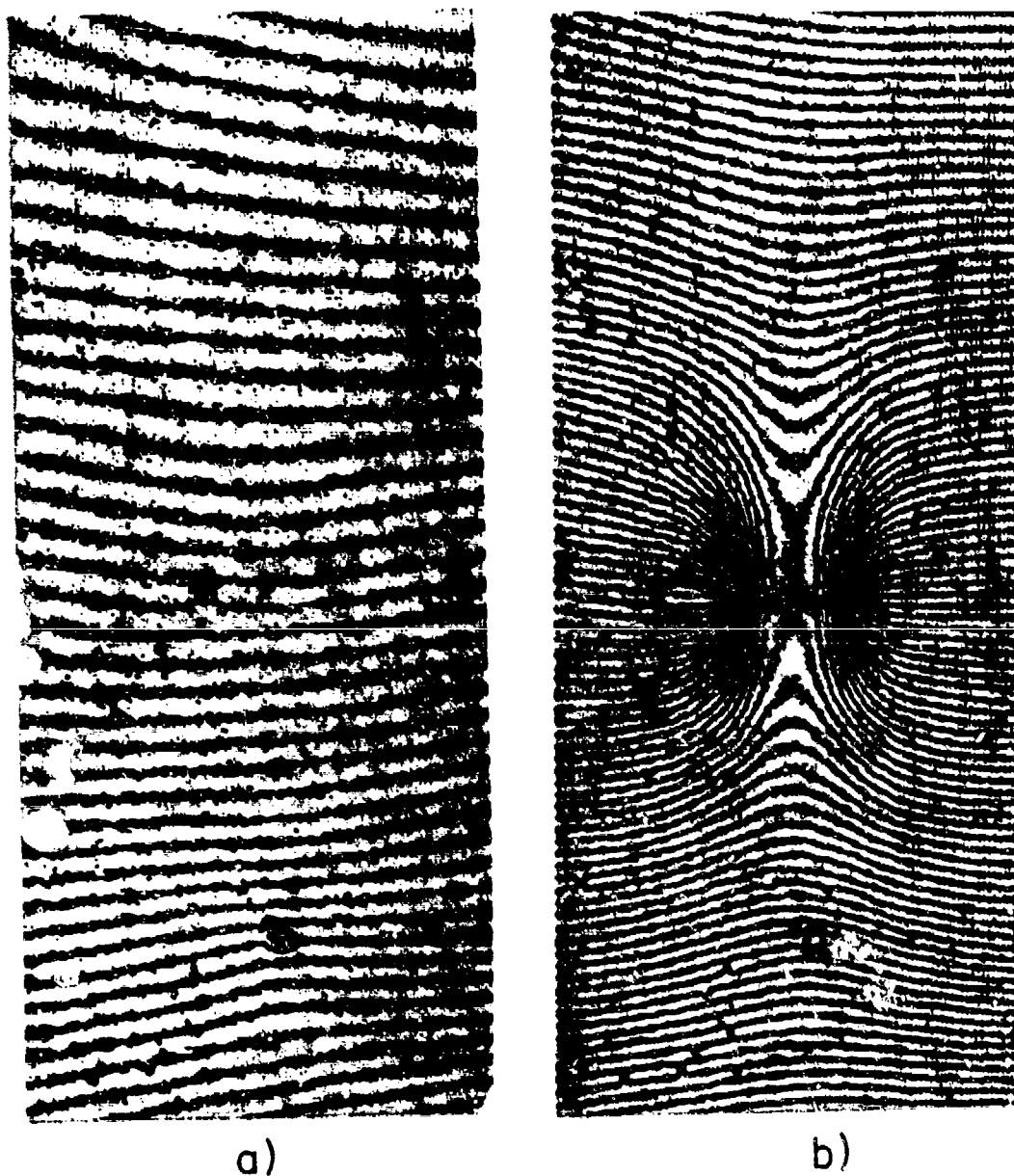
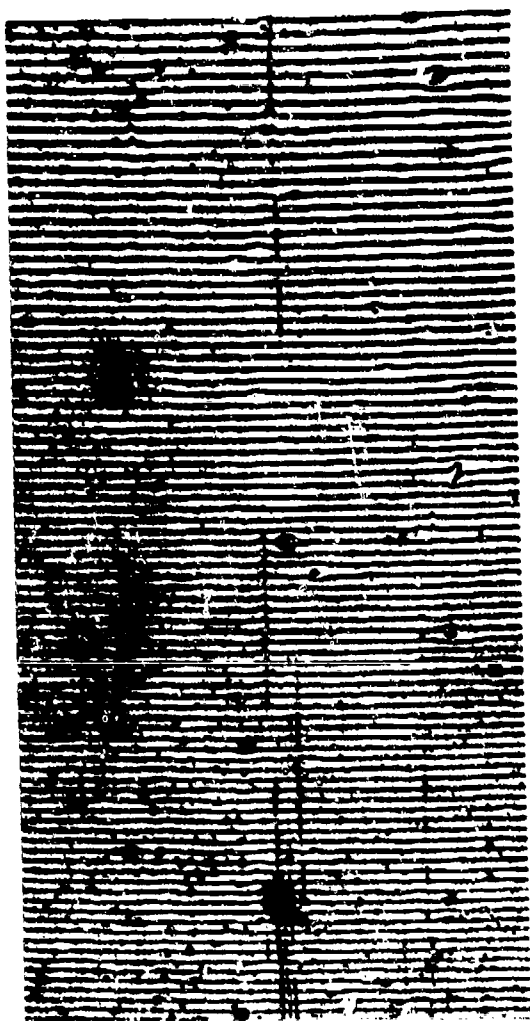
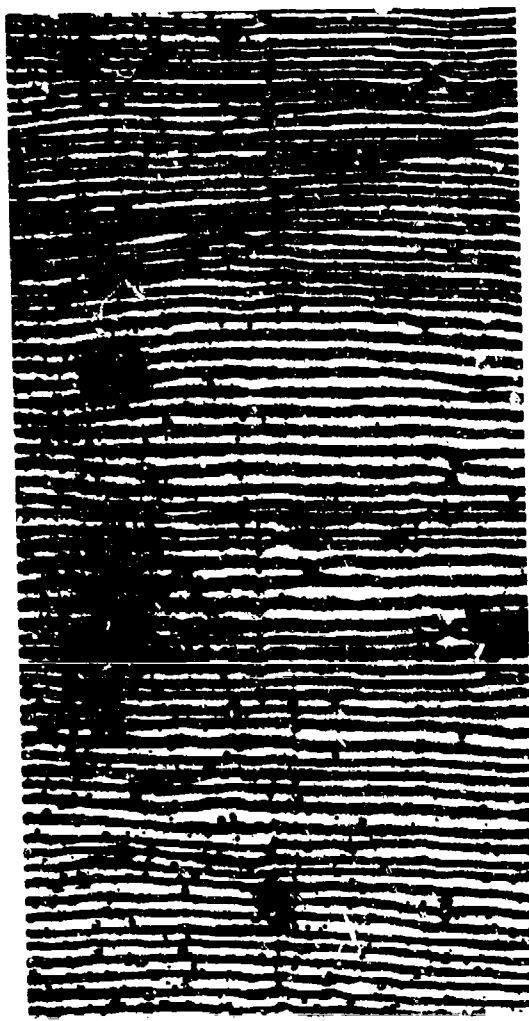


Figure A-4. Moiré Fringe Pattern for a $[O_2]_s$ E-Glass/Epoxy Specimen with a Center Notch: (a) before Crack Opening; (b) after Crack Opening.



a)



b)

Figure A-5. Moiré Fringe Pattern for a $[0,90_3]_s$ E-Glass/Epoxy Specimen: (a) at 100 lbf Load; (b) at 1200 lbf Load.

intensification due to subsurface cracks. Ultrasonic C-scan, X-ray radiography and edge replication of this and similarly loaded specimens established a strong correlation between crack location and disturbances in the moiré fringe pattern as reported by the author in reference [94].

In order to examine the sensitivity of the method to the size and location of imbedded flaws, a series of tests was conducted using 1 inch wide, 8 inch long, and 0.0375 inch (0.953 mm) thick $[0,90,0]_S$ E-glass/epoxy laminates in which flaws of 0.125 inch (3.18 mm), 0.250 inch (6.35 mm) or 0.500 inch (12.7 mm) were cut into one of the interior 0 degree plies prior to fabrication. The flaws were oriented normal to the specimen length and load axis and were symmetric with respect to the in-plane coordinates but were asymmetrical about the mid-plane. A typical specimen is shown schematically in Fig. A-6. A reflectorized 15,000 lines/inch (600 lines/mm) grating was attached to each surface of the specimen using the method previously described. The specimen was then loaded incrementally to 1000 lbf (4.45 N) in the dead load machine and the displacement pattern was observed. Alternation between observing the pattern on the surface nearest the flaw or the surface farthest from the flaw could be accomplished by rotating the specimen and clamp assembly 180 degrees about the load axis without otherwise disturbing the dead load linkage.

Results for a specimen having a 0.500 inch imbedded flaw are shown in Fig. A-7. Figure A-7(a) is the displacement field of the surface nearest the flaw with the specimen loaded to 1000 lbf. The

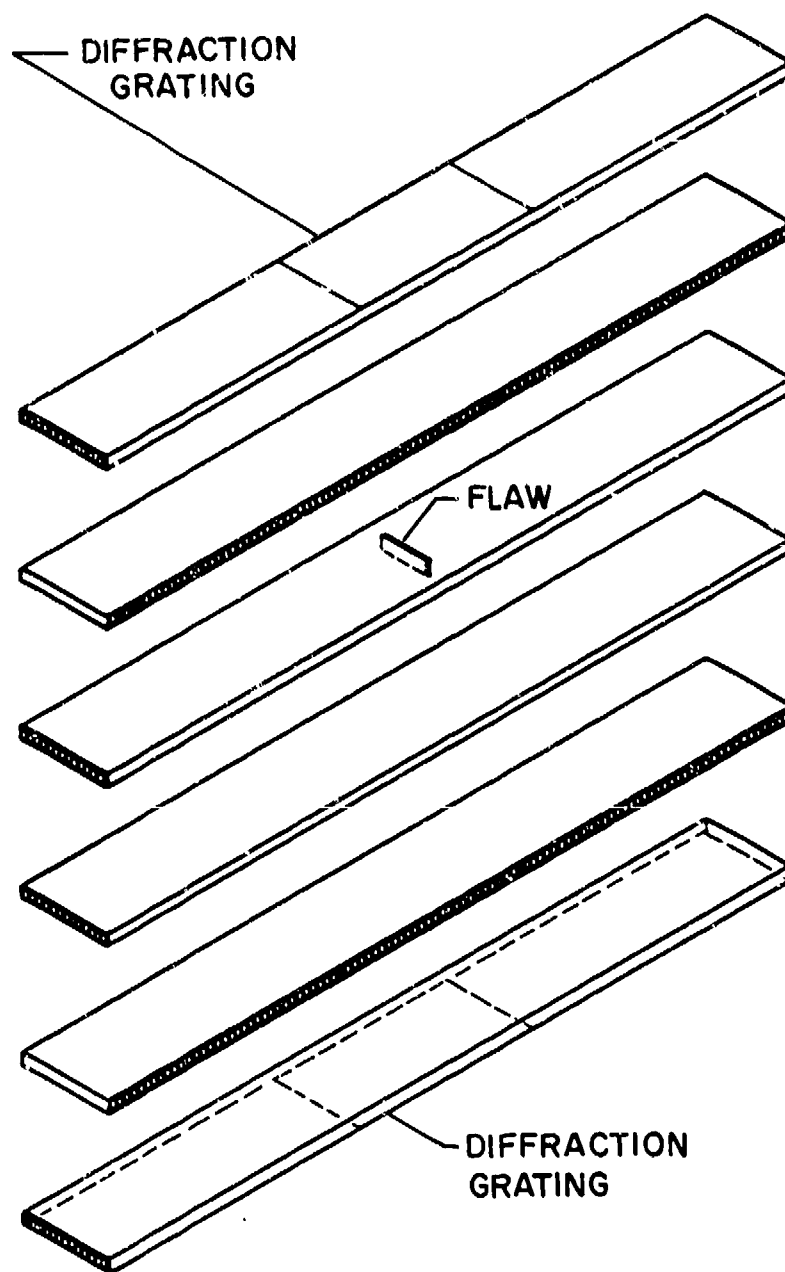
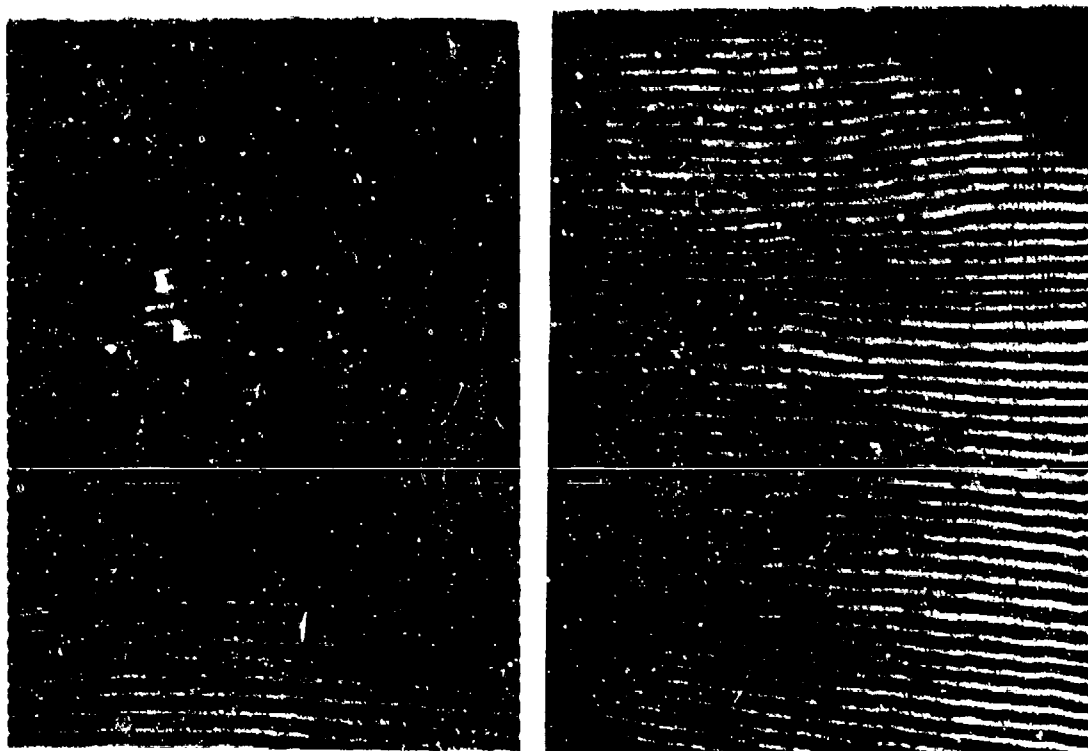


Figure A-6. Schematic of a Specimen with an Imbedded Flaw.



a)

b)

Figure A-7. Moiré Fringe Pattern for a $[0,90,0]_s$ Graphite/Epoxy Specimen with an Imbedded Flaw, Observing: (a) the Surface near the Flaw; (b) the Surface far from the Flaw.

presence of the flaw is clearly manifested in the upper portion of the photograph centered approximately on two orthogonal fiducial marks. The displacement field at a distance approximately equal to the flaw width is essentially uniform. Figure A-7(b) shows the obverse of the same specimen, also at a load of 1000 lbf. The disturbance caused by the flaw is perceptible in the neighborhood of the fiducials but the displacement perturbation has obviously been attenuated by the additional, intervening ply. Neither the extent nor the location of the flaw is evident in this case although the broad zone of disturbance appears to be somewhat larger than the near-flaw picture. As a result of this series, it was concluded that in E-glass/epoxy material, disturbances smaller than 0.125 inch and more than two plies removed from the surface being observed would not likely be detectable using an arrangement having the sensitivity described here.

Interrogation of fatigue damaged specimens was accomplished in a slightly different manner. In order to avoid fatigue damage to the grating itself, specimens were cyclically loaded without the grating in place. When the desired level of damage had been achieved, the specimen was removed from the MTS testing machine, a reflectorized grating was attached and the specimen was placed in the dead load machine where it was incrementally loaded to reopen, but not initiate, cracks and other damage. Figure A-8 shows one result. Figure A-8 is the displacement field of a $[0,90_2]_s$ graphite/epoxy specimen after 400 thousand cycles of tension-tension cyclic loading upon reloading to 1000 lbf static. Disturbances in the displacement field corresponding

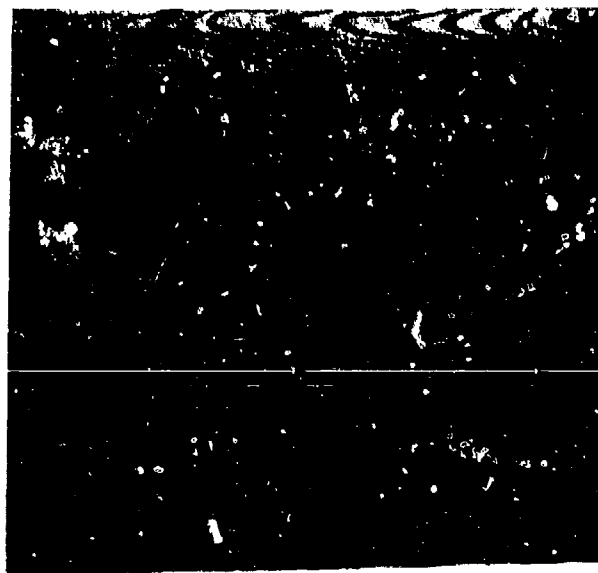


Figure A-8. Moiré Fringe Pattern for a $[0,90_2]_s$ Graphite/Epoxy Specimen after 400,000 Cycles of Fatigue Loading.

to transverse cracks are evident. Hourglass-shaped details in this photograph result from flaws in the diffraction grating.

Although the observable moiré fringe perturbations of Figure A-8 provide some insight into the location of regions of significant sub-surface disturbance, the greatest potential benefit of the technique lies in its ability to provide the 0 degree strain field. Several schemes were used to develop the strain field from the displacement field. Both manual and computer aided curve-fitting methods have been employed with some success. Highsmith [95] has manually computed the strain field between adjacent transverse cracks of a $[0,90_3]_S$ E-glass/epoxy laminate from the displacement field obtained interferometrically using the apparatus described here. His results provided verification of the validity of the shear lag analysis which had been applied to that laminate to predict the one-dimensional stress state adjacent to a crack.

Evaluation of the influence of fatigue damage on the 0 degree ply stress field poses a somewhat greater problem. The damage which develops in both the 0 degree and interior plies is complex. A satisfactory scheme for translating displacement information into strain information sufficient to accurately represent this complexity must be developed before the inherent sensitivity of the moiré technique can be fully exploited. Moreover, a larger field of view is required if a reasonable expectation of including the potential fracture site is to be realized. Such observations can be exceedingly valuable in studies of the precise nature of the localization process involved in

fracture. Finally, modification of the optical arrangement to permit measurement of both u and v displacements and to permit the use of higher frequency diffraction gratings would provide all of the components of the plane strain tensor with substantially improved accuracy.

Each of these modifications will in fact be integrated into the system described in this appendix. The preliminary phase of the work has demonstrated both the feasibility of the method and the desirability of continuing its development as a real time, in situ nondestructive evaluation technique.